Optimization of Sub-THz and THz Resonant-Tunneling-Diode Oscillators with Symmetrical Slot Antennas

Nguyen Dinh Tuan

Supervisor: Uni.Prof. M. Feiginov

Fakultät für Elektrotechnik und Informationstechnik
Technische Universität Wien

This dissertation is submitted for the degree of
Doctoral of Philosophy

TU Wien October 2023

Declaration

I hereby declare that except where specific reference is made to the work of others, the contents of this dissertation are original and have not been submitted in whole or in part for consideration for any other degree or qualification in this, or any other university. This dissertation is my own work and contains nothing which is the outcome of work done in collaboration with others, except as specified in the text and Acknowledgements. This dissertation contains fewer than 65,000 words including appendices, bibliography, footnotes, tables and equations and has fewer than 150 figures.

Nguyen Dinh Tuan
October 2023

Acknowledgements

I would like to gratefully thank my supervisor, Univ. Prof. Michael Feiginov. My starting point about the field of the project was not so good; however, he was always patient and calm with me, he gave me time and helpful advice during my doctoral studies and when writing this thesis. "My office always opens, you can come at anytime." - his open-mind sentence brought more confidence to me and shifted my point of view on many problems to new levels.

I also want to express my gratitude to all the members in my research team. They patiently listened to my frequent and sometimes incoherent discussions about the challenges that I was facing and gave me helpful advice. Specifically, I thank Petr Ourednik for his deep discussion and advice regarding the calculation and devices' fabrication. To Christian Spudat and Horia Boterzan, who had shown and done hundreds experiments with me in the clean-room, and for their deep humanity. To Gabriele Picco, who has done a great deal of work on the second published scientific article relevant to this thesis. To Bob Mirkhaydarov, who was graduated from the same university with me (MIPT), for his personality, he showed me how a PhD student looks like and how to arrange the time for writing the thesis. To Zehn Luo for showing me his deep knowledge about Python programming. To Zoltan Jehn for introducing me beatifull lanscapes to visit his home city - Budapest.

Furthermore, I would like to express my gratitude to the Center for Micro- and Nanostructures personnel for granting me access to the clean-room facilities, which were instrumental in the fabrication of the devices discussed in this thesis. Specifically, I extend my appreciation to Dr. Werner Schrenk, whose dedication has ensured the clean room's consistent high performance. Moreover, I am thankful to all the users of the clean-room for their valuable on-site guidance and assistance. I would also like to acknowledge the Technische Universität Wien and Austria for affording me the opportunity to pursue my studies. Additionally, I thank to the Austria Science Fund FWF for their financial support of our research project, identified by the reference number P30892-N30.

Finally, I would like to thank my family, my father, parents-in-law, sisters, brother- and sister-in-law that provided for me and encouraged me to fulfill my PhD studies. "I love you, mom" - this very simple sentence I had not said and have no more chances to say to my mother, who can only attend my graduation from some another planet. To my wife - my forever love, who quit a favorite job in Vietnam to go with me to a foreign country. She always says to me: "Nonetheless where we are, being with you is our home." To my lovely sons, who bring power, laugh, and happiness to me everyday.

Nguyen Dinh Tuan - Vienna, 2023

Abstract

The first topic of the thesis is focused on the analysis of how the oscillation frequency limitation of the symmetrical slot-antenna RTD oscillators depends on the parasitic elements of the circuit, especially on the contact resistance and the spreading resistance. In the high-frequency regime, the RTD areas are quite small, and the top contact resistance has a large impact; however, the spreading resistance plays a small contribution on the total parasitic resistance. The spreading resistance is dominant for large RTD areas corresponding to the low-frequency regime of the RTD oscillators. For the simple analysis of maximizing the oscillation frequencies of RTD oscillators, by adjusting the effects of these parasitic elements, one can estimate the parameters of the RTD oscillators, such as the length and the width of the slot antenna, and the RTD-mesa area in order to achieve the maximum oscillation frequencies.

Further, the thesis shows that the output power of symmetrical-slot-antenna RTD oscillators depends on the slot-antenna width. Although the dependence is not very strong for wider slots, it is essential for fine tuning the oscillator performance. In this work, we present an extensive set of experimental data on RTD oscillators with different slot widths. The data reasonably agree with the theoretical analysis and support its validity. Some oscillators exhibit the output-power level close to the state-of-the-art for fundamental-frequency symmetrical-slot-antenna RTD oscillators in the frequency range of 150-400 GHz. Specifically, we report 283 μW at 184 GHz and 82 μW at 368 GHz. The RTD we used in this work has 1.6 nm thick barrier with the peak current density is only ~ 5.8 mA/μm^2. In addition, the RTD oscillators were fabricated using only optical lithography.

Lastly, the thesis presents an island slot-antenna RTD oscillator, where the contact n++ layer is removed everywhere except for a small island under the RTD. At frequencies around 2 THz, this design leads to a significant reduction (by a factor of ≈ 2) of the total ohmic losses at the conducting surfaces of the slot antenna. With this design, we demonstrate the highest radiated power for RTD oscillators in the frequency range 1.6-1.74 THz with around 2.2 μW at the fundamental frequency of 1.74 THz. The RTD used in this work has 1.0 nm thick barrier, and its peak current density is 23.6 mA/ μm^2. We further demonstrate that

the oscillation frequency above 2 THz should be reached if the RTD contact resistance is reduced to 1-1.5 $\Omega\mu m^2$.

Table of contents

List of figures

List of tables

Chapter 1

Introduction

1.1 Purpose and outline of the thesis

Resonant-tunneling-diode (RTD) oscillators are considered to be one of the most promising sources for practical applications, since sub-THz and THz RTD oscillators are simple and compact sources at room temperature. Although different types (slot- and patch-antenna, composite, membrane, waveguide-based, etc.) [1–8] of RTD oscillators were developed, the state-of-the-art performance with regard to high operating frequencies and high output power (from a single oscillator) has been achieved with slot-antenna RTD oscillators so far [9], [10]; even better performance in the terms of the output power was demonstrated with double-RTD oscillator configurations (which could also be deemed as single oscillators) and with coherent arrays [6], [8], [11]. Two basic variants of slot-antenna RTD oscillators are with symmetric and asymmetric slots [3], [10], [12]. A higher output power can be achieved with the latter ones, although they have a tilted radiation pattern [10], [11], complicating their practical use. The former ones exhibit lower output power, but their radiation pattern is symmetrical (due to the symmetry of the structure), which simplifies coupling of such oscillators with the Gaussian optics of free-space THz systems, dielectric waveguides, and that is also of advantage for power combining in array configurations of oscillators [11], [13]. Therefore, our focus in the thesis is on symmetrical slot-antenna RTD oscillators.

Optimizing the design of the slot antenna is one of the key factors to improve the performance of the RTD oscillators. The impact of slot-antenna width on the output power of symmetrical slot-antenna RTD oscillators has not been analyzed and experimented yet. In addition, to achieve higher oscillation frequencies of the RTD oscillators, the losses in the resonator/antenna must be reduced.

The thesis had two main purposes: providing a set of experiment data on symmetrical slot-antenna RTD oscillators with different slot-antenna widths to match and support the validity of the theory analysis of the impact of the slot widths on the output power, and developing an RTD oscillator for high oscillation frequencies with high output powers by reducing the antenna losses. The target value of the oscillation frequency was 2 THz.

The initial chapter provides an introduction to the THz frequency range and the emerging applications that operate within this frequency region. The construction of THz sources and types of these sources are also described in this chapter. In the second chapter, we introduce the operation principle, and the structural parameters of RTDs. We describe the development, and some different types of the RTD oscillators. In addition, we mention some key factors for the consideration when designing RTD oscillators, and describe the simulation model of the RTD oscillators. The third chapter introduces the structure design of the symmetrical slot-antenna RTD oscillators, and the fabrication processes. Finally, we adjust some factors that limit the oscillation frequencies of the RTD oscillators. In the fourth chapter, we provide a variety of experiment data with fine-tuning slot-antenna width to maximize the output power of the RTD oscillators to verify the theory. The fifth chapter proposes an island design of the symmetrical slot-antenna RTD oscillators which allows the oscillators to work at high oscillation frequencies close to 2 THz. In the present work, the oscillation frequency of 1.74 THz with the output power of 2.2 μW have been achieved with this type of RTD oscillators. The conclusion and the future outlook are discussed in the sixth chapter of the thesis.

1.2 Overview about terahertz gap

Terahertz (THz) radiation is basically defined as the electromagnetic spectrum with frequencies between 100 GHz and 10 THz with corresponding wavelength λ = 3 mm - 30 μm. In some references, it is also referred to as the frequency between 300 GHz - 3 THz, see e.g. [14], [15]. This frequency range lies between the upper edge of the traditional microwave electronics and lower edge of the optical wave range, and has been underdeveloped in comparison with the other neighboring bands because of the lack of coherent, compact, and efficient THz sources and detectors. However, the THz frequency range has been developing these days thanks to the development in nanotechnology for photonics and electronics that enables terahertz research and applications, such as imaging, spectroscopy, and ultrahigh-speed wireless communication.

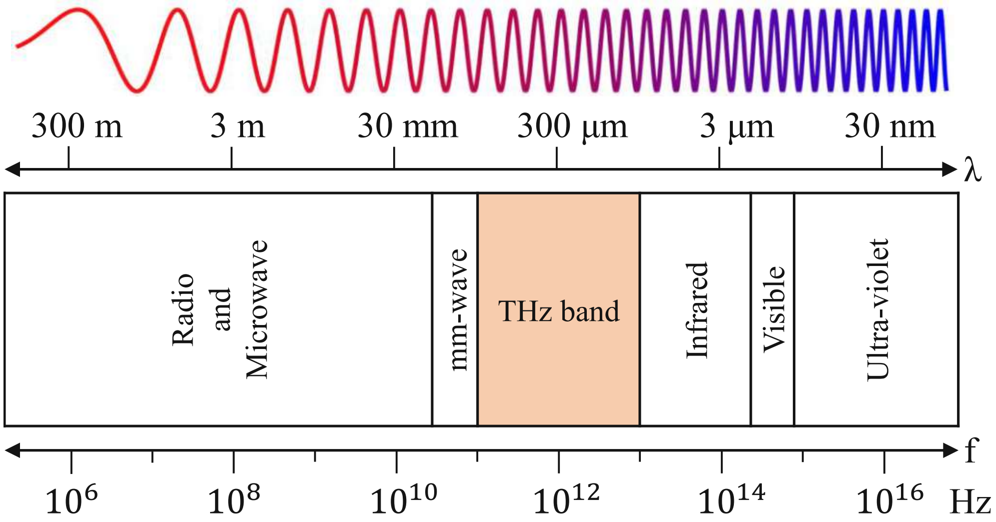

Figure 1.1: THz gap in the electromagnetic spectrum

The THz band lies between mm-wave and infrared frequency ranges, and is shown in the electromagnetic wave spectrum as in Fig. 1.1. The THz band was named in several ways, such near-millimeters wave, sub-millimeter, and far infrared.

The 1 THz radiated signal has 300 µm wavelength in free space, with the period of 1 ps, and photon energy is 4.14 meV. THz waves are sandwiched between microwave and optical bands, and have mid-features of these two frequency bands. These characteristics are summarized as followings:

- Transmissivity like radio wave: THz radiation has a longer wavelength than infrared radiation, hence it scatters less and has deeper penetration (in the range of cm) through materials than infrared radiation (in the range of µm). Materials including paper, plastics, ceramics, wood, and textiles are therefore transparent in this range yet opaque in visible light.

- Directivity similar to light wave: Compared to microwave waves, THz waves have shorter wavelengths, which improves the spatial imaging resolution. In reality, terahertz radiation can be used to study the internal structure of materials like plastic and wood by transmitting through them.

- Spectral fingerprint: The THz range is home to many molecules' inter- and intra-vibrational modes.

- Safety: Compared to X-rays, the photon energies in the THz range are substantially lower. Unlike X-rays, terahertz waves do not have any ionizing effects and are generally considered biologically innocuous.

Terahertz imaging and spectroscopy have attracted a lot of attention among terahertz applications [16], [17]. Several scientific fields, such as pharmacology, medical science, biology, material science, non-destructive evaluation, security, astronomy, and art, use imaging and spectroscopy of various materials. Terahertz communication also has the capacity to transmit and receive enormous amounts of data. Similar to optical communication systems, terahertz transmissions are anticipated to be used as information carriers with a 1 Tbps data transfer rate. The next frontier of wireless communication is now being established in this field of study [18], [19].

THz systems and applications are beginning to appear in some commercial applications as a result of recent advancements in the THz research sector. However, a number of problems need to be addressed and/or improved before THz waves can compete with and outperform other technologies in real-world applications. For example, technologies for a faster THz beam scan are needed, high-power and small THz sources are needed, THz measurement systems should be shrunk, and THz systems should be more affordable.

As seen in the following section, recent advancements in electronics and photonics are enabling terahertz research and a wide range of applications, including those in wireless communication, imaging, and spectroscopy.

1.3 Terahertz applications and sources

1.3.1 Terahertz Application

Researchers primarily worked on a variety of prospective THz applications throughout the last decade of the 20th century and the first decade of the 21st century, and highly encouraging findings were produced. In fact, those intriguing experimental findings served as a strong incentive for many researchers to delve into the THz field and examine it from many angles. Terahertz radiation has a wide range of possible uses, including terahertz imaging, spectroscopy, and wireless communication.

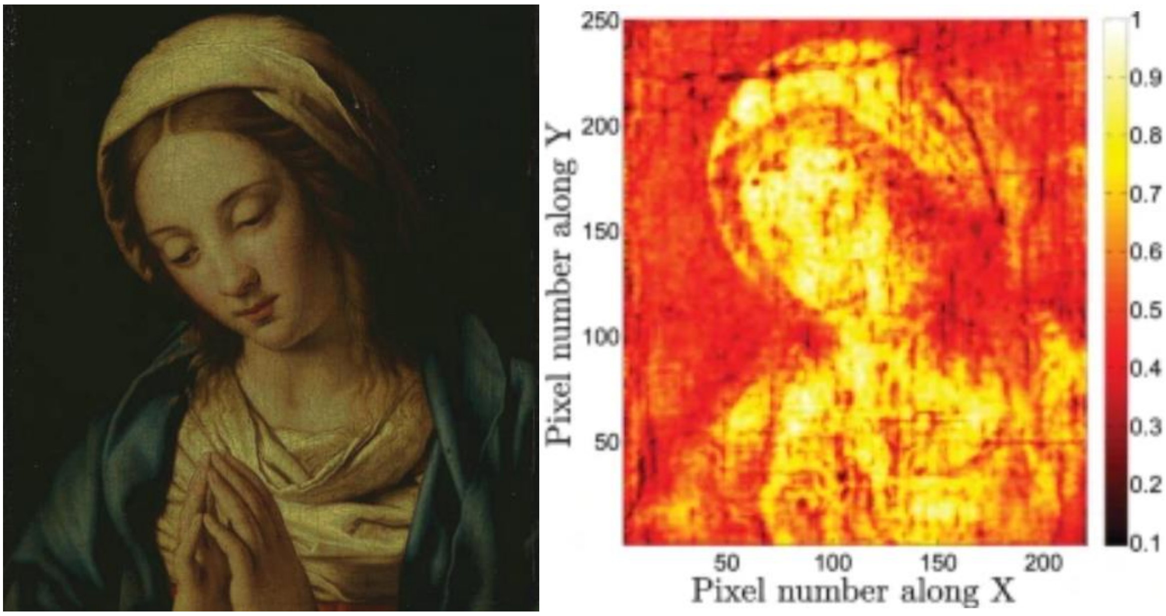

Figure 1.2: (a) visible photograph of the Madonna in Preghiera (b) THz image of the Madonna in Preghiera on the integrated spectrum between 0.5 and 1 THz. Image from [20]

Imaging

Paper, clothing, polymers, and even leaves can be penetrated by terahertz vibrations. Using X-rays, it is challenging to find these soft materials. Because terahertz wavelengths are shorter than millimeter wave wavelengths, terahertz imaging has a higher resolution than millimeter wave imaging. For non-destructive testing and non-invasive inspection of various opaque materials to learn more about the interior structure, these properties are appealing. Using a backward-wave oscillator, imaging in the terahertz range has been created for a number of applications, including plastic card examination [21]. Various studies have been reported, such as a real-time standoff imaging has been achieved using a quantum cascade laser [22]. Noninvasive mail inspection systems [23], waveguide-based all-electronic imaging [24], and food inspection [25] have also been explored. Furthermore, terahertz imaging with silicon MOSFETs has been investigated [26].

One of the subcategories of THz imaging is biomedical imaging. THz medical imaging can be used for body surface diagnoses such skin, mouth, as well as dental imaging, because THz waves can penetrate human tissues up to a few hundred micrometers. Moreover, security applications, the detection of solid explosive materials, and mail screening are prospective markets for THz systems. Fig. 1.2 shows a visible image of the Preghiera Madonna (left) with a THz image of the artwork created using an integrated spectrum between 0.5 and 1 THz (right).

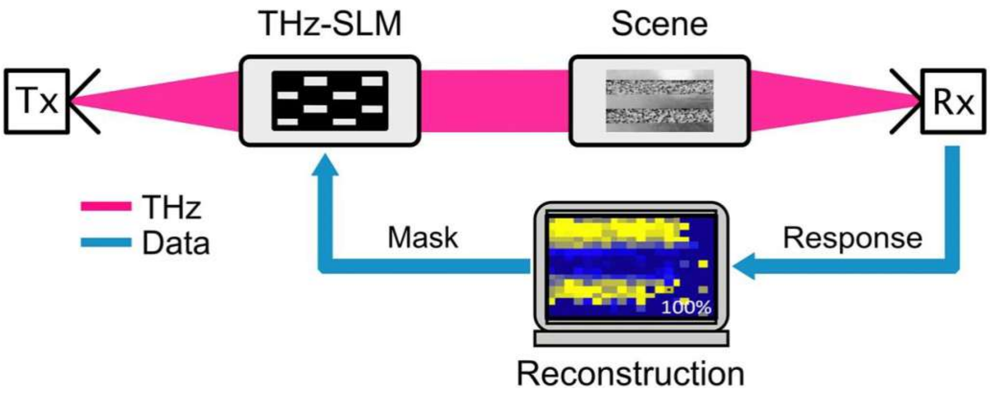

Figure 1.3: Scheme of the imaging process encountered in a THz-SPC (single-pixel camera). Image from [27].

Fig. 1.3 displays a schematic of an imaging system transmission. The beam coming from the THz source (Tx) is spatially modulated by a THz-SLM (spatial light modulator). The spatially modulated THz beam is directed to the scene of the camera and the radiation coming from the scene is detected using a single-pixel detector (Rx). With the knowledge of the spatial modulation patterns in connection with the measured responses an image of the scene can be reconstructed using a non-linear reconstruction algorithm.

Spectroscopy

Terahertz spectroscopy has also been the subject of significant study to create a variety of applications, including those in the sectors of security, pharmacology, and biology. This is similar to the development of imaging applications. Methods of inspection for illegal substances and explosives have been studied. Security-related research of a similar nature has been published. Investigations into carcinoma were conducted in the realm of biochemistry.

A particularly effective method for characterizing material qualities and comprehending their signature in this band is THz spectroscopy. Understanding of the absorption characteristics in several single-crystal, microcrystalline, and powder samples of organic compounds has improved thanks to THz spectroscopy. Fig. 1.4 shows a measurement result of a sample to identify the vibrational modes of maltose molecules [28].

The analysis of pharmaceutical solid dosage forms, tablet coatings, and active pharmaceutical components may also be done non-invasively using THz imaging and spectroscopy, which are both effective quantitative and qualitative techniques. For instance, Fig. 1.5 depicts the coating layer thickness variance amongst tablets for eight tablets coated at the same time in the THz area [29].

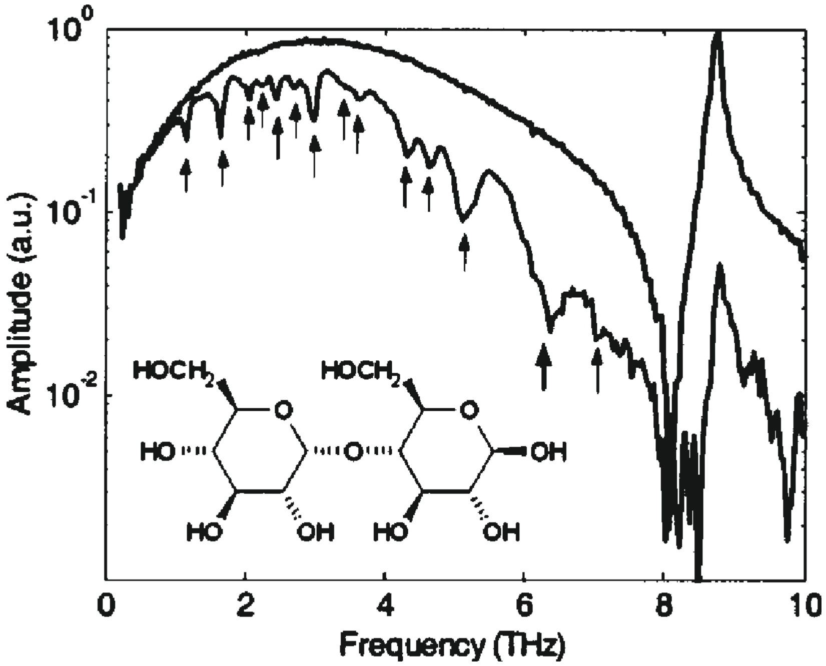

Figure 1.4: The measured vibrational spectrum of maltose in a THz time domain spectroscopy system, the upper graph shows the measured THz signal without a maltose sample. Arrows on below graph show the vibrational frequencies of maltose molecules. Inset shows the molecular structure of maltose. Image from [28].

In Fig. 1.6, an example of a transmission spectroscopy system is shown.

Wireless communication

THz wireless communication is another emerging study area. Because it enables high-speed wireless communications for networks beyond 6G, this is especially in demand, see [30]. In order for the THz band to mature and realize its full potential, numerous research are required. In the future, everything will be Internet-connected. The market for information and communication technologies is large. The rate of information transfer in contemporary civilization is increasing, and signal carrier frequencies are rising. The data rate of wireless communication continues to be low in comparison to that of fiber-linked optical communication, which is successfully expanding and achieving data rates surpassing a terabyte per second.

The idea of using THz frequency range for wireless communication has been proposed in the late 1990s. The first successful demonstration of THz wireless communications was reported in 2004, see [31]. One notable illustration involves the development (by Nippon Telegraph and Telephone Public Corporation (NTT) and Fuji Television Network) of

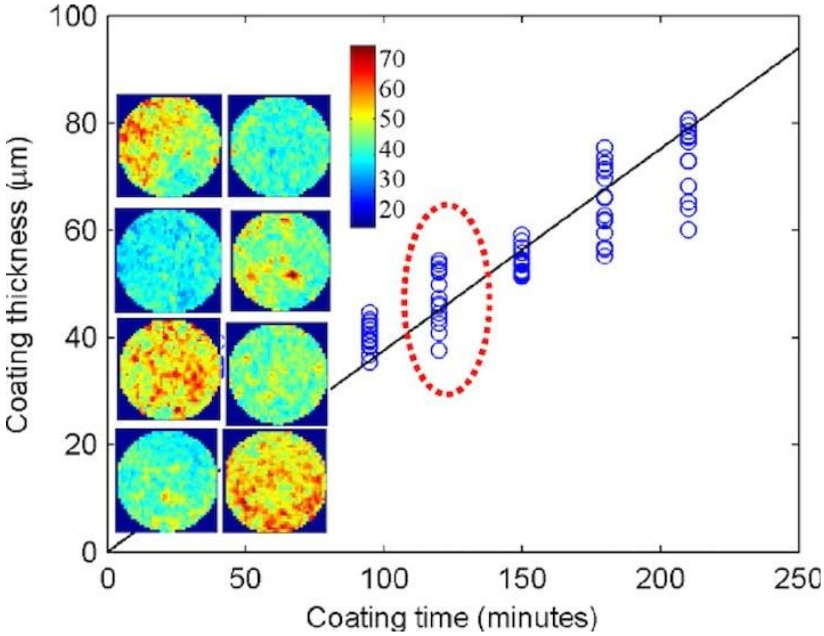

Figure 1.5: The averaged coating thickness of each individual tablet against the coating time, The inset shows the coating thickness map (um) of eight tablets with the same coating time of 120-min. A large tablet-to-tablet variation of coating thickness is obvious. Image from [29].

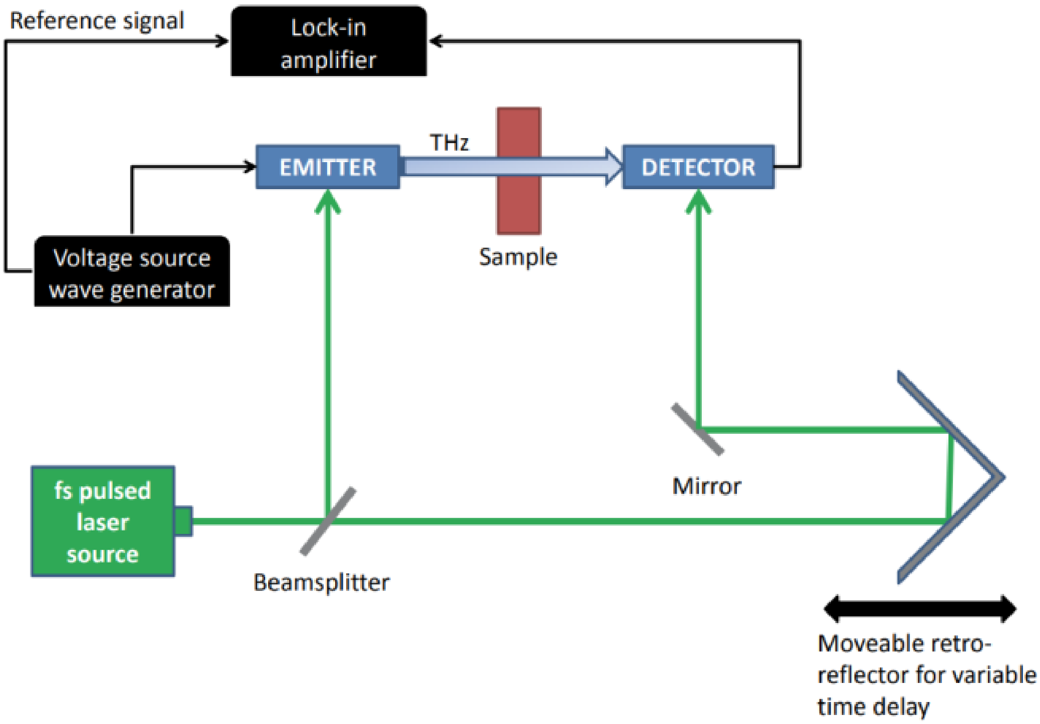

Figure 1.6: Simplified schematic diagram of a time-domain terahertz spectromete.

120-GHz-band millimeter-wave wireless links that utilize uni-traveling-carrier photodiodes (UTC-PDs) integrated with high-electron mobility transistor (HEMT) monolithic microwave integrated circuits (MMICs). These advancements have been tested successfully to operate at speeds exceeding 10 Gbps at the 2008 Olympic Games in Beijing [32]. The successful transmission of data without any errors has been achieved at a bit rate exceeding 12.5 Gbps at a frequency of 720 GHz in 2019 [33]. This accomplishment was made possible by utilizing a transmitter based on photodiodes and a receiver employing a Schottky-barrier-diode mixer.

In order to facilitate the above-mentioned applications, it is imperative to acquire appropriate terahertz (THz) sources capable of emitting THz radiation. The concept of THz sources will be described in the following subsection.

1.3.2 Terahertz sources

There are fundamental problems in the way of the development of THz sources. We can classify the issues in accordance with optical and electrical devices as they close the THz gap. Oscillations are produced by electronic devices as a result of the periodic movement of electrons within a single band. After that, electromagnetic waves are created as a result of the acceleration of the charge. On the other hand, optical devices are capable of producing electromagnetic waves through the process of electron transitions occurring between electronic bands present within the active material. The transitions can be either spontaneous or stimulated.

In the following subsections; we describe the problems on the electronic and optical sides, and address some electronic and optical sources working in the THz range. For a comparison of THz sources, see Fig. 1.7. In the comparison, we show only some candidates for compact sources. The figure shows the gap between the electronic and optical sources at around 1 THz.

Electronic THz sources

Electronic THz sources use the properties of semiconductors to produce terahertz radiation. These sources typically operate at room temperature, have high output power, and can generate continuous wave or pulsed terahertz radiation. The electronic sources cover the THz gap from the side of low frequencies.

The electronic devices are limited by an RC time constant of the RC circuit. The RC circuit is derived from the presence of parasitic elements within the physical device, specifically Ohmic losses and parasitic capacitances, and it limits the output powers and

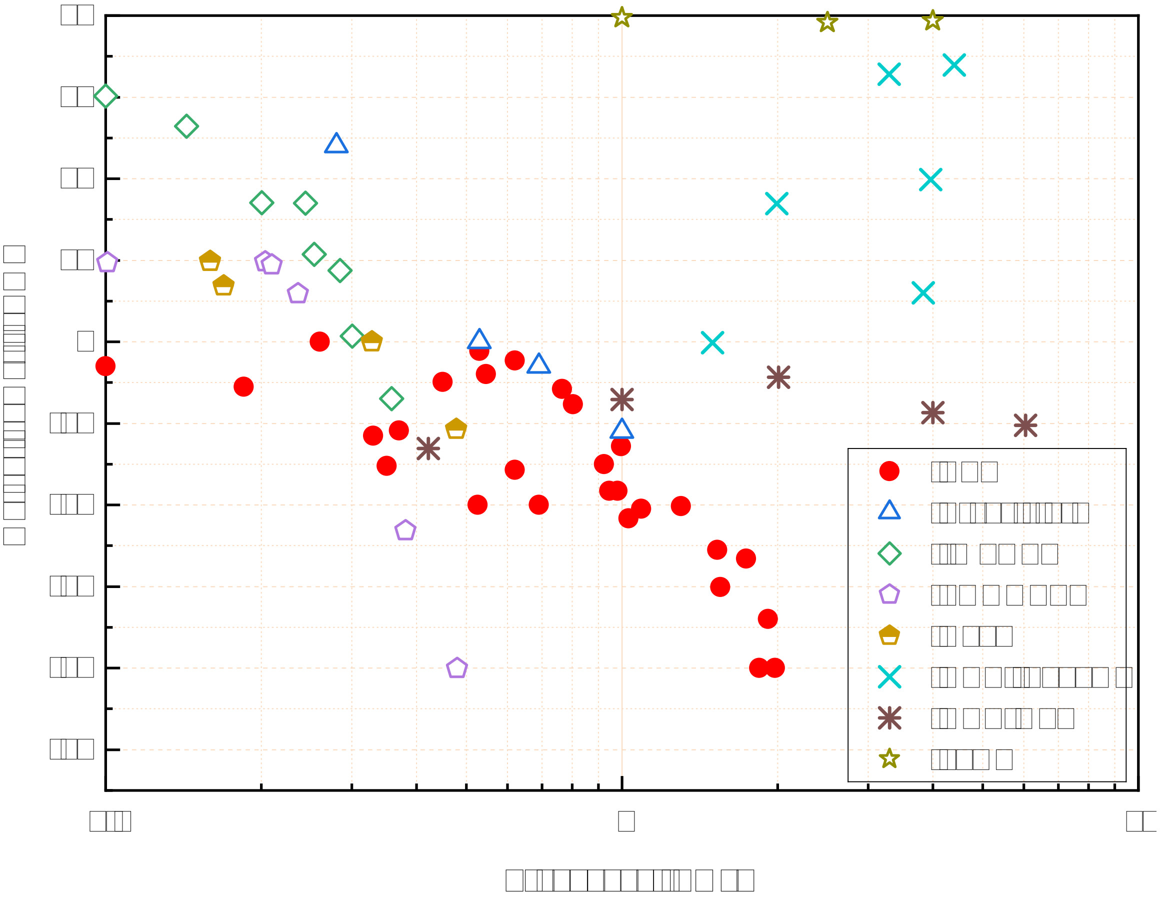

Figure 1.7: Current status of terahertz (THz) sources. Output power as a function of generated frequency. The optical sources (THz QCL and QCL-DFG, p-Ge) cover the high frequencies, and the electronic sources (the rest of the listed devices) cover the low frequencies. The THz QCLs need to be cooled down.

maximum operating frequencies. To address this problem, one needs to reduce the parasitics by minimizing the dimensions of the devices, or by doing proper fabrication processes.

We will start with some electronic devices which can exhibit the negative differential conductance (NDC) or resistance (NDR). In the NDC region, the current decreases with the increase of the voltage. These devices work actively in the NDC region as the NDC can provide the gain to compensate for the losses in the electrical resonators, hence generates the steady oscillations. These devices can be operated at the sub-THz and THz frequency range. Some devices can be listed here like Esaki, Gunn, IMPATT, TUNNET... diodes, and resonant tunneling diodes (RTDs).

Esaki diodes is one of the first sub-THz sources in the electronic field. This diode is also called tunneling diodes. Esaki diode is a composition of a connection of highly n- and p-doped semiconductors which can exhibit the negative differential conductance (NDC) region. The highest fundamental oscillation frequency was reported at 103 GHz on a GaAs tunneling diode, see [34]. The theoretical oscillation frequencies of Esaki diodes have been reported at around 200 GHz, see [35]; however, it was never experimentally demonstrated.

One of the most widely used electronic THz sources is the Gunn diode, which operates by exploiting the negative differential resistance (NDR) of certain materials. When a voltage is applied to a Gunn diode, the electric field causes the electrons to gain energy, which in turn causes them to move more quickly. However, when the electric field reaches a critical value, the velocity of the electrons decreases, leading to a negative differential resistance. This negative resistance can be used to generate terahertz radiation through a process called transit-time oscillation. The highest achieved oscillation frequency (the third harmonic) of around 455 GHz wih an output power of 23 μW were reported on the free-running oscillator with InP Gunn diode [36]. The theoretical oscillation frequencies of Gunn diodes composed of GaN have been reported to be 3 THz, as documented in reference [37]. However, they have not been experimentally confirmed for more than two decades.

Impact ionization avalanche transit-time (IMPATT) diodes [38], tunneling transit-time (TUNNETT) diodes [39] are other diodes which exhibit NDC region in the sub-THz frequency range. An oscillation frequency of 706 GHz with an output power of 0.2 μW were achieved with a TUNNETT diode in a waveguide, see [40].

Transistors are three-terminal devices. The transistor behaves as a two-terminal device with NDC when a positive feedback loop is created, either through external circuit or through inverse transmission of the transistor, see [41]. Electronic THz sources have been investigated using heterojunction bipolar transistors (HBTs) [42], high electron mobility transistors (HEMTs) [43], and complementary metal-oxide-semiconductor (CMOS) [44] transistors.

Resonant-tunneling diodes (RTDs) are the next electronic devices which explore the resonant-tunneling phenomena of electrons through a double-barrier (or triple-barrier) structure. These devices also exhibit negative differential conductance. The first above 1 THz frequencies had been reported in 2010 [45], and in 2011 [5] on the slot antena RTD oscillators. The highest oscillation frequency of 1.98 THz of RTD oscillators was achieved in 2017 [9]. The highest output power of 11.8 mW at the oscillation frequency of 450 GHz had been received in 2022 [6]. We describe RTDs in more details in Chapter 2 as they are essential part of the thesis.

Optical THz sources

The optical sources cover the THz gap from the high-frequency side. The optical sources can operate in a pulsed or continuous wave (CW) regime and at temperature much smaller than 0°C because their working principles are based on lasers and the energy of the THz photon is smaller or closed to the thermal energy at room temperature.

A type of optical THz sources is the quantum cascade laser (QCL), which operates by exploiting the quantum mechanical properties of semiconductors. QCLs consist of a series of semiconductor layers (each with a slightly different energy level) in which each layer is made up of an injector and active region. In the active region, a population inversion exists and electron transitions to a lower energy level occur, emitting photons at a specific wavelength. The electrons then tunnel between quantum wells, and the injector region couples them to the higher energy level in the active region of the subsequent repeat unit. QCLs can produce high-power terahertz radiation that makes them useful for many applications. The infra-red QCL designs were optimized and simplified, which allowed the QCLs to operate in the THz range (THz QCL). However, QCLs sources need to be operated at far below zero degrees Centigrade, see [46]. The quantum cascade laser (QCL) was initially created in 1994, and subsequent to extensive research, a demonstration was conducted at a frequency of 4.4 THz in the year 2002, see [47]. THz QCLs were proved in pulsed regime that they can emit the oscillation frequencies in the range from 1.5 to 6 THz with the output power up to 2.5 W, see [48], [49].

One additional principle for the use of QCLs in the generation of THz waves is known as difference frequency generation (DFG). This principle involves the utilization of a QCL that generates two distinct lasing modes characterized by disparate wavelengths. The frequency difference between the modes corresponds to a frequency in the THz range. The utilized QCL functions within the infrared spectrum, obviating the need for cryogenic cooling. Consequently, the QCL- DFG technique is capable of producing THz waves at room temperature. These sources also have the potential to operate within the sub-THz range. QCL-DFGs have been successfully operated within the frequency range of 0.42 THz to 6 THz, exhibiting a maximum output power of 1.4 mW in pulsed mode, as reported in references [50] and [51].

Another approach for generating optical THz waves involves the utilization of a femtosecond laser to generate terahertz radiation through a process called photoconductive switching. This process involves illuminating a photoconductive material with a femtosecond laser pulse, which generates a transient population of free carriers. When an electric field is applied to the material, these carriers can be accelerated, leading to the emission of terahertz radiation.

The photoconductive material used in these sources is typically a semiconductor, such as gallium arsenide or indium phosphide, which has a bandgap energy that is smaller than the photon energy of the laser pulse. When the laser pulse is absorbed by the semiconductor, it generates a population of electron-hole pairs, which can be separated by the applied electric field.

The p-Ge laser is considered as the most powerful THz source, capable of generating an output power in the range of several watts, see [52] and [53]. The p-Ge laser operates by utilizing hole intervalence band transitions within the germanium semiconductor material. Recent papers report an output power from a p-Ge-laser of up to 10 W, see [54]. The main disadvantages of this kind of laser are the operational requirements for a cooling dewar, high magnetic, and pulsed electric fields.

Optically pumped THz lasers are another type of optical THz sources. The generation of optically pumped THz lasers can be achieved through the process of signal mixing, wherein two signals characterized by distinct optical wavelengths are combined, resulting in a frequency difference that corresponds to the desired THz signal frequency. The very narrow emission lines (1 MHz or fewer) produced by optically pumped lasers are one of its primary benefits. These emission lines are responsible for the extremely high spectrum brightness of these THz sources as well as their high output power. The system can reach a maximum output power of 1.5 mW and is capable of functioning across a wide frequency range, spanning from tens of GHz to 2 THz. At a frequency of 1 THz, the output power is in the range of tens of µW, as referenced in [55].

Chapter 2

Resonant-Tunneling-Diode (RTD) Oscillators

In this chapter, we introduce the operation principle, and the structural parameters of RTDs. Next, we describe the general oscillation conditions of an oscillator. Then the development, and some different types of the RTD oscillators will be discussed at the end of the chapter.

2.1 Introduction to resonant-tunneling-diode oscillators

THz frequency range is expected to be important for many applications [56], but its practical use is hindered by the lack of sufficiently-simple solid-state room-temperature radiation sources. Among available technologies, resonant-tunneling-diode (RTD) oscillators are deemed to be one of the most promising for practical use, since sub-THz and THz RTD oscillators are very simple [3], [4], compact [5], they work at room temperature, cover the frequencies up to almost 2 THz [9], can provide relatively high output power radiated into free space (several hundred μW by stand-alone oscillators and up to $\approx 10\,\mathrm{mW}$ at 0.45 THz in coherent-array configuration) [6], [8, 10, 11], have high DC-to-RF conversion efficiency of up to 1-5 % [6], [10], [57], etc.

RTD oscillators consist of several key components. The active element is the RTD, which exhibits negative differential resistance (NDR) and acts as the gain element. The resonator determines the oscillation frequency of the oscillator. There is also a biasing circuit and an external bias source that provide the necessary energy for the oscillator to function. Additionally, an antenna is included to transmit the generated oscillations to the external environment. In current advanced oscillators, the resonator and antenna are often combined into a resonant antenna, which directly radiates the electromagnetic waves generated by the oscillator.

Numerous examples of the RTD oscillator's employment in real-world applications have previously been published, including the following: wireless communication [58], [59], imaging [60], spectrometer [61], radars [62], [63], etc.

2.2 Resonant-tunneling diodes

The concept of resonant tunneling through the quantum states between double barriers was earlier described in a textbook in 1951 [64]. The operation principles about negative differential conductance (NDC) of the device based on the phenomenon was mentioned in 1965 [65]. In 1973, Chang, Tsu, and Leo Esaki predicted resonant tunneling in heterostructures, see [66]. Experimental demonstrations of NDC in such device structures was subsequently shown in 1974 [67]. This work laid the foundation for the development of resonant tunneling diodes. The conducting layers were composed of GaAs, while the barriers consisted of AlGaAs. Nevertheless, this result was obtained at a temperature of 77K, which corresponds to the boiling point of liquid nitrogen. The first RTD with negative differential conductance (NDC) working at room temperature was successfully created in 1985, as referenced in [68]. This achievement was made feasible by modifying the layers and enhancing the quality of the films grown using molecular beam epitaxy (MBE).

In the years 2010 and 2011, a significant progress was made in the field of RTD oscillators with two separate groups successfully reporting oscillators operating at the fundamental frequency of $\approx$ 1 THz [45] and $\approx$ 1.1 THz [5], respectively. Over time, the operational frequencies of RTD oscillators have experienced a continuous increase, with current frequencies reaching nearly 2 THz, as reported in reference [9]. In comparison with THz quantum-cascade lasers (QCLs) [46], oscillators bases on RTDs can operate at room temperature, which constitutes a pivotal benefit over THz QCLs. The output power of RTD oscillators reached to over 10 mW at the fundamental frequency of 450 GHz [6]. The recent progress in this field has established RTD oscillators as a feasible technology that can facilitate practical THz applications.

2.2.1 Theory of resonant-tunneling-diode operation

At first, we shortly describe about a phenomenon called quantum mechanical tunneling which will help us clearly understand about the operation principle of the RTDs.

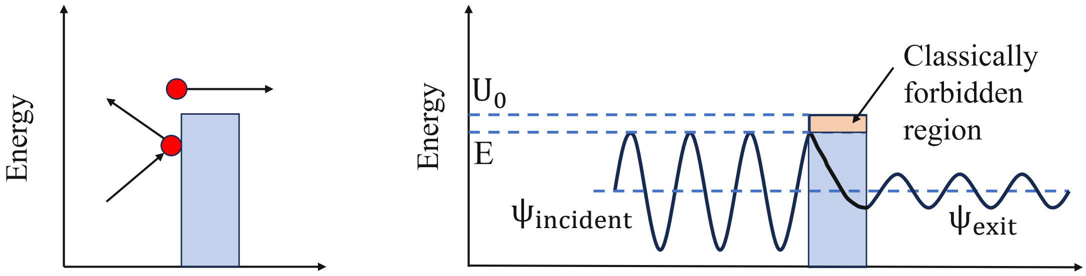

(a) Classical view (b) Quantum mechanical view

Figure 2.1: Rectangular potential barrier and particle wave function.

The term "quantum mechanical tunnelling" refers to a phenomenon that is utilised by all varieties of tunnelling diodes, including double, triple, and super-lattice types. Quantum tunnelling refers to the process in which electrons are able to travel through a potential barrier with a height greater than the total energy of the electrons.

For more details about quantum mechanical tunneling, see [69]. This paragraph only summaries some main features of this phenomenon. In classical physics, an electron must have sufficient energy to surmount a barrier; otherwise, it rebounds from the barrier, see Fig. 2.1a. Electron tunnelling through potential barriers occurs due to the quantum mechanical wave nature of particles, an effect forbidden in classical physics. As the wavefunction of the particle is required to be continuous at the barrier, there is a finite probability that a particle (with energy E) will tunnel through the potential barrier U_0, see Fig. 2.1b. The transmission coefficient through the barrier can be expressed as:

$$T \approx e^{-2\alpha d} \tag{2.1}$$

with:

$$\alpha = \sqrt{\frac{2m(U_0 - E)}{\hbar^2}} \tag{2.2}$$

where: d is the width of the potential barrier, m is the effective mass of the electron, and $\hbar$ is the reduced Planck's constant.

The more rigorous treatment of the transmission coefficient gives the expression:

$$T = \left\{1 + \frac{1}{4}\left[\frac{U_0^2}{E(U_0 - E)}\right] sinh^2 \alpha d\right\}^{-1} \tag{2.3}$$

Now, we turn back to double barrier resonant tunneling diodes.

A double barrier resonant tunnelling diode, also known as a DBRTD, is typically made up of an undoped quantum well (QW) that is sandwiched between two undoped potential barriers and is surrounded on all sides by doped emitter and collector layers. Due to the good lattice matching that can be achieved when AlGaAs is grown on a GaAs substrate, the AlGaAs/GaAs material system has become particularly popular for use in DBRTDs.

Figure 2.2 illustrates the potential profile of the conduction band in a typical RTD. As the DBRTD is an open quantum system, the quasi-bond-states, also knows as resonant states, are generated within the QW. The operation of the RTD relies on the movement of electrons through the quasi-bound states formed in the quantum well. In Fig. 2.2, E_1 represents the energy at the bottom of the first subband, while E_2 represents the energy at the bottom of the second subband. The electrons in the contacts are distributed according to the Fermi-Dirac statistic, filling states of the contacts up to the Fermi level. The contacts are called the emitter and the collector, which is based on the direction of the electron transport in reference to the double-barrier structure. The left electrode is referred to as the emitter (cathode), and the right electrode is referred to as the collector (anode). Consequently, under an applied voltage, the electrons are considered to transport from the left side to the right side. In order to explain current conduction in the RTDs, two tunneling models have been proposed: the sequential tunneling model [70] and the coherent tunneling model [66].

The electron wave resonance of a resonant tunnelling diode is similar to optical transmission in a Fabry-Perot etalon. Let us assume that double barriers of the RTD have the tunneling coefficients T_1 and T_2, respectively. $T_1 \ll 1$ and $T_2 \ll 1$ for double barriers having weak transparent barriers individually, and the resonant part of the current is dominate over non-resonant one [65]. In this situation, the total tunneling transmission probability (T_{total}) of the DBRTD is large for electrons having the energy close to or equal to the energy levels E_1 or E_2 in the QW. T_{total} is unity for a symmetrical barriers in the resonance [64]; however, if the energy of the electrons does not coincide with any resonant states E_1 or E_2 in the QW, then T_{total} will be extremely low ($T_{total} \sim T_1 T_2$). That means the DBRTDs are typically allowed the resonant electrons to tunnel through the double barriers. T_{total} is also less than unity for an asymmetric system. The asymmetry of the DBRTDs can be introduced by making one barrier thicker, or by applying an external bias to the structure, and/or by changing the confining potential of the barrier.

The sequential tunneling process of the electrons through the DBRTDs can be summarized as following: Under the applied voltage, electrons transport from the emitter to the collector through the left barrier, the quantum well, and the right barrier. When electrons enter the quantum well, they loose their phase completely. Consequently, the movement of electrons in this situation is considered as two separate processes. Typically, the heterostructure and doping parameters of an RTD are selected to fulfill the condition that at low biases (U is

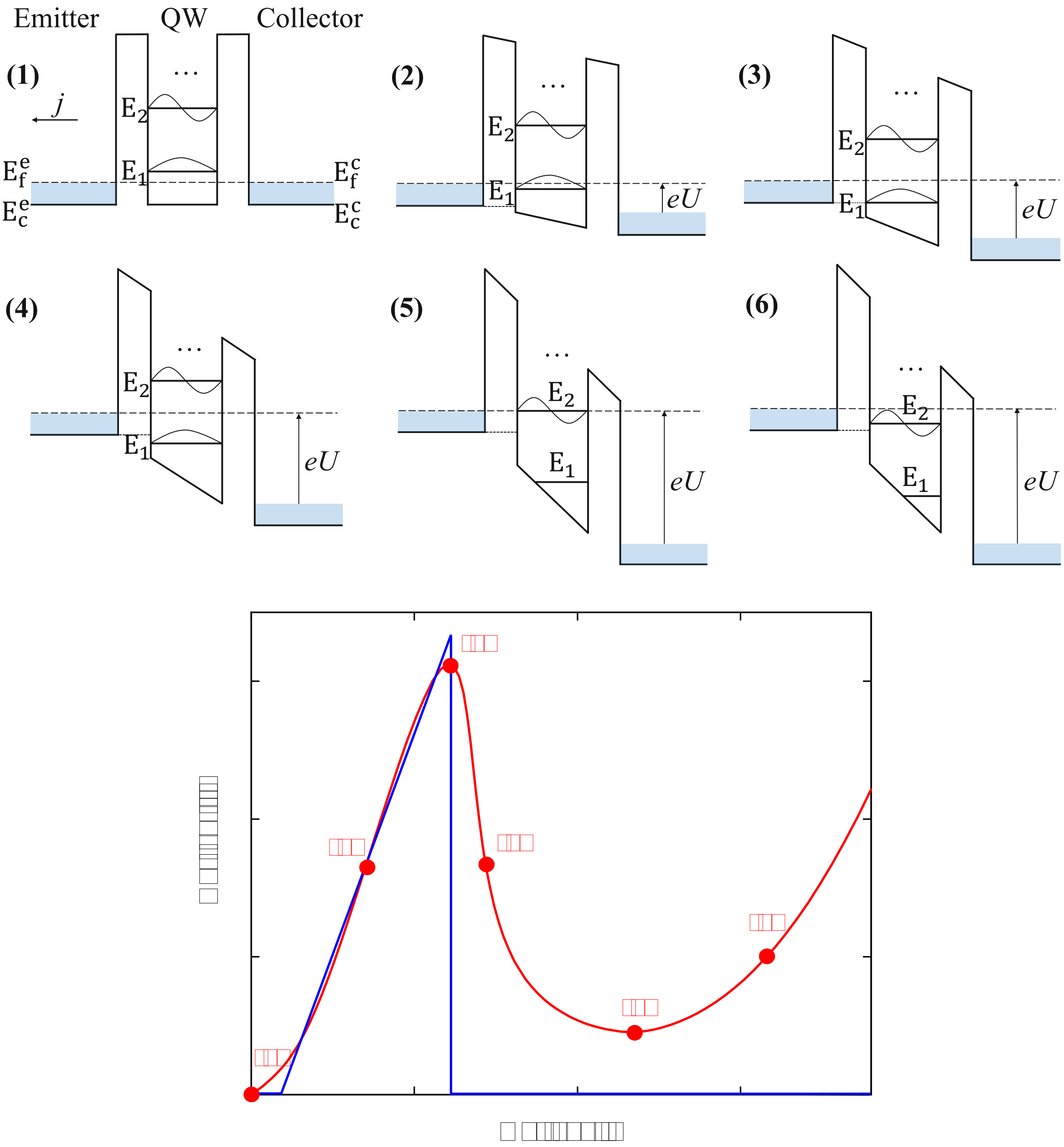

Figure 2.2: The operation principle of RTDs. The pictures from (1) to (6) correspond to different applied voltage U on the RTD. The lower diagram shows the I-V characteristics of the RTD. The blue line is an ideal I-V curve at zero Kelvins without any scattering effects, while the red one shows a real I-V curve of the RTD with red points mark indicating different bias points from (1) to (6).

close to 0), the bottom of the ground subband in the QW (E_1) is higher the Fermi level on the emitter. Consequently, for the biases close to 0 V, the emitter and the collector of the RTD have the same Fermi level position, and the double barriers structure is in equilibrium. So, the net resonant-tunneling current across the RTD is close to zero at low biases (situation (1) in Fig. 2.2).

However, when we apply bias to the RTD, this equilibrium is broken. With the increasing of the applied bias, the Fermi levels of the contacts (emitter and collector) are shifted too, and the current through the RTD starts to flow. The ground subband E_1 in the QW is shifting down below the Fermi level E_f^e of the emitter, and the resonant-tunneling current is starting to flow. The current is proportional to the number of the subband states between the emitter Fermi level E_f^e and the QW ground subband E_1; as a result, the current through the RTD keeps increasing with further increase of applied biases, and it creates one region of the I-V curve called the positive-differential-conductance (PDC) region (situation (2) in Fig. 2.2).

The current hits the maximum value (I_p - the peak current density), when the emitter conduction level E_c^e matches with the QW ground subband E_1 (situation (3) in Fig. 2.2). At this point, the current suddenly drops to flow as there are no available electrons can tunnel. In principle, the movement between the peak current density and the point where no currents flow is sharp, and it makes a triangular shape (the blue line in the I-V curve from Fig. 2.2). In reality, due to scattering effects in RTDs, imperfection structures, or not really zero temperature, etc, the I-V curve of the RTD is more smooth (the red curve in the I-V curve from Fig. 2.2), and creates the negative-differential-conductance (NDC) region (situation (4) in Fig. 2.2). Current will keep dropping with increase in bias voltage until other mechanisms take place (situation (5) in Fig. 2.2). With an increase in voltage, the density of electrons with high enough kinetic energy to pass the barrier increases, consequently the current starts to rise. When the second subband level (E_2) in the QW drops below the emitter Fermi level E_f^e, currents flow is enhanced through the second resonance condition. At this point, with an increase in voltage, the current is starting to flow as described in situation (6) of Fig. 2.2).

The coherent resonant tunneling in a double barrier structure refers to a quantum mechanical phenomenon where an electron wave can pass through two potential barriers due to its wave-like nature. This effect is observed when the energy and the momentum of the incident electron match the resonant states within the barriers, allowing it to tunnel through the barriers with high probability. At zero bias ($U = 0$), the total current flows through the double barrier structure equals zero as the tunneling current from left to right and those from right to left are equal. When bias voltage is applied to the structure, there are more electrons in the emitter are in resonance with the QW resonant states leading to an increase of the tunneling current through the double barrier structure. Close to the emitter conduction band edge E_c^e, the current reaches maximum since the number of incident electrons satisfying resonance condition reaches maximum. When the applied bias increases further, the resonant state E_1 in the QW lowers than E_c^e, and the tunneling current starts dropping to the NDC region of the I-V curve. Further increasing in the applied bias gives the rise again of the current through the higher subbands in the QW (E_2, etc.).

2.2.2 Material systems of RTDs

Optimal performance of a double barrier RTD can be achieved by judiciously selecting the material system. This enables the adjustment of barrier heights, band-gap of the materials, electron mobility, and doping concentration of the contact regions. In addition, the epitaxial layer dimensions, specifically the barrier thickness (t_b), quantum well thickness (t_{qw}), and spacer thickness (t_s), may be adjusted in order to enhance the functionality of the device. The growth parameters such as temperature and interruption time are also significant factors to consider.

Typically, semiconductor materials from III-V group are chosen to grow RTDs due to their excellent characteristics and mature growth technique. The following discussions will focus on several material systems using for the fabrication of conventional (symmetric) double barrier RTDs.

- **Gallium Arsenide based RTDs: $GaAs/Al_xGa_{1-x}As$:** After Tsu and Esaki [66] discovered and explained the phenomenon of tunneling in a finite super-lattice, researchers used $GaAs/Al_xGa_{1-x}As$ as the material system to demonstrate this phenomenon [68], [71]. In this layer structure, a GaAs well (with low band gap) was sandwiched between $Al_xGa_{1-x}As$ barriers (with high band gap). The first experiment to explain the NDC in a double barrier structure was done at low temperature (77 K) using $GaAs/Al_{0.7}Ga_{0.3}As$ material [67]. However, these earlier devices could give only a very low peak current density and no clear NDC region at room temperature. In 1987, the highest PVCR (peak-to-valley current ration) of 3.9 at room temperature of $GaAs/Al_{0.42}Ga_{0.58}As$ double barrier structure with a peak current density of $\sim 8\ \mathrm{kA/cm^2}$ was reported by Huang [71].

  The offset of the conduction band between GaAs and $GaAs/Al_xGa_{1-x}As$ is approximately calculated by the following equation [72]:

$$\Delta E_c(x) = \begin{cases} 0.748x & (0 < x < 0.45) \\ 0.6[1.247x + 1.147(x-0.45)^2] & (0.45 < x) \end{cases} \tag{2.4}$$

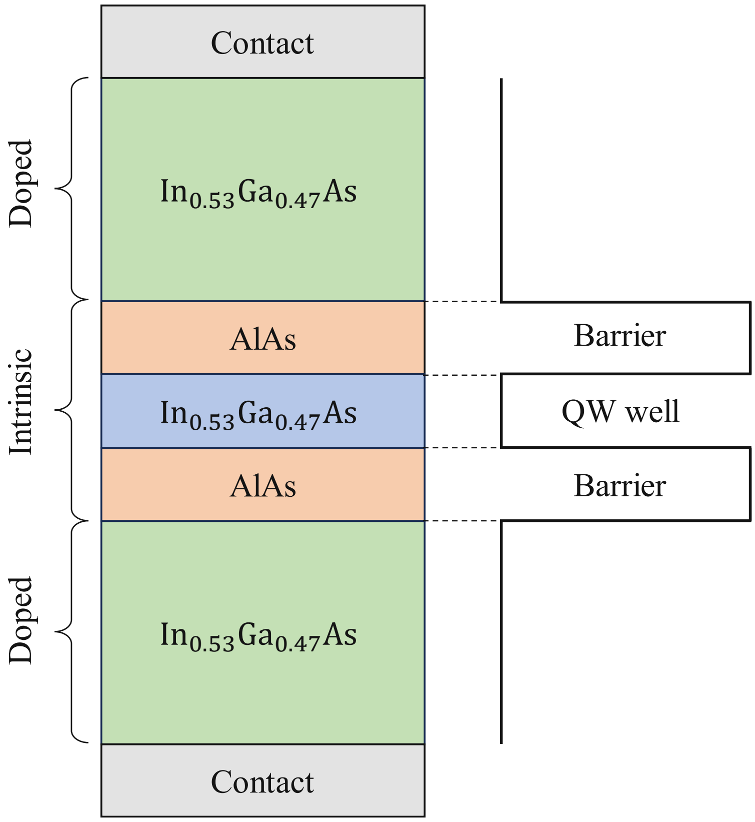

Figure 2.3: An example of an RTD layer stack up, with $In_{0.53}Ga_{0.47}As$ and AlAs layers.

As a result, the height of the $Al_xGa_{1-x}As$ barrier should be higher to achieve higher PVCR and higher peak current density on GaAs substrate. And AlAs was used as the barrier layer for this purpose.

- **GaAs/AlAs:** This material system was first used in 1985 [73], and the NDC region was observed at room temperature. Typically, the enhancement in PVCR was due to the reducing of alloy scattering in the AlAs barrier that leads to a reduction in leakage current components through the higher lying resonant levels in the QW as the barrier height was increased in AlAs. And the improvement of the peak current density was because of the increase in transmission probability. By optimization of growing this material at 580°C, the highest PVCR of 5.4 was obtained in 1994 [74], and the highest peak current density of $\sim 200\ \mathrm{kA/cm^2}$ was obtained by using thin barrier of 1.4 nm [75].
- **InGaAs/InAlAs:** High current density and low contact resistance were the main reasons behind the introduction of this material system. In 1986, the first use of $In_{0.53}Ga_{0.47}As/In_{0.52}Al_{0.48}As$ was proposed as a double barrier RTD lattice-matched

to InP substrate [76]. The electron effective mass m* of $In_{0.52}Al_{0.48}As$ barrier is about 0.075 m_0, and it is quite low in comparison to $Al_xGa_{1-x}As$ barrier. That leads to a higher peak current density. In addition, the $In_{0.53}Ga_{0.47}As$ also has lower electron effective mass ($m^* = 0.044m_0$) than that in GaAs ($m^* = 0.067m_0$). As a result, the current density is higher in $In_{0.53}Ga_{0.47}As$ due to higher electron mobility. A PVCR of about 7 and a peak current density of ~ 90 kA/cm^2 were obtained on this material system at room temperature [77].

- **$In_{0.53}Ga_{0.47}As/AlAs$** : The use of $In_{0.53}Ga_{0.47}As/AlAs$ as a double barrier RTD was first introduced in 1987 by Inata [78] with a high PVCR of 14. By adding InAs sub-well to the $In_{0.53}Ga_{0.47}As/AlAs$, the ground subband level in the QW was shifted further down, and the separation between QW subband levels was increased. A recording highest PVCR of 50 was obtained in 1991 [79] at room temperature using this variation.

  Since 2002, the $In_{0.53}Ga_{0.47}As$ quantum well was replaced with an indium-rich (80%) quantum well. The $In_{0.8}Ga_{0.2}As$ quantum well has been improved by the group of Prof. Asada to produce RTD oscillators at THz frequency range. By using this material system, the peak current density of 2300 kA/cm^2 with the oscillation frequency of 1.31 THz were achieved at room temperature in 2012 [80] by this group. An example of an RTD layer stack up, with $In_{0.53}Ga_{0.47}As$ and AlAs layers is shown in Fig. 2.3.

- **InAs/AlSb:** This material system was first proposed in 1988 by Luo [81]. Low electron effective mass and conduction band offset are the main advantages of InAs/AlSb. The electron effective mass of InAs is $m^* = 0.023m_0$, and the conduction band offset is about 1.35 eV [82, 83]. The peak current density of 100 kA/cm^2 and the PVCR of 11 at room temperature was reported with this material system in 1990 [84]. In addition, an oscillation frequency up to 712 GHz was obtained in 1991 [1] using this material structure.

In recent years, there has been a notable demonstration of a highly fascinating RTD variant that utilizes graphene as its foundation. This particular RTD configuration involves the resonant tunneling of electrons between two graphene layers, which are effectively separated by a boron-nitride barrier consisting of only a few atomic layers [85]. The occurrence of negative differential conductance (NDC) in such structures can be attributed to the misalignment of the electronic spectra in the adjacent graphene layers, which is influenced by changes in bias. These particular RTDs are anticipated to operate within the sub-terahertz frequency range [86].

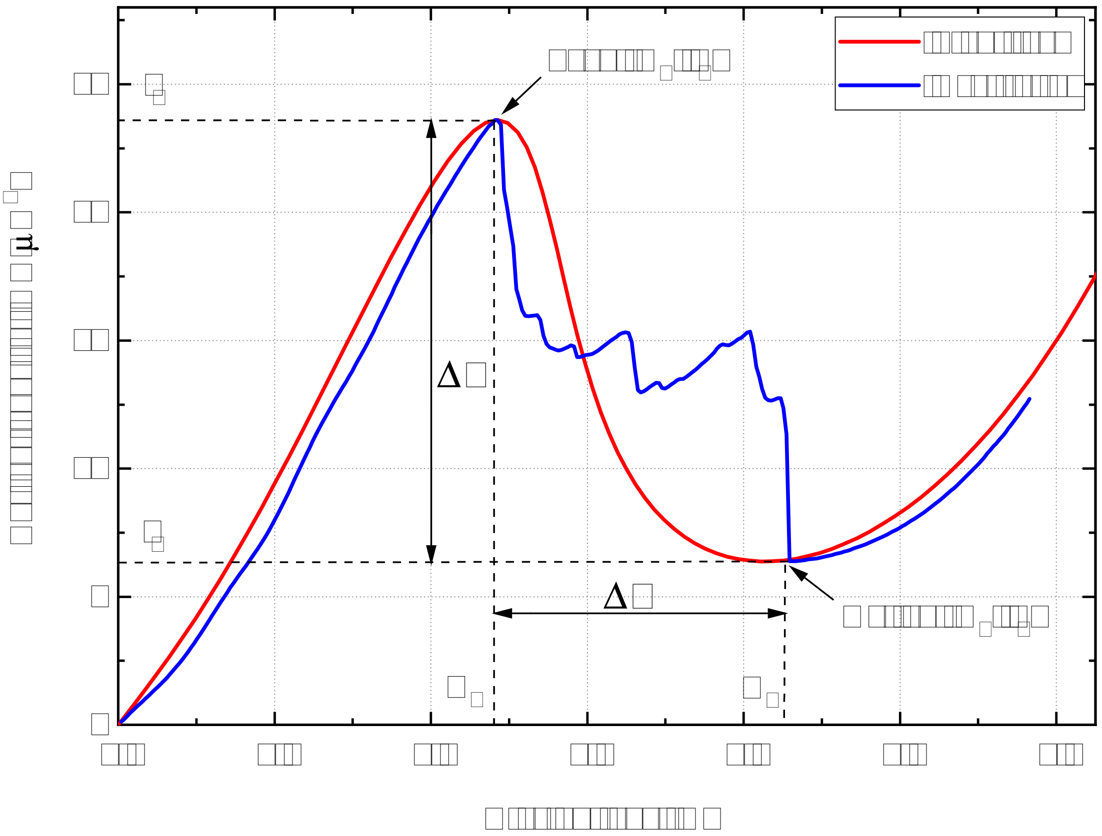

Figure 2.4: The example of an IV characteristic with clear NDC from an RTD fabricated for this work. The stabilized curve shows a result from a simulation of the RTD, and the oscillating curve corresponds to the measured data of a fabricated device with the same RTD parameters as in the simulation case.

2.2.3 Parameters of RTDs

Parameters of RTDs

There are lots of important equivalent parameters of RTDs that needs to be well-defined and adjusted to make RTD oscillators having better performance on both cases of high oscillation frequency and high output power. These RTD parameters are including: the peak current density j_{p}, the peak-to-valley current ratio (PVCR), the distance between the peak and the valley current density ΔI ($\Delta I = j_{\mathrm{p}} - j_{\mathrm{v}}$), and the difference between the peak and the valley voltage ΔV ($\Delta V = V_{\mathrm{p}} - V_{\mathrm{v}}$). These parameters are defined from an I-V curve of an RTD in Figure 2.4.

These above equivalent parameters of RTDs are determined by applying DC measurements for the I-V characteristics of the RTDs. The RTDs are oscillating during the measurement due to the NDC region of the RTDs. Stabilizing the RTD is necessary in order to produce a smooth form of the I-V curve as in the oscillating case; nevertheless, stabilization calls for extra considerations and is not an easy task to complete. For the rough analysis of the RTD oscillator, we can use the equivalent parameters of RTDs which are not required the stabilized curve for their determination.

The negative differential conductance of the RTDs, G can provide the gain needed to sustain oscillation, and depends on the current difference ΔI and the voltage difference ΔV as following:

$$G \approx -\frac{\Delta I}{\Delta V} = -\frac{j_\mathrm{p} - j_\mathrm{v}}{V_\mathrm{p} - V_\mathrm{v}} \tag{2.5}$$

G has contribution on both the output power and the maximum oscillation frequency of the RTD oscillators. The peak current density j_p and the voltage of the current peak V_p affect on the DC-to-RF efficiency. The output power is also influenced by the voltage difference ΔV. The maximum area of the RTD is affected by j_p, V_p and the thermal conductivity of the material systems used in RTD.

For Analyzing the RTD oscillators, the conductance and capacitance of the RTD are considered as a function of the voltage and frequency, and they are nonlinear. For more details, see next chapters.

Next subsections describe some physical parameters from the RTD' structure, such as the barrier, the quantum well, and the spacer thicknesses, which affect on the performance of the RTD.

Barrier thickness

We can understand the dependence of peak current density of a double barrier RTD on its barrier thickness through the transmission probability T of electrons through this layer structure. The transmission coefficient through a rectangular barrier can be expressed as:

$$T \approx e^{-2KT_\mathrm{b}} \tag{2.6}$$

and the wave vector inside the barrier is:

$$K = \sqrt{\frac{2m^*(U_0 - E)}{\hbar^2}} \tag{2.7}$$

Here $\mathrm{T_b}$ is the width of the barrier, m^* is the electron effective mass, $\mathrm{U_0}$ and E are the potential barrier and the energy of the electron, while $\hbar$ is the reduced Plank constant.

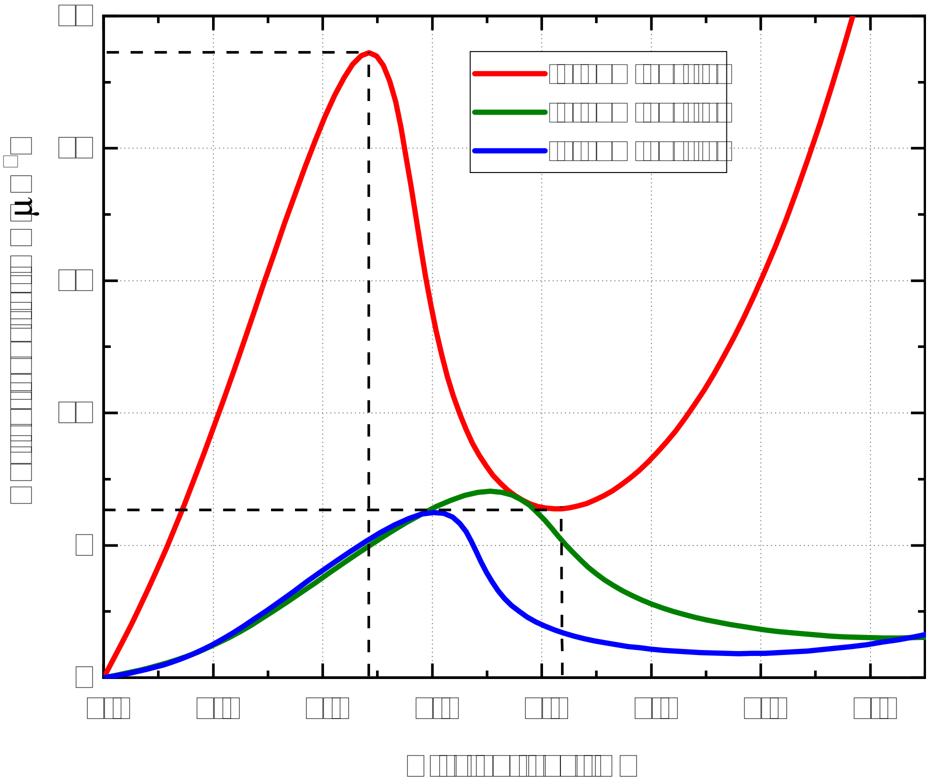

Figure 2.5: I-V curves of RTDs with different barrier thicknesses from our RTD wafer samples.

As a result, the transmission coefficient T and the current density J increase exponentially with the decrease in the barrier thickness T_b. Figure 2.5 shows I-V characteristics of RTDs with barrier thickness of 1.0 nm, 1.4 nm and 1.6 nm resulting on different peak current densities.

Quantum well thickness

As in the previous section, we also explore the dependence of peak current density through a double barrier quantum well on its QW thickness through the tunneling coefficient.
The QW subband levels is given as following:

$$E_n = \left(\frac{\hbar^2\pi^2}{2m^*T_w^2}\right)n^2 \tag{2.8}$$

where T_w is the quantum well thickness, and m^* is the effective mass of the electron.

Using the Wentzel-Kramers-Brillouin (WKB) approximation, for the n^{th} resonant level, the full-width at half-maximum (FWHM) is calculated as [69]:

$$\Delta E_\mathrm{n} = E_\mathrm{n} exp(-2T_\mathrm{b}\sqrt{\frac{2m^*(U_0 - E_\mathrm{n})}{\hbar^2}}) \tag{2.9}$$

where U_0 is the barrier height.

The transmission coefficient T(E) through a double barrier QW is approximated as:

$$T(E) = \frac{4T_1T_2}{(T_1+T_2)^2}\left[1+\frac{E-E_\mathrm{n}}{\frac{1}{2}\Delta E_\mathrm{n}}\right]^{-1} \tag{2.10}$$

where T_1 and T_2 are the tunneling coefficients through the left and right barriers respectively.

The effect of T_w on the tunneling coefficient T_E, and thus the current density of the DBRTD can be seen in ref. [80] and [87]. According to these, the current density of the DBRTD increases with reducing of the QW thickness.

Spacer thickness

In order to prevent diffusion of dopants to the subsequent layers during the process of growing materials (i.e. from the n++ InGaAs into the AlAs barrier), the undoped spacer is necessary to include to the layer structure. With the use of the undoped spacer, the mean free path of the electron is clear from ionised donors.

With the presence of an undoped spacer layer (it might be a low-doped spacer layer) between the emitter contact (negative) and the barrier, a triangular well will be created next to the barrier (on emitter side) under a large applied bias voltage, see Figure 2.6

The creation of a triangular potential well gives rise to a population of a two-dimensional electron gas (2DEG), wherein electrons are found to occupy the quasi-bound states. The outcome of this phenomenon is the occurrence of resonant tunnelling between the quantized states within the triangular well and the resonant state within the quantum well, which is commonly known as 2D-2D resonant tunnelling. As a result, an enhanced peak-to-valley current ratio is observed. However, this improvement comes at the cost of a reduced current density, see [88].

The optimisation of spacer thickness presents a clear balance between enhancing the peak-to-valley current ratio (PVCR) and reducing the peak current density J_p. It is imperative to comprehend that the presence of a thick spacer results in the widening of the depletion region, thereby leading to an augmentation in the intrinsic delay time. Consequently, the performance at high frequencies may be compromised.

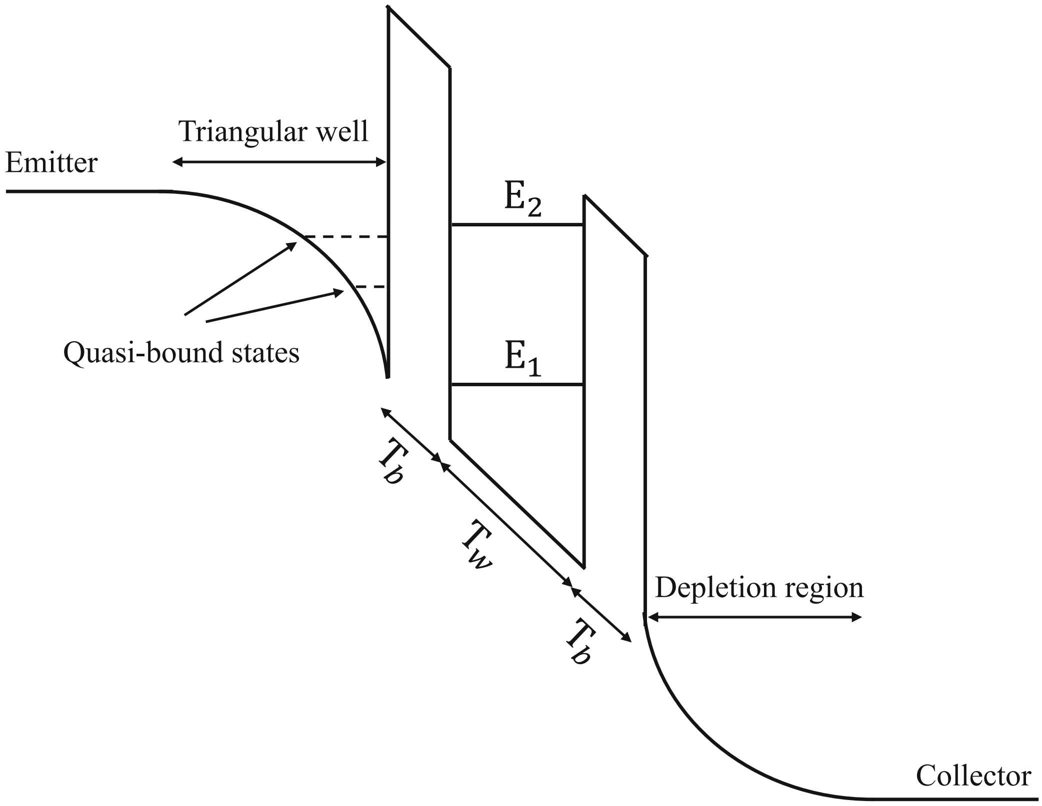

Figure 2.6: Band-diagram of RTD with spacer layer on both sides of barriers.

2.3 Resonant-tunneling-diode oscillators

2.3.1 Early development of RTD oscillators

A resonant tunneling diode oscillator typically consists of a resonator/antenna and an RTD. An RTD is considered as an active device due to its ability to actively compensate for losses of the resonator through its negative differential conductance (NDC). All resonators experience various types of losses, such as ohmic losses and radiation losses. In the most elementary case, the resonator may consist of a resonant LC circuit wherein the losses are symbolized by a resistor with a positive value G, see Fig. 2.7. Subsequently, an RTD is linked to the resonator, wherein a bias voltage is applied within the NDC region. If the NDC region is sufficiently substantial, it will compensate for the losses incurred by the resonator ($|G_{\mathrm{RTD}}| > G$). Subsequently, the resonator will start oscillating by itself,i.e., we have an RTD oscillator. There is an expectation that RTD oscillators can work at high frequencies due to a very fast process of tunneling.

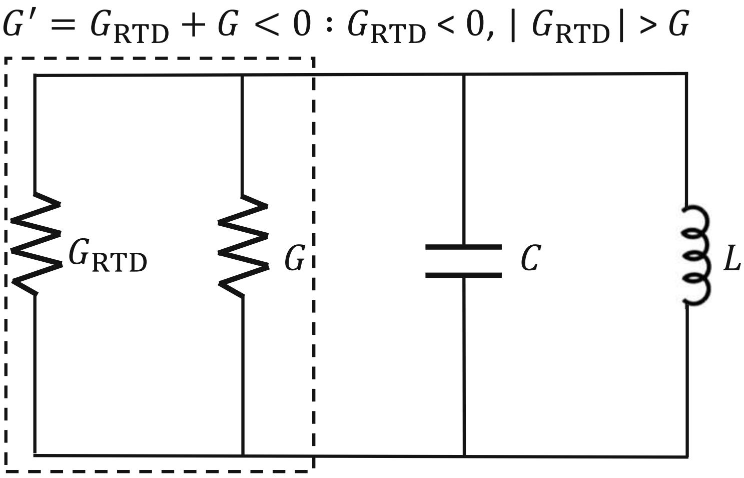

Figure 2.7: An example of a linear RTD oscillator.

The initial development of an RTD oscillator occurred in 1984 at Lincoln Laboratories, where a coaxial cable was utilized for construction, see more detailed in [89]. The RTD was fabricated using a composite material consisting of gallium arsenide (GaAs) and aluminum gallium arsenide ($Al_{0.3}Ga_{0.7}As$). The thicknesses of the barriers and the quantum well were the same of 5 nm. The layers surrounding the barriers were doped at a concentration of $1 \times 10^{18}\mathrm{cm}^{-3}$. The current density of the RTD was 0.06 $\mathrm{mA}/\mu\mathrm{m}^2$, and the peak-to-valley current ratio (PVCR) was 2.8 at 100 K. In order to use the RTD oscillator in practical, the RTD needed to be cooled down to 200 K. The highest oscillation frequency at this temperature was 8.2 GHz with the output power of 5 µW.

The first development of a room temperature RTD oscillator took place in 1985, as mentioned in reference [68]. The difference from the previous design was the doping concentration of the layer surrounding the barriers was decreased from $1 \times 10^{18}\mathrm{cm}^{-3}$ to $5 \times 10^{16}\mathrm{cm}^{-3}$. As a result, the peak current density of this design was decreased (0.016 $\mathrm{mA}/\mu\mathrm{m}^2$). The peak-to-valley current ration (PVCR) was expected to increase; however, it was only reached the value of 1.5 at room temperature due to growing layers technique. The measured oscillation frequency was only 80 MHz, while the output power was around 20 µW. In later work, the RTD barriers were made from pure AlAs, which gives them a higher barrier height and makes them better at stopping the flow of thermionic current. The oscillation frequency of 200 GHz with the output power of 20 µW was reported in 1988 [90], at 420 GHz with the output power of 0.2 µW in 1989 [91], and at 712 GHz with 0.3 µW in 1991 [1].

In the subsequent years of almost 2 decades, there was a lack of notable advancements in the field of RTD oscillators, leading to their perception as an impractical technology.

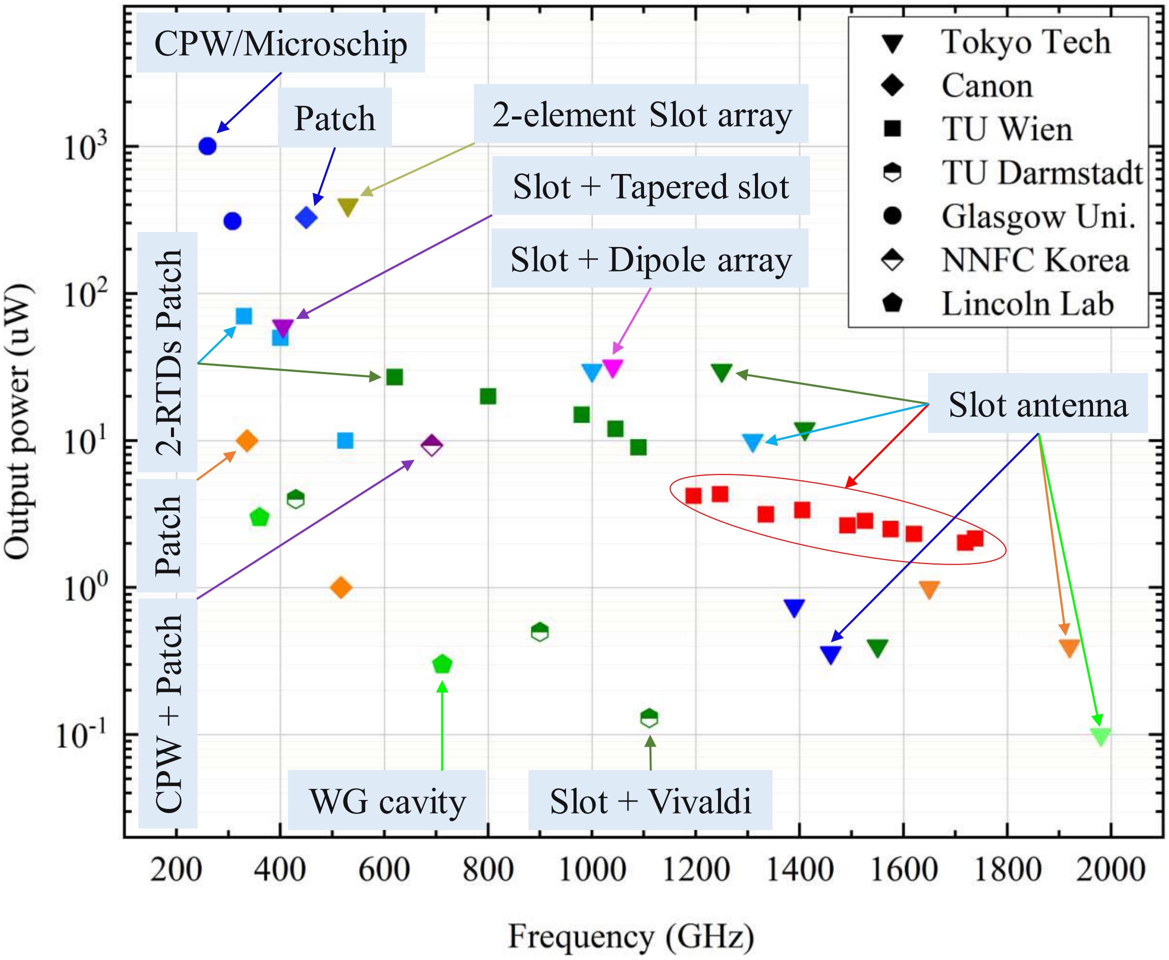

Figure 2.8: Oscillation frequencies and output powers of RTD oscillators operating at the fundamental harmonic. The shapes of the points show the names of the institutions. At one institution, the colors of the points illustrate different types of integrated antennas or different published articles.

Researchers started to put their consideration again on RTD oscillators in 2010 and 2011 when RTD oscillators were demonstrated to work at THz frequency range, see [45] and [5]. Achieving better performance on both oscillation frequency and output power of RTD oscillators is still questionable and needs to be further improved.

2.3.2 Different types of RTD oscillators

Oscillators based on RTDs with negative differential conductance (NDC) have been studied, investigated, and demonstrated for long time already [92]. Researchers proposed and demonstrated lots of different types of RTD oscillators working in the sub-THz and THz frequency range. The initial stages of development commenced by employing coaxial resonators oper-

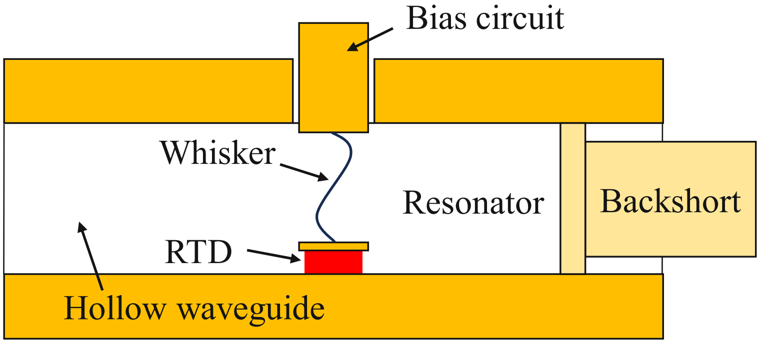

Figure 2.9: A hollow-waveguide oscillator with the highest oscillation frequency of ≈ 0.7 THz [1].

ating at frequencies of around 8.2 GHz as mentioned above in [89]. In this setup, a resonant tunneling diode (RTD) was positioned at the base of a cylindrical cavity and connected using a needle. Additionally, a backshort was placed at a certain distance within the cavity, passing through the center of the cylinder.

Figure 2.8 summarizes the oscillation frequencies with the output powers of different types of RTD oscillators from some institutions. For more details, see tables 2.1 and 2.2.

Hollow-waveguide RTD oscillators

Hollow-waveguide resonators were proposed in order to achieve high oscillation frequencies. These resonators are comprised of a hollow waveguide segment that includes a movable backshort at one end and a mount for an RTD with a whisker contact at the other end, as illustrated in Figure 2.9. The utilization of the movable backshort serves the purpose of adjusting the resonance frequency and confirming the proper functioning of the oscillator at its fundamental frequency. Managing such resonators can be a complex task, and that is why they are currently not in practical of use.

The modification of the materials used in RTD technology has progressed further in the direction of achieving higher frequencies. The substitution of GaAs layers with InAs and the replacement of the barrier material AlAs with AlSb led to the development of a resonant tunneling diode (RTD) that exhibited oscillations at a frequency of 712 GHz. The output power of this RTD oscillator was measured to be 0.3 µW, as reported in reference [1]. The electron mobility in InAs is approximately five times greater than in GaAs. The staggered band alignment between InAs and AlSb results in an increased transmission coefficient compared to GaAs RTD. The utilization of these materials resulted in an increased operational speed of the RTD, thereby enabling the attainment of a higher oscillation frequency.

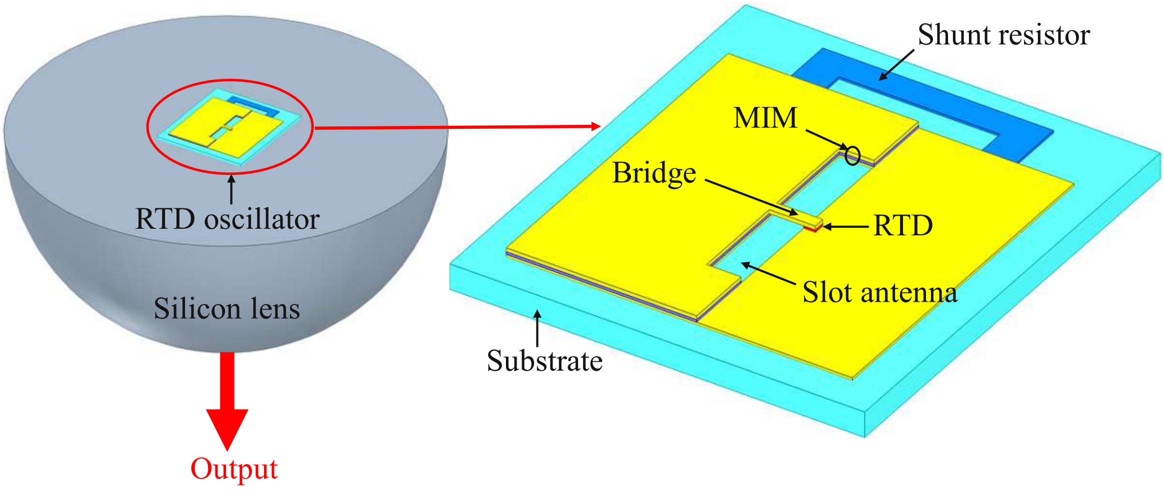

Figure 2.10: On-chip slot-antenna RTD oscillator.

On-chip slot-antenna RTD oscillators

In 1997, the proposal for on-chip slot-antenna RTD oscillators was first introduced [12]. Among other types of RTD oscillators, the slot antenna is considered as a simple resonant antenna, and it can act as an antenna to radiate output power, as well as a resonator. A schematic of a general slot-antenna RTD oscillator is shown in Fig. 2.10. The slot antenna is formed by a rectangular hole in the lower electrode metallization layer and by removing the conducting doped semiconductor layers in the hole. An RTD is positioned on one side of the slot, and an air bridge connects it to the upper electrode of a large metal-insulator-metal (MIM) capacitor on the other side of the slot. The upper and lower electrodes form two contacts to the RTD to supply its DC bias. Additionally, a shunt resistor (e.g., made of indium-tin-oxide (ITO)) is fabricated between the upper and lower electrodes parallel to the RTD to suppress parasitic RTD oscillations at low frequencies. Typically, these oscillators are manufactured on semiconductor substrates possessing a substantial dielectric constant, resulting in the predominant emission of radiation into the substrate. In order to facilitate the emission of radiation and achieve collimation, the chips are affixed onto hemispherical Si lenses.

One of the main features that makes slot-antenna RTD oscillators become a good candidate for high oscillation frequencies range is due to its dimensions. The dimensions of the slot antenna could be reduced to around 10 µm that suits for THz waves, see [9] and [93]. However, decreasing in slot antenna sizes also leads to a decrease in the radiated power of the oscillators. As a results, any optimization of slot-antenna RTD oscillators needs to consider both cases of frequency gain and output power.

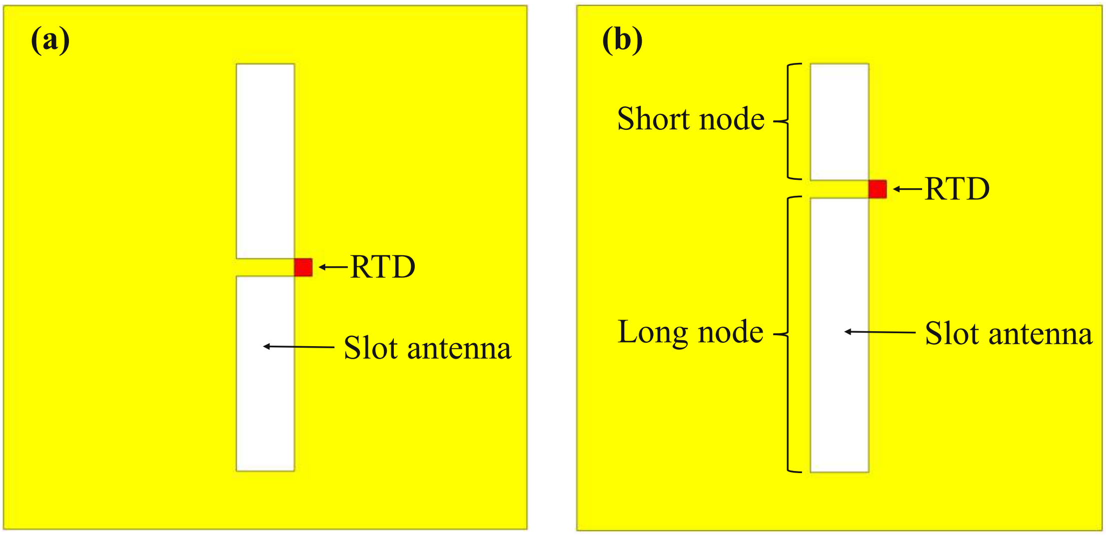

Figure 2.11: Symmetrical (a) and asymmetrical (b) slot-antenna RTD oscillator.

For the optimization of oscillation frequencies, the slot-antenna RTD oscillators have been modified in different ways. The length of the slot-antenna was chosen as the first parameter for this purpose. In reference [94], the length of the slot antenna was reduced from 20 µm to 16 µm. This modification led to an oscillation frequency of 1.55 THz and an output power of 15 µW. Reducing the conduction losses of the slot antennas is another effective way to increase the oscillation frequencies of the oscillators. In the subsequent study conducted at Tokyo Tech [95], a lossy conductive InGaAs layer located beneath the bridge connecting the RTD was selectively removed through etching, while simultaneously increasing the width of the bridge. The implementation of this modification resulted in a decrease in the losses of the slot antenna, thereby enabling the oscillator to achieve oscillation at a fundamental frequency of 1.92 THz, accompanied by an output power of 0.4 µW. In this study, the length of the antenna was 12 µm, the RTD had the peak current density of 50 mA/µm^2, and the peak-to-valley current ratio (PVCR) was measured to be 1.7. In the same group at Tokyo Tech, a slot-antenna RTD oscillator operating at a frequency of 1.98 THz was successfully fabricated [9]. The thickness of the metal constituting the slot antenna was increased from approximately 100 nm to 2 µm that led to a decrease in the conduction loss of the slot antenna. The length of the antenna was 9 µm. The RTD integrated with this slot-antenna has the barrier thickness of 0.9 nm. The peak current density of the RTD was measured to be 31 mA/µm^2, while the peak-to-valley current ratio (PVCR) was $\approx$ 1.81. The measured output power was $\approx$ 0.1 µW.

An "island" design of on-chip slot-antenna RTD oscillators was also proposed, see [93]. This is a part from my thesis, which will be describe in more detailed in the Chapter 5. In this design, the contact n++ layer is removed everywhere except for a small island under the RTD. At frequencies around 2 THz, this design leads to a significant reduction (by a factor of ≈ 2) of the total ohmic losses at the conducting surfaces of the slot antenna. With this design, we achieve the highest radiated power for RTD oscillators in the frequency range 1.6-1.74 THz with around 2.2 µW at the fundamental frequency of 1.74 THz.

As mentioned above, the length of the slot-antenna in THz oscillators is in the range of around 10 to several tens µm and is small compared to the wavelength of the radiated waves [2–5, 9, 45, 95–98]. The radiation efficiency of miniature slot antennas is diminished, thereby imposing constraints on the emitted power of the oscillators. In order to address the issue, the concept of a conventional (symmetrical) slot-antenna was modified to an unconventional design known as an asymmetrical slot antenna RTD oscillator, see Figure 2.11. This involves positioning the RTD in proximity to one end of the slot, where the shorter end functions as a resonator to determine the resonance frequency. Meanwhile, the longer end of the slot serves as an effective radiator. The methodology enables the amplification of the oscillators' output power, resulting in a notable achievement of approximately 400 µW at approximately 550 GHz [10].

The output power of the slot-antenna RTD oscillators could be also increased by integrating such oscillators in an array. By combining a small number of RTD oscillators in the array, the oscillation frequencies of these oscillators can be locked mutually, and their output power were combined coherently. This approach of slot-antenna RTD oscillators was first presented in 1997 [12]; and later on, two-element slot-antenna arrays were demonstrated to work at the fundamental oscillation frequencies of 770 GHz and 810 GHz with the output powers of 270 µW and 180 µW respectively, see [10]. In 2023, the highest output power of 770 µW at $\approx$ 530 GHz was achieved also with 2-element array of slot-antenna RTD oscillators. In this work, asymmetrical slot antennas with the length of 130 µm and an offset of 48 µm were introduced [11]. The peak current density of the RTD was 31 mA/µm^2, and the peak-to-valley current ratio (PVCR) was around 2.5. Achieving mutual locking of a bigger number of oscillators is challenging due to the inherent difficulty in managing the variations of parameters among neighboring oscillators, which arise from technological imperfections.

All types of slot-antenna RTD oscillators mentioned above always include MIM (metal-insulator-metal) layer as a part of the design. However, an another modification of slot-

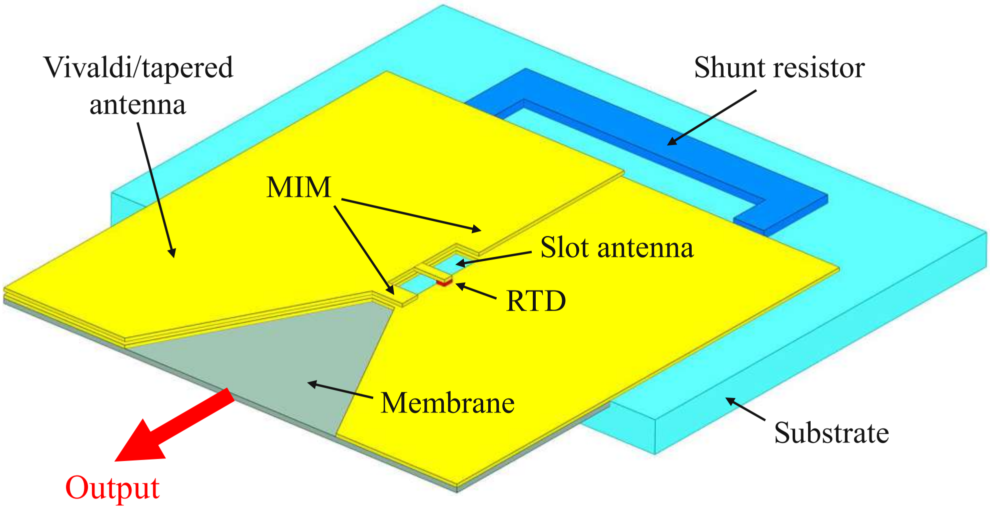

Figure 2.12: A slot-antenna RTD oscillator with a Vivaldi/tapered antenna. The slot antenna acts as a resonator of the RTD, while the Vivaldi/tapered antenna behaves as a radiator. The picture illustrates the Vivaldi antenna positioning on a silicon membrane. The tapered slot antenna is on a patterned semiconductor substrate instead of a membrane.

antenna RTD oscillators without MIM capacitor was successfully fabricated in 2020 [99]. The fundamental oscillation frequency of $\sim$ 600 GHz with $\sim$ 10 µW were achieved.

Membrane RTD oscillators

Another variation of a conventional slot-antenna resonator is the membrane RTD oscillator, which involves the fabrication of a slot antenna RTD resonator on a thin dielectric membrane. Typically, these resonators are additionally integrated with a planar broad-band (Vivaldi) antenna in order to enhance the radiation efficiency of the oscillator, see Figure 2.12. An oscillation frequency of $\sim$ 400 GHz was achieved this type of RTD oscillators, see [100]. The oscillator is this case is situated on a thinned InP substrate with a thickness of approximately 20 µm.

In 2011, the group at the university of Darmstadt reported the operation of an RTD oscillator at a frequency of 1.1 THz. In this study, the resonator utilized a slot-antenna configuration, while a Vivaldi antenna served as the radiator, see [5]. The antenna was positioned on a silicon membrane. The coupling between the resonator and radiator was achieved through the leakage that occurred via the metal-insulator-metal (MIM) structure, see Figure 2.12 for more detailed. Such type of oscillators does not radiate downwards to the substrate, therefore the utilization of a silicon lens is not necessary for the operation of the oscillator. The RTD in this study has the peak current density of $\sim$ 14 mA/µm^2, and the

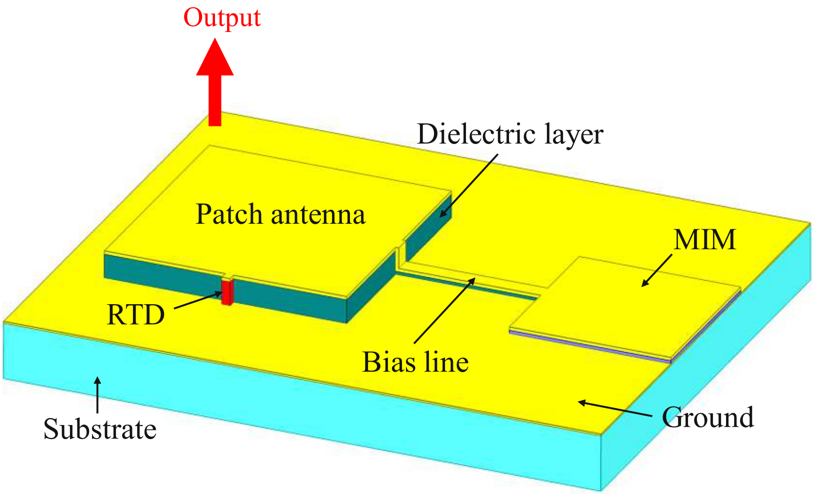

Figure 2.13: A principal sketch of a patch antenna RTD oscillator.

peak-to-valley current ratio (PVCR) of ~ 3.5. The power output of the oscillator reached a maximum of 0.1 µW at the highest achieved oscillation frequency. The RTD layers was grown using a combination of InGaAs/AlAs materials. The thickness of the barriers is 1.2 nm, and the quantum well (QW) structure consisted of a composite material configuration, in which an InAs mini-well with a thickness of 1.2 nm was positioned between $In_{0.53}Ga_{0.47}As$ layers, each with a thickness of 1.2 nm. The dimensions of these oscillators are relatively small, measuring approximately 500×500 µm^2.

Patch antenna RTD oscillators

The concept of combining an RTD with a patch antenna as a resonator/radiator, as shown in Figure 2.13, has been put in research for quite long time. Initially, the utilization of the patch antenna was employed to enhance the coupling of the external radiation's integration into an RTD, see [101]. One of the main advantages of this type of oscillators is that it does not require a silicon lens under the substrate as the direction of the radiation waves is upwards. Consequently, the dimensions of the oscillators can be relatively compact. Later on, the patch antenna RTD oscillator was developed by Canon, see [102]. In this study, the RTD was placed directly between the ground electrode and the patch antenna electrode. The RTD has the peak current density of 2.8 mA/µm^2, and the peak-to-valley current ratio of around 3. A maximum oscillation frequency of approximately 500 GHz with an output power of 1 µW were achieved with the oscillator.

By integrating 2 RTDs with a patch antenna, a group at TU Wien successfully fabricated RTD oscillators with relatively high output power. Output powers of 70 µW and 10 µW were

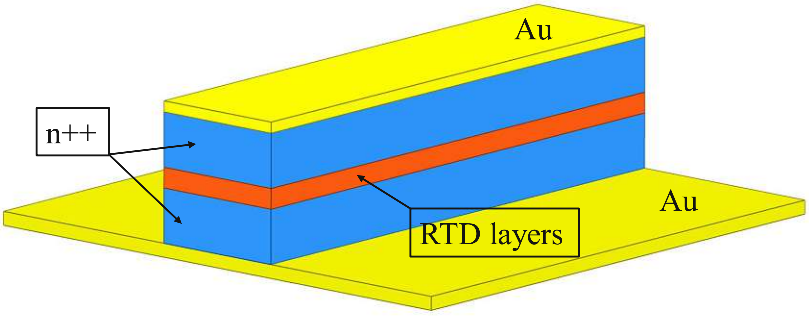

Figure 2.14: A sketch of a travelling-wave microchip RTD oscillator, it is expected to operate at THz frequencies [103].

achieved at fundamental oscillation frequencies of 330 GHz and 525 GHz, relatively, see [98]. The peak current density of the RTD in this case is ∼5.8 mA/µm^2, and the peak-to-valley current ratio is around 8. In the next year [2], a highest oscillation frequency of 1.1 THz with 9 µW output power were recorded with double-RTD patch-antenna oscillators by the same group. The improved parameters are because of a dramatic decrease in the parasitic inductance of the patch antenna by implementation a conical vias which connects the RTD to the patch-antenna electrode, and due to the use of a thinner barrier RTD. The thickness of the RTD barrier in this study is 1.0 nm which results on the peak current density of ∼23.8 mA/µm^2, and the peak-to-valley current ratio of around 3.7.

In accordance with this principle, Canon undertook the optimization of the oscillator, as described in reference [6], through the implementation of impedance matching between the patch antenna and the RTD. The process of impedance matching involved relocating the double-RTD pair from the periphery of the patch towards its central region. The oscillator exhibited an oscillation frequency of 450 GHz with an output power of 320 µW. In this design configuration, a total of 36 double-RTD patch antennas were configured to ab arrangement of oscillators. The output power of the array exceeded 10 mW.

Travelling-wave microstrip RTD oscillator

The idea of using NDC active layers in traveling-wave oscillators has been mentioned earlier in [92], and an in-depth theoretical analysis of travelling-wave microstrip RTD oscillators was presented in [103]. Such type of RTD oscillators should work at room temperature, and could operate at frequencie range of 1 to 2 THz, and maybe higher. Microstrips have a bigger active volume than lumped-element oscillators, hence they should be able to generate more THz output power. Microstrip RTD oscillators can be considered in a different way by replacing the entire cascade with their single period — an RTD — making them similar to

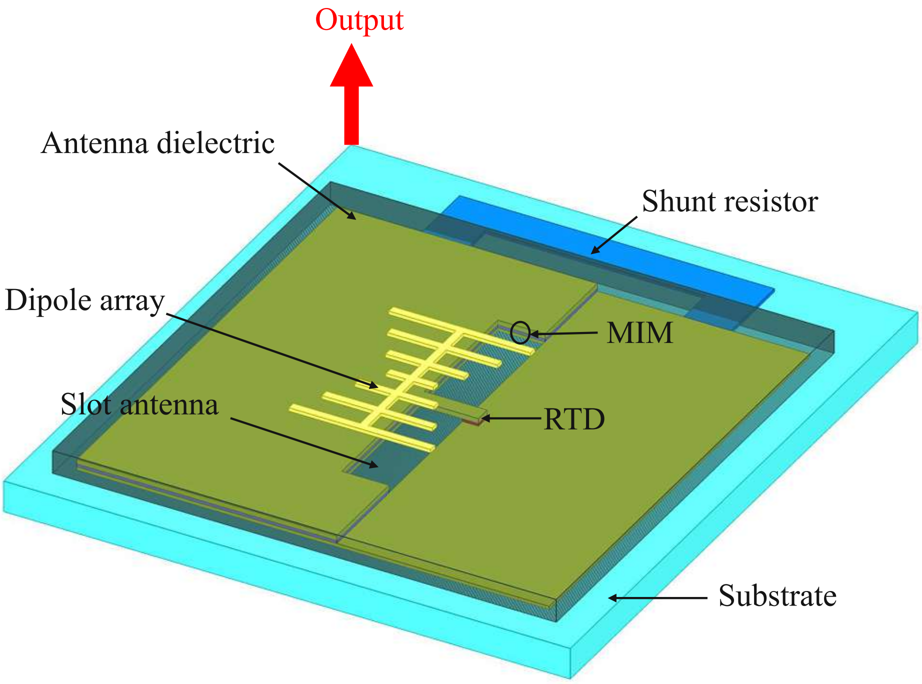

Figure 2.15: An RTD oscillator with a dipole array (Yagi-Uda) as the secondary radiator.

THz QCLs with metal-metal waveguide. Microstrip RTD oscillators, unlike THz QCLs, can operate at room temperature without the need for cryogenic cooling.

Harmonic RTD oscillator

Another category of RTD oscillators is known as harmonic oscillators. A second harmonic of an RTD oscillator was reported with an oscillation frequency of $\sim$ 87 GHz, see [104]. The initial publication regarding THz emission from RTD oscillators was observed at the third harmonic frequency, as documented in reference [105]. In this study, the fundamental and third harmonic frequencies were 342 GHz and 1.02 THz, respectively. The length of the slot antenna is 50 µm. The output power at the fundamental frequency was 23 µW, and the third harmonic has $\sim$ 2.6 % of the fundamental output power. In triple-push RTD oscillators, it was observed that the emission of the highest frequency harmonic achieved at 1.52 THz, specifically corresponding to the third harmonic with the power output of $\sim$ 1.9 µW, see [106].

RTD oscillators with a secondary radiator

One of the main features of RTD oscillators that makes them to be a good candidate for sub-THz and THz applications is due to their compact sizes. The total dimensions of the RTD oscillators which require a silicon lens are quite large ($\approx$ 5mm), while the size of the RTD oscillators themselves is only several hundreds µm. As a result, designing RTD oscillators without the use of the silicon lens is advantageous.

One potential method for directing the radiated waves upwards from the substrate involves employing a supplementary radiator that is coupled to the slot antenna RTD oscillator. In this type of oscillators, the primary function of the slot antenna is to serve as the resonator, while the secondary antenna assumes the role of the radiator.

The combining of a slot antenna with a patch antenna was first presented in [94]. The patch antenna was positioned on a BCB polymer. An oscillation frequency of $\sim$ 1 THz with an output power of 15 µW was achieved with this oscillator. Later on, a 55 µW output power was received by using an array of three oscillators. As mentioned above, the matching in frequency between a slot antenna and a patch antenna is a crucial point. Consequently, putting more oscillators in an array is a challenging and not really reliable.

In 2019, instead of using a patch antenna for coupling with a slot antenna, an array of dipole antennas was employed in an RTD oscillator, see [7]. The design configuration can be seen in Figure 2.15. The dipole antennas were put on the COC polymer which has lower losses than BCB polymer, and were made of different dipole lengths, which result on a broadband radiation. An oscillation frequency of 1.04 THz with an output power of 21 µW was achieved with this oscillator. Later on, an array of 83 elements of oscillators was put together, and radiated around 730 µW.

The state-of-the-art of different types of RTD oscillators are shown in the tables 2.1 and 2.2. Each reference listed in the tables shows following parameters: the published year and the institution of the article , the type of antenna integrated in the RTD oscillators, the need of using Si lens, the number of RTDs, the oscillation frequency, the DC-to-RF efficiency, and the radiated output power of the RTD oscillators. The parameters of the RTD, such as the peak current density j_p, the peak to valley current ratio PVCR, the current and voltage differences between the peak and the valley points ΔI, ΔV are also shown in the tables.

The state-of-the-art of RTD oscillators in the direction of high output powers are shown in the table 2.1. According to this table, the highest output power of 11.8 mW was achieved at the fundamental oscillation frequency of 0.45 THz on a 36-elements patch array RTD oscillator, see [6]. Table 2.2 illustrates the state-of-the-art of RTD oscillators is the case of high oscillation frequency. The highest fundamental oscillation frequency of 1.98 THz was received with a slot-antenna RTD oscillator, see [9].

References	[10]	[7]	[8]	[107]	[108]
Year	2012	2019	2020	2021	2021
Antenna type	Slot	Slot+Dipole	Microstrip	Ring slot	CPW+Patch
2nd radiator	Si lens	No	No	Si Lens	No
RTDs	2	89	1	2	1
Frequency (THz)	0.62	1	0.26	0.35	0.69
DC-RF eff. (%)	-	-	0.7	NA	0.27
Power (μW)	610	730	1000	30	10
j_p (mA/μm^2)	-	30	3	-	6.61
PVCR (-)	-	2	3	-	1.3
ΔJ (mA/μm^2)	14	-	1.6	-	-
ΔV (V)	0.36	0.3 - 0.4	0.6	-	0.16
Institution	Tok. Tech	Tok. Tech	Glas. Uni.	Osaka Uni.	NNFC

References	[98]	[109]	[57]	[6]	[11]
Year	2021	2021	2022	2022	2023
Antenna type	Patch	SRR	Slot	Patch	Slot
2nd radiator	No	Si lens	Si lens	No	Si lens
RTDs	2	1	1	72	2
Frequency (THz)	0.33	0.9	0.09	0.45	0.53
DC-RF eff. (%)	-	-	5	1	0.22
Power (μW)	70	30	500	11800	770
j_p (mA/μm^2)	5.8	8	5.8	-	12
PVCR (-)	8.9	3.18	8.9	2.5	2.5
ΔJ (mA/μm^2)	4.9	-	4.9	14	-
ΔV (V)	0.48	0.54	0.48	0.55	0.4
Institution	TU Vienna	Tok. Tech	TU Vienna	Canon	Tok. Tech

Table 2.1: State-of-the-art in high-power RTD THz oscillators

References	[5]	[95]	[94]	[96]	[9]
Year	2011	2014	2015	2016	2017
Antenna type	Slot+Vivaldi	Slot	Slot+Patch	Slot	Slot
2nd radiato	No	No	No	Si lens	Si lens
RTDs	1	1	1	1	1
Frequency (THz)	1.1	1.55	1	1.92	1.98
DC-RF eff. (%)	0.004	-	-	0.03	-
Power (μW)	0.1	0.4	15	0.4	-
j_{p} (mA/μm^2)	14	-	35	50	31
PVCR (-)	3.5	-	2	1.7	1.81
ΔJ (mA/μm^2)	10	-	17.5	20.6	13.9
ΔV (V)	0.5	-	-	0.4	0.51
Institution	Darm. Uni.	Tok. Tech	Tok. Tech	Tok. Tech	Tok. Tech

References	[7]	[109]	[108]	[2]	[93]
Year	2019	2021	2021	2022	2023
Antenna type	Slot+Yagi	SRR	CPW+Patch	Patch	Slot
2nd radiato	No	Si lens	No	No	Si lens
RTDs	1	1	1	2	1
Frequency (THz)	1.04	1.22	0.69	1.09	1.74
DC-RF eff. (%)	0.4	-	0.27	0.25	-
Power (μW)	21	7	9.3	9	2
j_{p} (mA/μm^2)	30	8	6.6	23.6	23.6
PVCR (-)	2	3.18	1.3	3.7	3.7
ΔJ (mA/μm^2)	15	-	1.5	17.2	17.2
ΔV (V)	0.34	0.54	0.3	0.33	0.33
Institution	Tok. Tech	Tok. Tech	NNFC	TU Vienna	TU Vienna

Table 2.2: State-of-the-art in high-oscillation-frequency RTD THz oscillators

2.4 Design considerations for RTD oscillators

This discussion will explore the key design considerations that need to be taken into account when developing RTD oscillators:

2.4.1 High oscillation frequencies case

- Increase the magnitude of the NDC region (the ratio $\Delta I/\Delta V$, or the conductance) of the RTDs. It can be done by reducing the thickness of the barriers, optimizing the thickness and the composition of the well.
- Lower the contact resistance of the RTDs and the deposition metal layer, as mentioned in Chapter 2. By increasing the quality of the RTDs contacts as well as carefully doing fabrication steps, a good value of contact resistance can be achieved.
- Decrease the losses of the resonator/radiator.
- High oscillation frequencies can be received on the short slot antenna.

2.4.2 High output power case

In order to achieve high output power, one needs to consider followings:

- Increase the magnitude of ΔI and ΔV of the RTDs as the output power is directly proportional to ΔI and ΔV. Reducing the thermal heating of the RTDs by decreasing the peak voltage V_p is also important factor. It is affected by the configuration of the emitter and the well.
- Increase the radiation conductance of the integrated antennas which is related to the dimensions of the antennas.
- Decrease the parasitic losses of the antennas.
- Introduce multiple RTD oscillators in an array. However, the parameters of these oscillators need to be calculated carefully to satisfy the matching conditions between them.

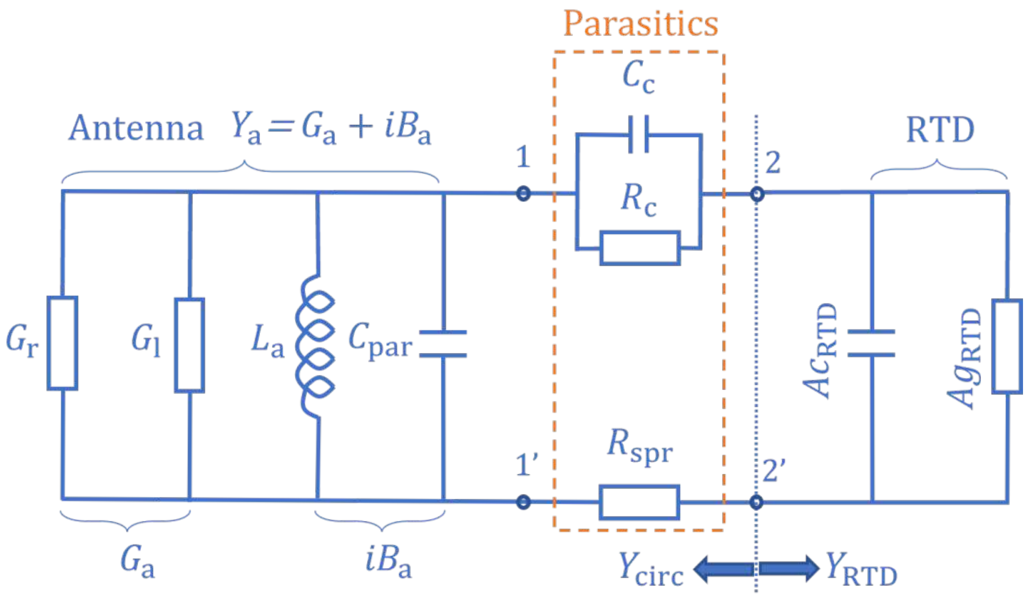

Figure 2.16: AC equivalent circuit of an RTD oscillator.

2.5 Simulation model of RTD oscillators

The solutions of any simulation models of RTD oscillators are oscillation frequencies, output powers, and DC-to-RF efficiency. These parameters are estimated and calculated based on the small-signal analysis and large-signal analysis of RTD oscillators with NDC. The small-signal analysis uses a linear RTD model which is sufficient to determine whether the system can oscillate and the oscillation frequencies. However, the oscillating voltage in the small-signal model has been considered to be infinitely small, therefore the calculation of the output power of RTD oscillators using this model is not correct. The amplitude of the steady-state oscillators is limited by the RTD non-linearity, i.e., we should use a non-linearity RTD model to analyze the output power of the RTD oscillators, and it leads to an analysis of the large-signal of RTD model. The small-signal RTD model and the large-signal RTD model can be found in [4], [110–113].

In this section, we will apply the concept of these two analysis models for our oscillation frequencies and output power estimation of the simulation model.

Figure 2.16 shows an equivalent circuit that was used in the theoretical analysis of the RTD oscillators. Y_a represents the admittance of an antenna, where B_a is the antenna susceptance and G_a is its total conductance, which is equal to the sum of the antenna loss (G_l) and radiation (G_r) conductances. Y_a, G_l, and G_r are simulated with a commercial (ANSYS HFSS) electromagnetic simulator for every given antenna geometry. C_{par} is the parasitic RTD capacitance, which is assumed to be in the range from to 0.35 fF to 1 fF for our oscillators (it depends on the dimensions of the air-bridge from the edges of the slot-antenna (in our cases) to the RTD mesa). R_{spr} is the RTD spreading resistance of its bottom contact calculated for each RTD-mesa area; ρ and c_{c} are the specific (per unit area) contact resistance and capacitance, respectively, of the RTD top contact, which are taken to be equal to 1-3 $\Omega\,\mu\mathrm{m}^2$ and 19 $\mathrm{fF}/\mu\mathrm{m}^2$. A is the RTD-mesa area. g_{RTD} and c_{RTD} are the specific RTD conductance and capacitance, respectively; they are dependent on the frequency (ω) and AC oscillation amplitude (V_{AC}). The oscillation conditions of an oscillator are defined by the equations:

$$\mathrm{Im}(Y_{\mathrm{circ}}) = -A\,\omega\,c_{\mathrm{RTD}}(\omega, V_{\mathrm{AC}}), \tag{2.11}$$

$$\mathrm{Re}(Y_{\mathrm{circ}}) = -A\,g_{\mathrm{RTD}}(\omega, V_{\mathrm{AC}}). \tag{2.12}$$

Solution of the system of Eqs. (2.11) and (2.12) provides a steady-oscillation amplitude V_{AC} and oscillation frequency ω. The output power is then calculated as:

$$P = \frac{1}{2}\left|\frac{Y_{\mathrm{circ}}}{Y_{\mathrm{a}}}\right|^2 G_{\mathrm{r}} V_{\mathrm{AC}}^2. \tag{2.13}$$

To define $g_{\mathrm{RTD}}(\omega, V_{\mathrm{AC}})$ and $c_{\mathrm{RTD}}(\omega, V_{\mathrm{AC}})$, we rely on quasi-static (quasi-DC) and small-signal (SS) dynamic characteristics of an RTD. First, we apply a harmonic AC voltage to the RTD, biased at a given DC bias (V_{DC}): $V(t) = V_{\mathrm{DC}} + V_{\mathrm{AC}}\cos(\omega t)$. Then, we calculate the first harmonic of the DC RTD current density (j_0) divided by V_{AC}, which defines the first-harmonic quasi-DC RTD conductance:

$$g_0^{(1)}(V_{\mathrm{AC}}) = \frac{2}{\pi}\frac{1}{V_{\mathrm{AC}}}\int_0^{\pi} j_0\left(V_{\mathrm{DC}} + V_{\mathrm{AC}}\cos(\xi)\right)\cos(\xi)\,d\xi. \tag{2.14}$$

Then, we use a SS dynamic RTD model [110–112] to take into account the frequency roll-off of the RTD conductance and define $g_{\mathrm{RTD}}(\omega, V_{\mathrm{AC}})$ as

$$g_{\mathrm{RTD}}(\omega, V_{\mathrm{AC}}) = \frac{g_{\mathrm{SS}}(\omega)}{g_0} g_0^{(1)}(V_{\mathrm{AC}}), \tag{2.15}$$

where, $g_{\mathrm{SS}}(\omega)$ and g_0 are the SS (dynamic) and DC RTD conductances, respectively; all parameters are dependent on the DC bias point V_{DC}. $g_{\mathrm{SS}}(\omega)$ is calculated with a SS (linear) charge-relaxation model [110–112]. In such a way, first, Eq. (2.15) gives a correct small-signal value for the RTD dynamic conductance; second, it provides an accurate description of the variation (roll-off) of the RTD conductance with V_{AC} in the quasi-DC case; and, third, it approximately describes this roll-off at higher frequencies.

In a similar fashion, we define $c_{RTD}(\omega, V_{AC})$. It is defined as the amplitude of the first harmonic of the RTD capacitive current (which is $\propto \sin(\omega t)$), divided by ωV_{AC}:

$$c_{RTD}(\omega, V_{AC}) = c^{(1)}(\omega, V_{AC}) = \frac{2}{\pi}\int_0^{\pi} c_{SS}\left(\omega, V_{DC} + V_{AC}\cos(\xi)\right)\sin^2(\xi)\,d\xi. \tag{2.16}$$

where, c_{SS} is a SS RTD capacitance, calculated as

$$c_{SS}\left(\omega, V\right) = c_{ec}(V) - \frac{g_0(V) - g_\infty(V)}{1 + (\omega\,\tau_{resp}(V))^2}\tau_{resp}(V) \tag{2.17}$$

according to [110–112], where c_{ec} is the geometrical RTD emitter-collector capacitance, g_∞ is the high-frequency RTD conductance, and τ_{resp} is the RTD charge-relaxation time constant. Eq. (2.16) is converging to c_{SS}, when $V_{AC} \to 0$. On the other hand, it provides also an accurate capacitance value for large V_{AC} in the quasi-static limit ($\omega \to 0$). Large-signal high-frequency values provided by Eq. (2.16) are approximate. To go beyond the above simplified approximations for $g_{RTD}(\omega, V_{AC})$ and $c_{RTD}(\omega, V_{AC})$, one needs to use an accurate large-signal model for RTD dynamics [113], which goes beyond the scope of this thesis.

2.6 Conclusions

In this chapter, we have described the operational principle of RTDs. We have shown the structural parameters of RTDs, such as the growth material systems, the barrier thickness, the spacer thickness, and the QW thickness which affect on the performance of the RTDs (the peak current density, or the peak to valley current ration).

Next, we have presented the early development of the RTD oscillators, and some different types of RTD oscillators, such as patch antenna RTD oscillators, slot antenna RTD oscilltors, travelling-wave microchip RTD oscillators, etc...Among these types of RTD oscillators, the symmetrical slot-antenna RTD oscillators have been chosen for the thesis. In addition, we describe some key factors for the consideration when designing RTD oscillators, and describe the simulation model of the RTD oscillators.

Chapter 3

Proposal of structures, fabrication process, and frequency limitation of symmetrical-slot-antenna RTD oscillators

3.1 Introduction

Among different types of RTD oscillators (slot- and patch-antenna, membrane, composite, waveguide-based,etc.), the slot-antenna RTD oscillators were chosen for the performance in the terms of high operating frequencies and simple designs. On-chip-slot-antenna RTD oscillators are also the most simple and the most studied type of RTD oscillators. This chapter proposes and explains the device structure as well as the fabrication process of a typical slot-antenna RTD oscillator. Next, we mention some factors on design considerations for RTD oscillators, and show the analysis for simulation model of RTD oscillators. The discussion of the limitation of the oscillation frequencies of RTD oscillators will close this chapter.

3.2 Structure design of slot-antenna RTD oscillators

The design of a slot-antenna RTD oscillator we investigate in this work is sketched in Fig. 3.1. That is a rather common design of RTD oscillators in the sub-THz and THz frequency range [105]. The slot antenna is formed by a rectangular hole in the lower-electrode metallization layer and by removing the conducting doped semiconductor layers in the hole. The slot acts as a resonator by forming a standing wave of an electromagnetic field, and it also performs the function of an antenna by radiating output power at the same time. An RTD is positioned on

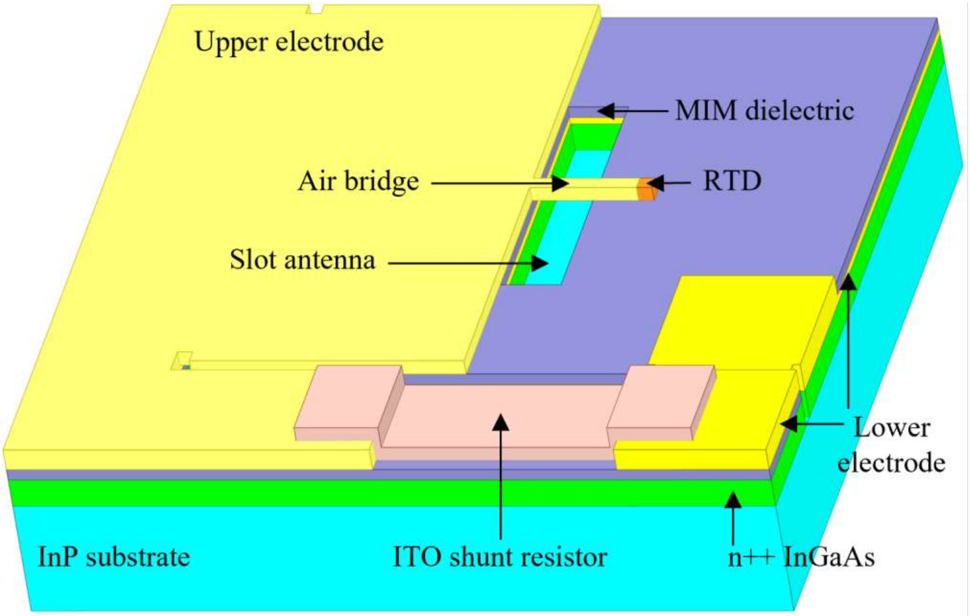

Figure 3.1: Schematic of a slot-antenna RTD oscillator.

one side of the slot and it is connected by an air bridge to the upper-electrode (UE) of a large metal-insulator-metal (MIM) capacitor on the other side of the slot to reduce the conduction loss of the antenna and parasitic capacitance near RTD mesa. The upper and lower electrodes (UE and LE) form two contacts to the RTD to supply its DC bias. Additionally, a shunt resistor (e.g. made of indium-tin-oxide (ITO)) is fabricated between the upper and lower electrodes in parallel to the RTD to suppress parasitic RTD oscillations at low frequencies.

3.3 Fabrication process

Our fabrication process is similar to the one described in the literature [114]. The fabrication process is based on optical lithography, except for one or two steps which were done by electron-beam lithography (EBL). The whole general processes from preparing samples to the final step of the fabrication procedure will be discussed clearly in this section. However, there will be some small changes in the recipe for each design of RTD oscillators investigated later in Chapter 4 and Chapter 5.

3.3.1 RTD wafer preparation

The RTD wafer is cleaned with DI water, acetone, and isopropanol (IPA) using ultrasonic cleaning in 5 minutes for each cleaning solution. The sample is then blown with N_2 gas to

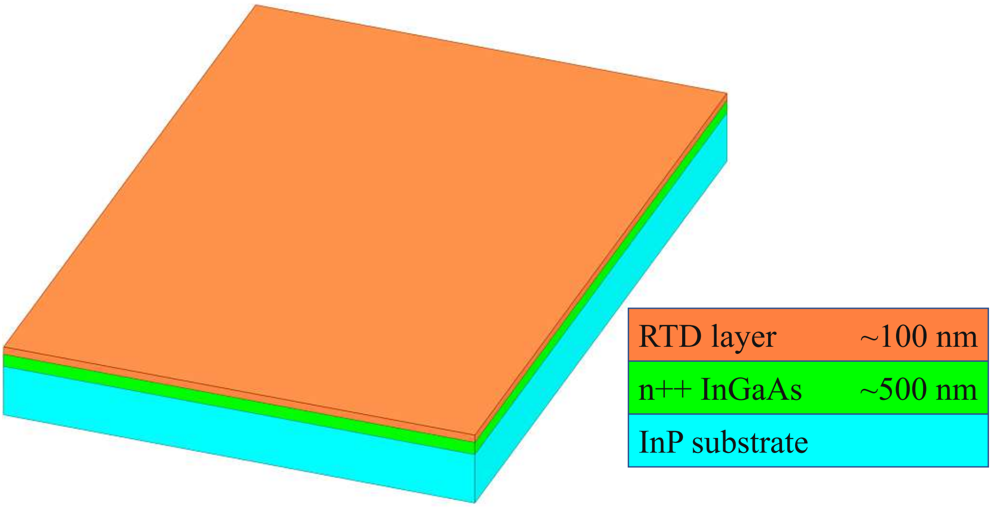

Figure 3.2: A stack layout of an RTD sample.

be dry, and then is put on the hot plate at 120°C to avoid remaining water and enhance the adhesion for coating photoresist on the sample.

3.3.2 Top RTD-mesa electrodes fabrication

After cleaning step, the RTD sample is now ready for the next processes.

The sample is spin-coated with two layers of photoresists. The bottom photoresist layer is LOR3A, and the top one is AZ5214E (for electron-beam lithography, PMGI and PMMA were used as the bottom and the top photoresists). The purpose of using double layers of photoresists is to create an undercut of the bottom resist layer (LOR3A as it is not sensitive with lithography processes) that makes the lift-off step much easier. Also, LOR3A and AZ5214E are tolerant to acid, which is used for surface cleaning before the contact metal deposition. As the following: the optical lithography (or EBL) is first used to pattern the RTD mesa, then surface cleaning (dry etching with O_2 etching at 100 W and 10 sccm for 30 seconds, and wet etching with HCl 10 % for 1 minute at room temperature). An alloy of Ti/Pd/Au (20/20/150 nm) is then deposited on the sample using evaporation machines. The sample is put in the hot DMSO solution to lift-off the photoresists.

3.3.3 RTD mesa formation

For formation of RTD mesa, the piranha solution ($S_2SO_4 : H_2O_2 : H_2O = 1 : 1 : 40$) is used for the wet etching process at 0°C. The etching depth depends on the RTD layer thickness

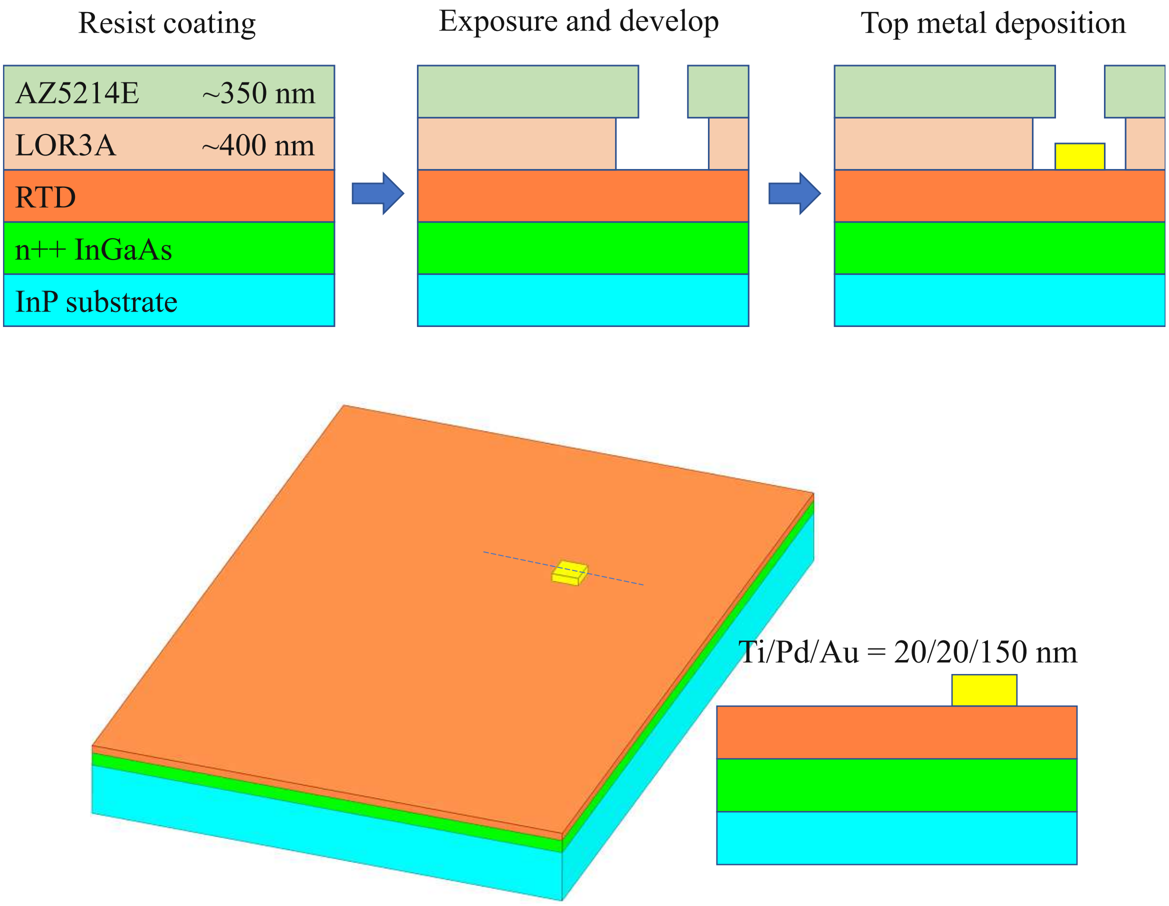

Figure 3.3: Top metal deposition.

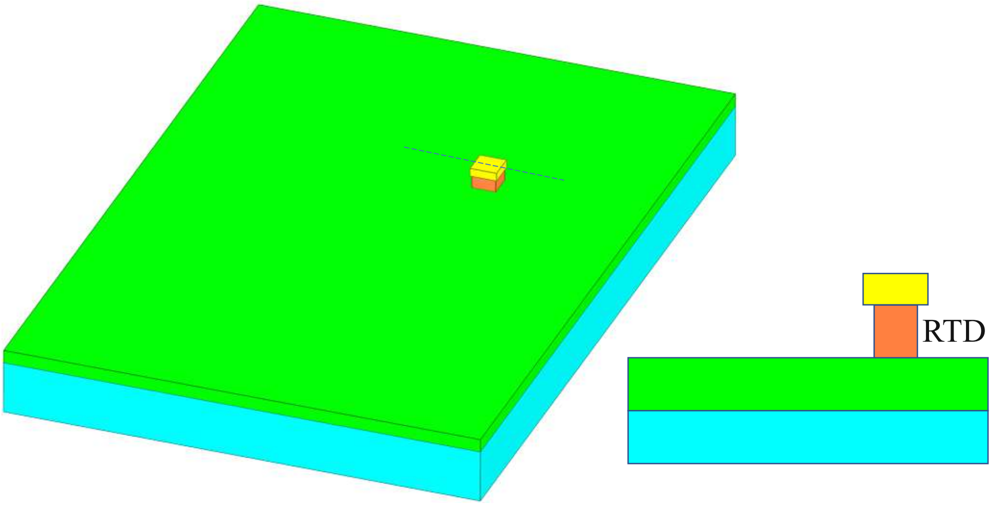

Figure 3.4: RTD mesa formation.

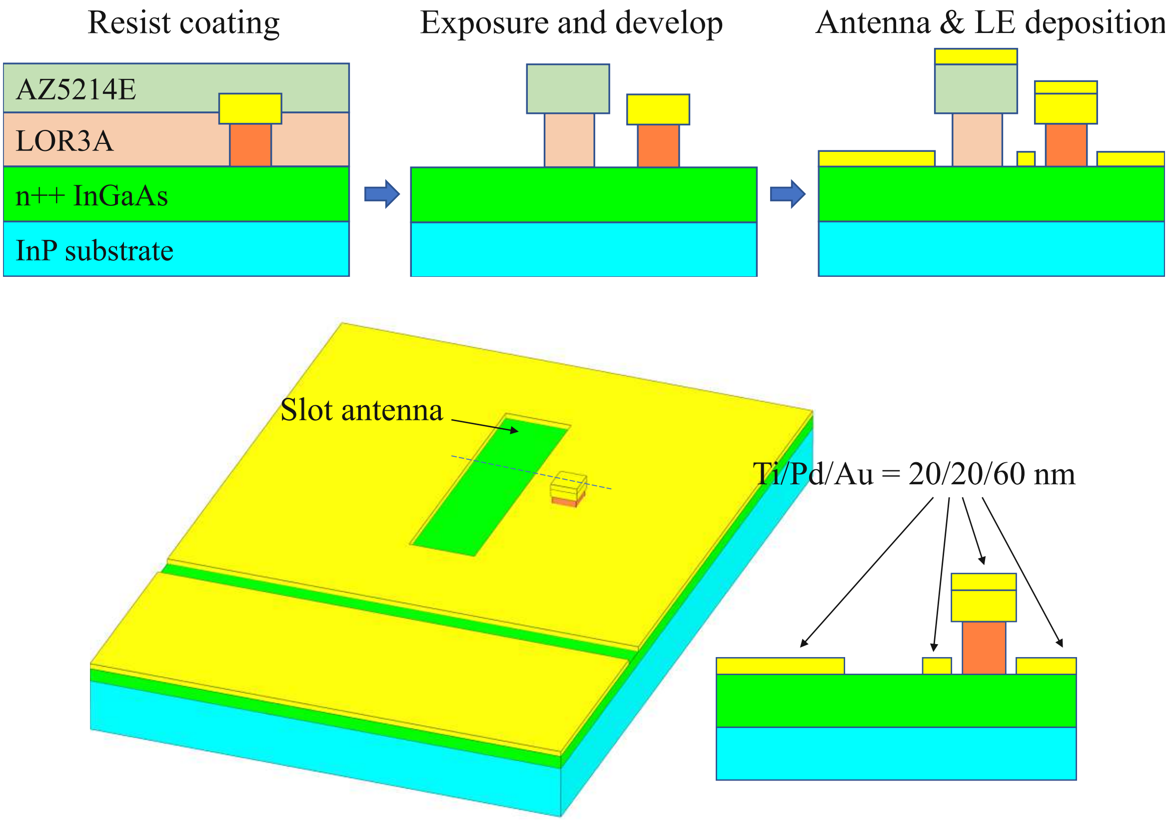

Figure 3.5: Slot-antenna & LE formation.

which is different for every RTD wafer structure. In our case, ∼ 150 nm InGaAs etching is sufficient.

3.3.4 Slot-antenna and lower electrode evaporation

At this step, two layers of photoresists (LOR3A and AZ5214E) are also used for the spin-coating process. The mask of the slot-antenna and lower electrode is then applied for patterning on the sample, following by developing in the developer MIF726, then surface cleaning (dry etching with O_2 etching at 100 W and 10 sccm for 30 seconds). A combination of Ti/Pd/Au (20/20/60 nm) is then deposited on the sample using evaporation machines. The sample is put in the hot (90°C) DMSO solution to lift-off the photoresists.

Formation of slot-antenna

The next step is to etch away the n++ InGaAs layer inside the slot-antenna. In order to avoid the short between electrodes, an isolation trench is also etched together in this step.

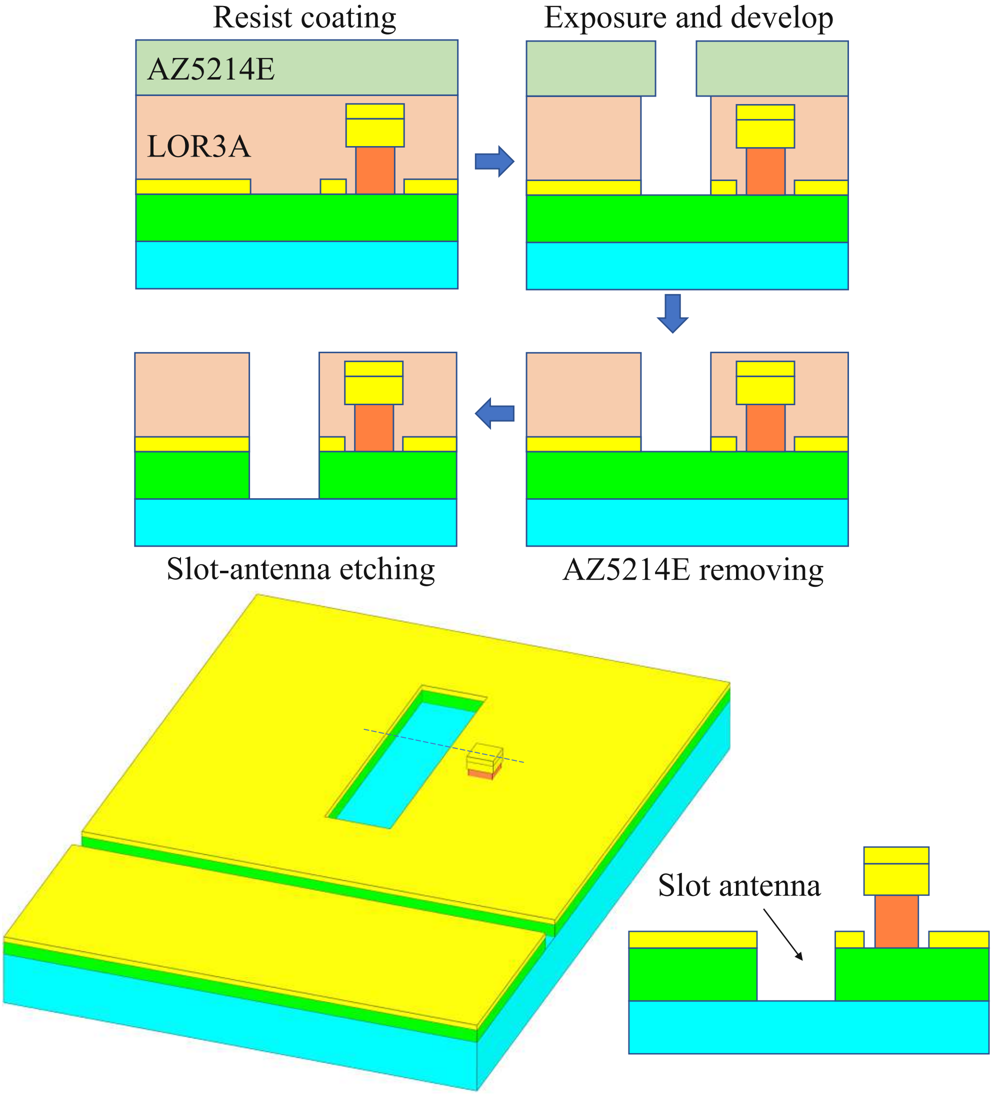

Figure 3.6: Slot-antenna & isolation trench formation.

LOR3A resist is used as a mask for the etching process. All parts of the sample, except the slot-antenna area and the trench, are covered by LOR3A (as always, firstly two layers of resists LOR3A and AZ5214E are used for patterning the mask, then AZ5214E is removed away using acetone solution as LOR3A is not dissolved in acetone). The sample is then baked in the hot plate at 200°C for 5 minutes to semi-cross-link resist LOR3A. Using reactive ion etching (RIE, RF: 140 W, ICP: 250 W, Cl_2: 4 sccm, Ar: 18 sccm) at 175°C for $\sim$ 50 seconds to etch away n++ InGaAs layer inside the slot-antenna and the trench. At the last step, the LOR3A mask is removed using DMSO solution, following by O_2 cleaning in the RIE.

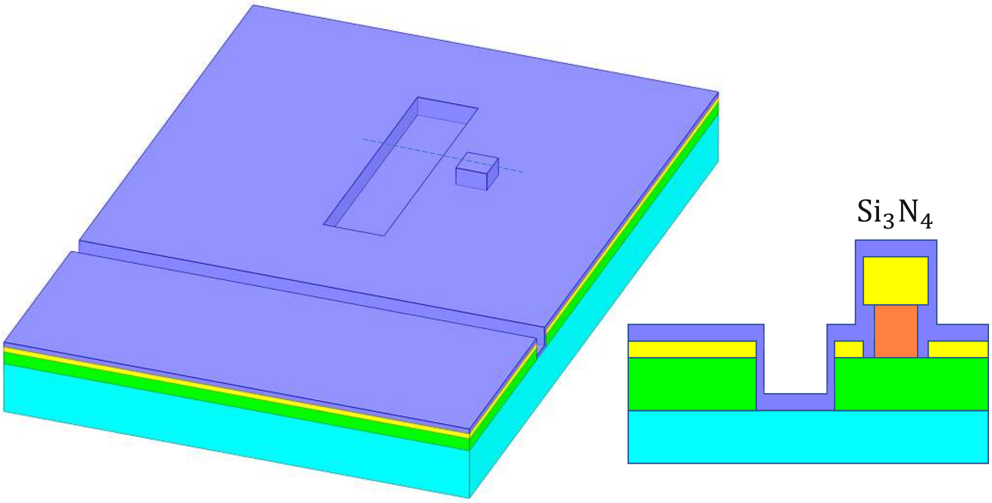

Figure 3.7: Passivation 150 nm Si_3N_4

3.3.5 Isolation layer (Si_3N_4) deposition

An isolation layer Si_3N_4 of $\sim$ 150 nm is deposited on the entire sample using plasma-enhanced chemical vapor deposition (PECVD) machine.

Opening Si_3N_4 for RTD mesa and contact pads

The opening process of Si_3N_4 areas for the RTD mesa and contact pads starts with coating $\sim$ 1.5 µm AZ5214E resist which is used as a mask for the reactive ion etching (RIE). CHF_3 gas at 20°C has been using for this etching process. The AZ5214E resist is chosen in this step because the etching temperature is only 20°C, while the baking temperature of AZ5214E is 100°C. It takes about 3 minutes to etch away Si_3N_4 on RTD mesa and contact pads. The passivation AZ5124E resist is removed after etching process by hot (90°C) DMSO solution, following by O_2 surface cleaning in RIE machine. The sample is ready for next steps.

3.3.6 Supporting layer for the bridges

To avoid cracks at the edges of the slot-antenna and the isolation trench (as the depth of the slot-antenna is $\sim$ 600 nm), a supporting layer is needed to build the bridges over the slot-antenna and the isolation trench. The height of the supporting layer should be relatively comparable with the depth of the slot-antenna. AZ5214E cross-linked resist has been chosen for this purpose. Around 800 nm of AZ5214E is coated on the sample. after patterning and developing, the sample is put on the hot plate at 180°C for about 10 minutes to cross-link the

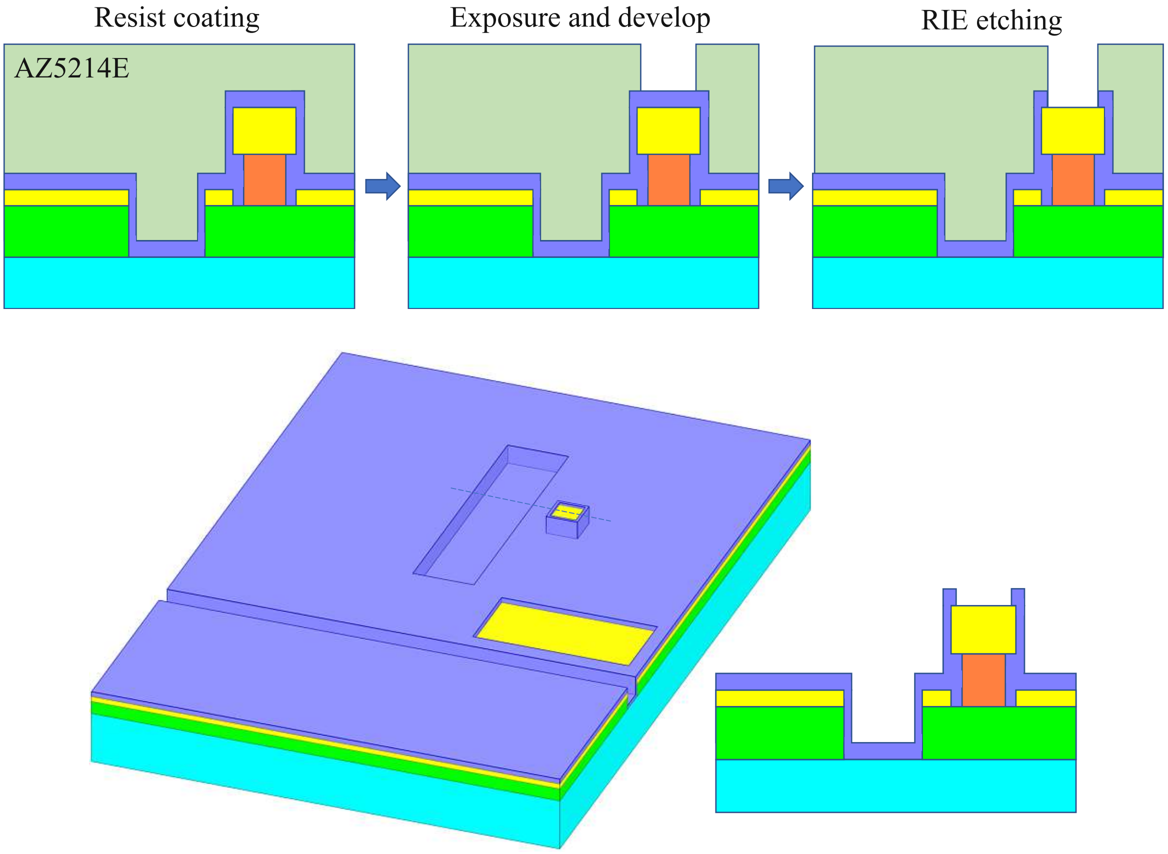

Figure 3.8: Opening Si_3N_4

resist and to make the edges of the supporting layers smoother by re-flowing-process during baking sample.

3.3.7 Air bridge and MIM fabrication

As previous fabrication steps, the lithography process is started with spin-coating two layers of resists (LOR3A and AZ5214E), following by patterning and developing. Next, surface cleaning is done by O_2 etching in RIE machine. A composition of Ti/Au = 20/280 nm is deposited on the sample using evaporation machine. The resist mask is then removed in the DMSO solution.

3.3.8 Stabilized shunt resistor deposition

As a final step, a shunt resistor was deposited outside the slot-antenna area to suppress low-frequency instability of the RTD oscillators. In general cases, Indium tin oxide (ITO) is

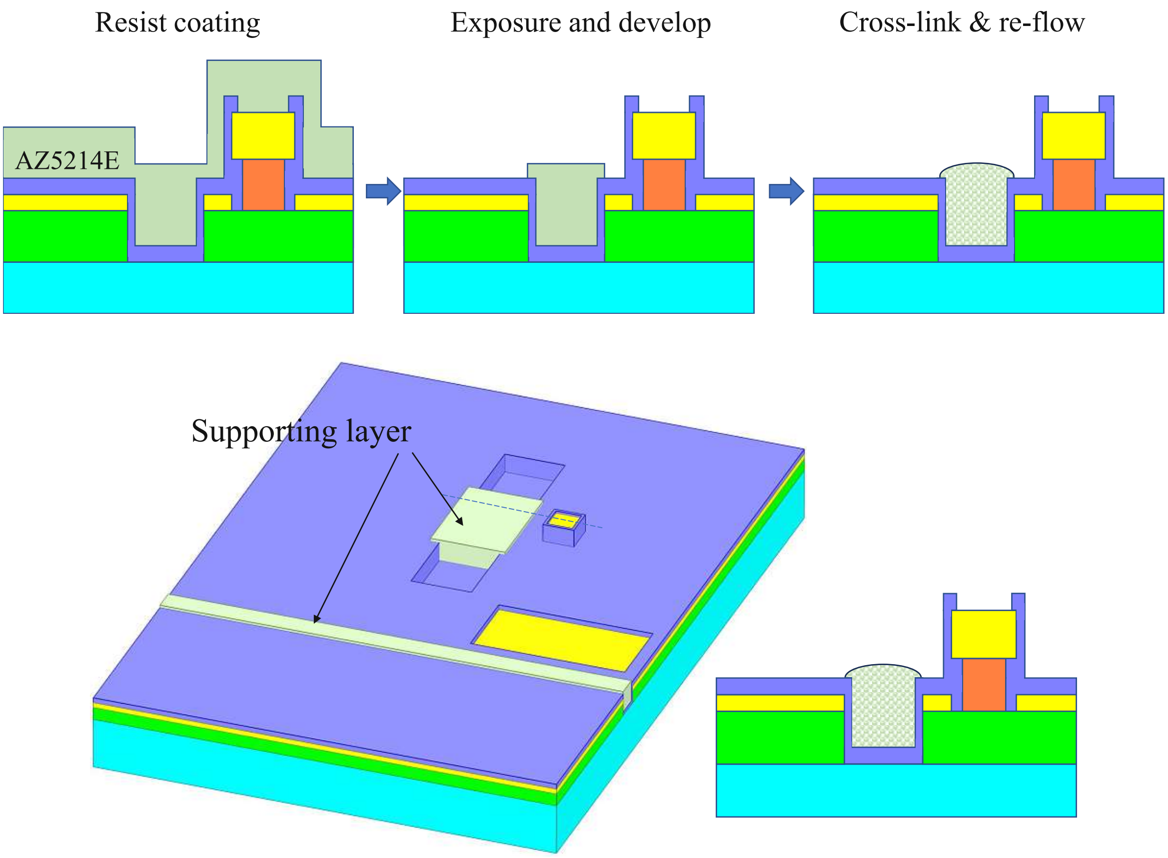

Figure 3.9: AZ5214E supporting layer

chosen for a shunt resistor as it has a low electrical resistivity. The dimension of the ITO shunt resistor depends on the DC characteristics of the RTD oscillators.

After depositing the shunt resistor, the supporting layer (cross-linked AZ5214E) under the bridge can be removed away using O_2 in RIE machine. However, all other steps afterwards, such as measurement, need to be done properly and carefully in order to avoid any cracks in the bridge side.

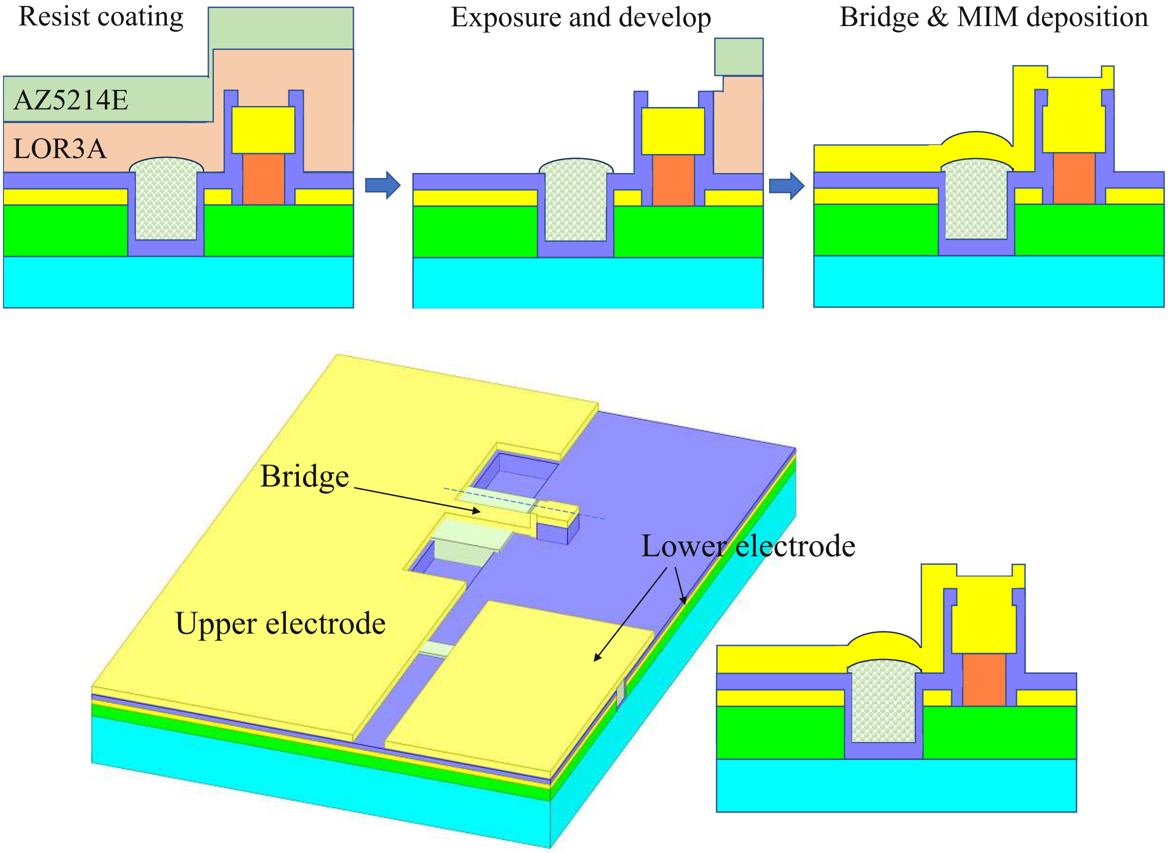

Figure 3.10: Bridge and MIM layer formation

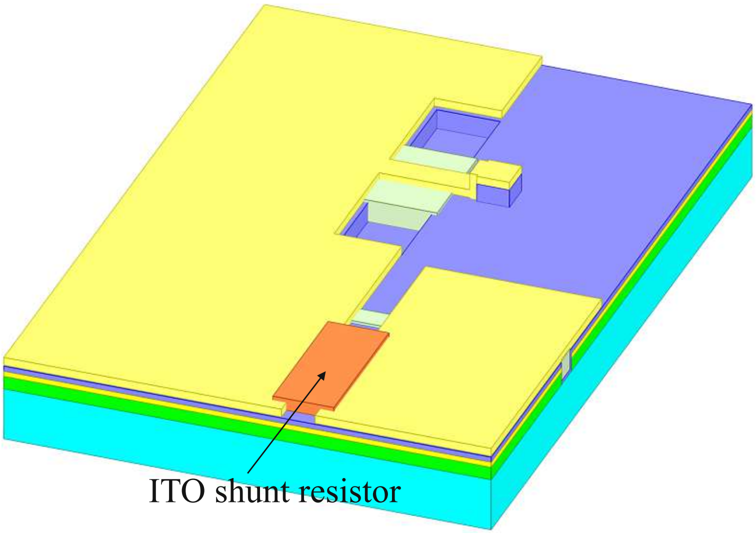

Figure 3.11: Deposition ITO shunt resistor

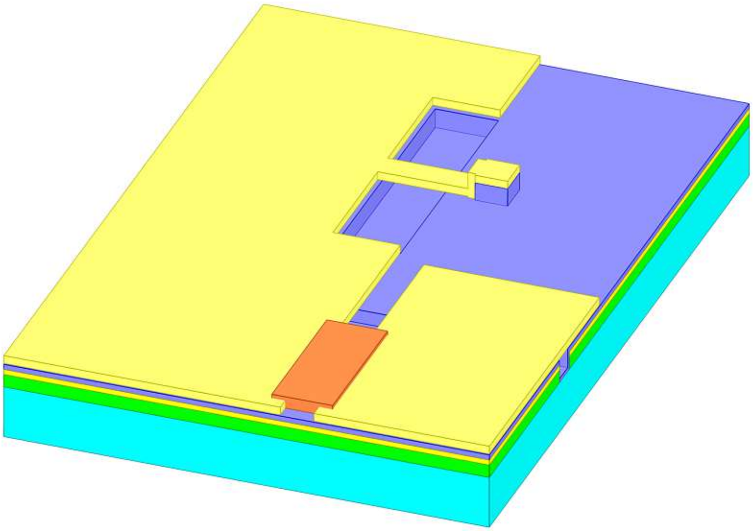

Figure 3.12: A final slot-antenna RTD oscillator

3.4 Frequency limitation of RTD oscillators

In order to make RTD oscillators working, the condition: $|G_{\mathrm{RTD}}| > G_{\mathrm{a}}$ must be satisfied, where G_{RTD} and G_{a} are the conductance of RTD and antennas. RTD oscillators stop working when RTD cannot provide enough NDC to compensate for the resonator losses or RTD cannot provide any gain at all beyond certain limiting frequencies, since NDC turns into PDC with increase of frequency. There are several factors which limit the oscillation frequency of RTD oscillator. Based on the concept of the RTD oscillators, three following factors are considered as the main reasons to the frequency limitation:

- Parasitics of the contacts
- Losses from antennas/resonators
- RTD dynamics

None of the above contributions is working independently, they are coupled due to the concept of the RTD oscillators. However, we can define the effect of each factor on the RTD oscillators when its parameters are considered predominate. The upper limitation of the oscillation frequency of an RTD oscillator can be defined based on the oscillation conditions.

3.4.1 Impact of the contact's parasitics

Fig. 3.13 shows the cross-section of the physical RTD connection to the circuit. The connectivity between the RTD layers and the circuit is established via semiconductor layers, which are subsequently interfaced with deposited metallic layers. The interface between a semiconductor and a metal results in the manifestation of contact resistance. The schematic illustration portrays the denotation of the contact resistance of the top contact as R_{c}. The homogeneity of the current along the top contact results in an inverse relationship between the contact resistance of the top contact and its contact area as $R_{\mathrm{c}} = \rho_{\mathrm{c}}/\mathrm{A}$, where ρ_{c} and A are the specific contact resistivity (its unit is $\Omega\mu\mathrm{m}^2$) and the active area of the RTD (in $\mu\mathrm{m}^2$). The interfaces of the contacts can be induced with a charge accumulation. The outcome of this phenomenon is the emergence of contact capacitance denoted as C_{c}, which operates in parallel with the contact resistance R_{c} and is directly proportional to the contact area $C_{\mathrm{c}} = c_{\mathrm{c}} \cdot \mathrm{A}$, where c_{c} is the specific contact capacitance (in $\Omega/\mu\mathrm{m}^2$).

The current that passes through the top contact and the RTD subsequently spreads into the severely doped semiconductor layer beneath the RTD and the metallic bottom contact.

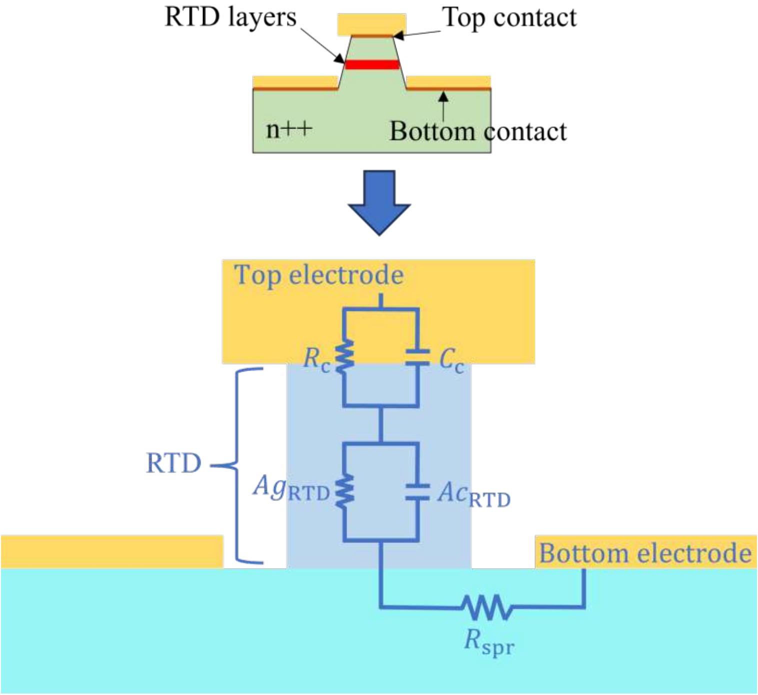

Figure 3.13: Cross-section of the physical RTD connection to the circuit and the corresponding equivalent circuit.

Because the current does not pass through the bottom contact uniformly in this situation, the relationship between the bottom equivalent contact resistance and the RTD area is more complicated than it is in the top contact instance. In the equivalent circuit, R_{spr} stands in for the resistance caused by current spread and scattered bottom contact resistance. Physically, the current paths also have a parasitic capacitance and inductance. Due to the RTD and its contacts' sub-micrometer scale, this inductance ordinary has a minimal impact, as seen in Ref. [115].

The contact parasitic elements are linked in a sequential manner within the oscillator circuit, interconnecting the RTD and the resonator. The frequency operational region is commonly constrained by an RC time constant that arises from contact parasitics. In order to ascertain the maximum operation frequency of an RTD, it is necessary to substitute it with the corresponding small-signal equivalent circuit. This circuit comprises of a parallel connection between the RTD capacitance (C_{RTD}) and conductance (G_{RTD}), as described in Ref. [4] and [115].

Typical values of the contact parasitics

The typical value of ρ_c in RTDs with InGaAs contact layers is 1-10 $\Omega\mu m^2$. Nonetheless, it is possible for the value to exceed 100 $\Omega\mu m^2$ if appropriate measures are not implemented to produce high-quality contacts. Terahertz resonant tunneling diodes (RTDs) typically feature narrow tunnel barriers, elevated current density, and pronounced negative differential conductance (NDC). In the context of RTDs, it is imperative that the working point falls within the NDC region and that the RTD exhibits DC stability in that region. This necessitates that the value of ρ_c be less than $-1/G^0_{\mathrm{RTD}}$, where G^0_{RTD} represents the specific static differential conductance of the RTD (G^0_{RTD} is negative in the NDC region). An RTD utilized in a 1.74 THz oscillator in [93] did not exhibit a record-high peak current density of $j_{\mathrm{RTD}} \approx$ 23.6 mA/μm^2. However, it did possess a value of $1/G^0_{\mathrm{RTD}} \approx -7.5$ $\Omega\mu m^2$. Consequentially, it is imperative that the value of ρ_c is maintained at a level lower than -1/G^0_{RTD}, in order to effectively bias the RTD within the NDC region.

The larger area of the bottom RTD contact is typically deemed less crucial, however, its impact on the overall contact resistance of the RTD should not be disregarded. This implies that the value of ρ_c must be lower than the one determined in the aforementioned evaluation.

Taking an example: the conductance and capacitance of an RTD are -50 mS/μm^2 and 12 fF/μm^2, respectively. The contact parasitics have the resistance value of 2 $\Omega\mu m^2$ and the capacitance value of 20 fF/μm^2. This RTD oscillator gives us the maximum frequency of $\approx$ 2.3 THz. Despite the fact that this is a very rough approximation, it is pretty near to the highest achieved oscillation frequency of the RTD oscillators, which is 1.98 THz, see [9], which was received with an RTD with the same parameters.

The importance of ρ_c on the frequency limitation of the RTD oscillators will also be shown in Chapter 5.

Spreading resistance

Subsequently, we will discuss the evaluation of the spreading resistance and its impact. This contribution is a result of the propagation of electrical currents within the semiconductor conducting layer beneath, which subsequently overflow onto a segment of the lower electrode.

An expression for the spreading resistance of a symmetric RTD can be derived using transmission line theory. This is typically applied to RTDs with cylindrical mesa geometry, see [116–118]. The validity of the transmission line method is contingent upon the transfer length, defined as the effective length of the contact wherein current is absorbed, being

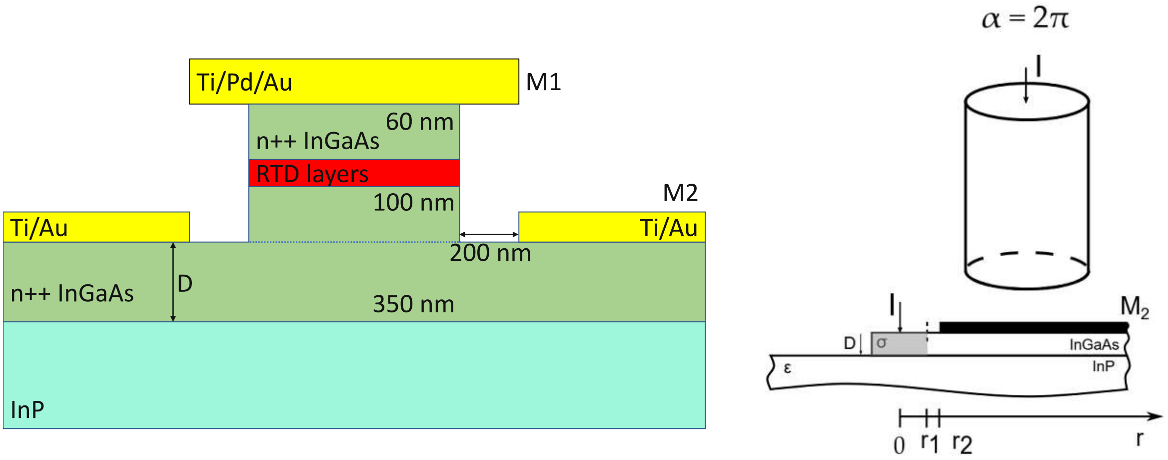

Figure 3.14: Cross section of an RTD contact layers

significantly greater than the thickness of the conductive layer. This assumption allows for a uniform current distribution within the semiconductor layer.

Fig. 3.14 describes the cross-section view and the top view of the spreading resistance for a symmetric RTD coupling with a slot-antenna. We have here: r is the radial coordinate, r_1 and r_2 (in µm) are the radius of the active area of the RTD and RTD mesa cap area covering by metal, respectively (the value of $r_2 - r_1$ defines the etching depth of RTD mesa). D is the depth (typical value of it is in the range of $0.5 - 1$ µm), and σ is the conductivity (in $\frac{\mathrm{S}}{\mathrm{m}}$) of the doped layer beneath the RTD layers (InGaAs in this example). ε is the permittivity of the semi-insulating substrate layer (InP for this example). M_2 is the bottom metal contact layer which is very large in comparison with the top RTD metal contact layer. I here is the current flowing through the RTD.

In order to calculate the value of the spreading resistance, we can write the following equations:

$$\mathrm{d}I = j\alpha r\mathrm{d}r \tag{3.1}$$

Taking the integral for both sides of Eq. 3.1, we have:

$$I(r) = j\alpha\frac{r^2}{2} \tag{3.2}$$

The electric field going in the InGaAs layer is defined as:

$$I(r) = \sigma E(r) r\alpha D \Rightarrow E(r) = \frac{1}{2}\frac{j}{\sigma D}r \tag{3.3}$$

And:

$$U = \int_0^{r_1} E(r)dr = \int_0^{r_1} \frac{1}{2}\frac{j}{\sigma D} r dr = \frac{1}{4}\frac{j}{\sigma D} r_1^2 \tag{3.4}$$

$$R = \frac{U}{I(r_1)} = \frac{1}{2}\frac{1}{\sigma D \alpha} \tag{3.5}$$

The spreading resistance then is defined as following:

$$R_{\mathrm{spr}} = \sum R = \frac{R_{\mathrm{sh}}}{\pi}\left\{\frac{1}{4} + \ln\left(\frac{r_2}{r_1}\right) + \frac{K_0(\frac{r_2}{L_\mathrm{T}})L_\mathrm{T}}{K_1(\frac{r_2}{L_\mathrm{T}})r_2}\right\} \tag{3.6}$$

Where K_0 and K_1 are the modified Bessel functions of zero and first orders, respectively. L_T and R_{sh} are the transfer length (in µm) and the sheet resistance (in Ω):

$$L_\mathrm{T} = \sqrt{\frac{\rho_\mathrm{c}}{R_{\mathrm{sh}}}} \tag{3.7}$$

$$R_{\mathrm{sh}} = \frac{1}{\sigma D} \tag{3.8}$$

with ρ_c is the contact resistivity (in Ωµm^2).

Taking an example as following (see Fig. 3.14): The active area A of an RTD is 0.21 µm^2, the conductivity σ_{InGaAs} and the depth D of the n++ InGaAs layer (with doping of 3×10^{19} cm^{-3}) are 3.93×10^5 $\frac{\mathrm{S}}{\mathrm{m}}$ and 350 nm, respectively. The top $\rho_{\mathrm{c},1}$ and the bottom $\rho_{\mathrm{c},2}$ contact resistivity are 2 Ωµm^2 and 10 Ωµm^2, respectively. By using Eq. 3.6, the spreading resistance R_{spr} in this case is 4.9 Ω. This value of R_{spr} is somehow comparable with Ref. [97] which had R_{spr} of 4 Ω with D = 400 nm, and 2 Ω with D = 600 nm.

We should notice that all the above equations are formulated for the DC case (frequency is zero). As the frequency changes, the transfer length L_T will change, as a result the spreading resistance will also change. The dependence of the spreading resistance on the frequency (with different values of RTD area A) can be seen in the Fig. 3.15.

From Fig. 3.16, we can notice that both the top contact resistance and the spreading resistance decrease with increasing of frequency. For example, at DC case (frequency is zero), R_c and R_{spr} are 10 Ω and 2.84 Ω, respectively; however, these values at HF case (high frequency, for example at 2 THz) are 7.98 Ω and 2.14 Ω, respectively. In the high-frequency regime, the RTD areas of the RTD oscillators are quite small (in the range from 0.1 µm^2 to 0.5 µm^2). The spreading resistance R_{spr} of these RTD areas has small impact; however, the top contact resistance R_c plays a huge contribution on the total parasitic resistance. The

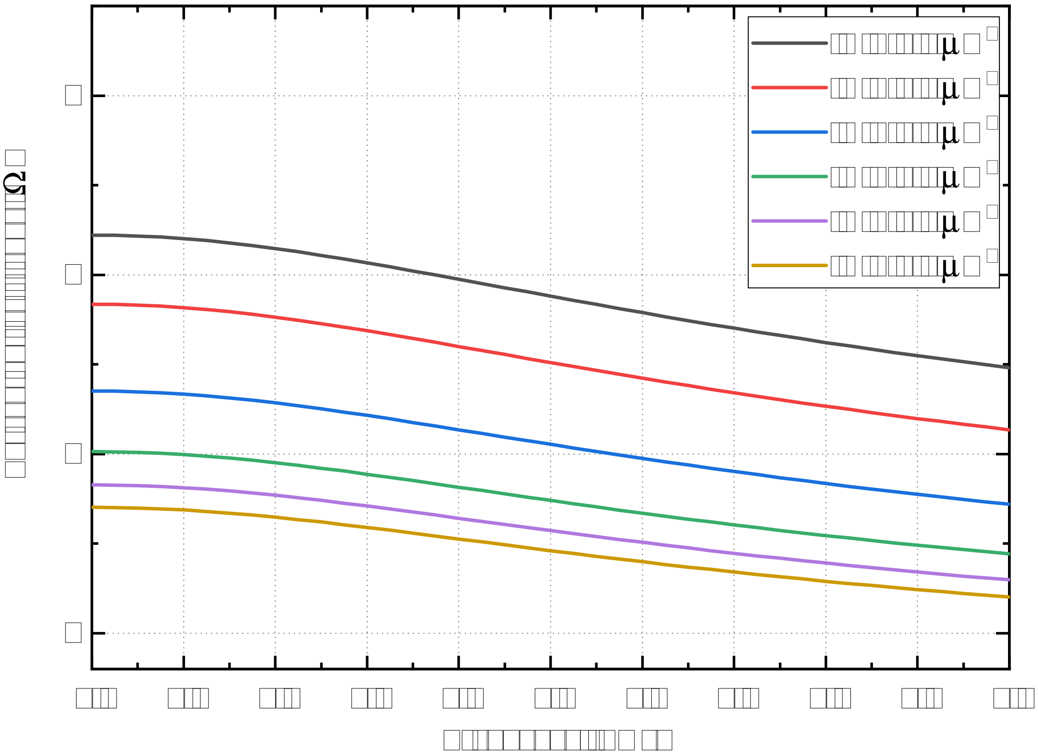

Figure 3.15: Dependence of the spreading resistance on the frequency with different RTD areas.

spreading resistance is dominant for large RTD areas (from ∼ 1.0 μm^2 in the DC case, or from ∼ 1.2 μm^2 in the HF case).

Frequency limitation of RTD oscillators

Next, we will introduce the impact of both contact parasitics and spreading resistance on the slot-antenna RTD oscillator to have an estimation on frequency limitation of the system. The results are calculated regarding the equivalent circuit of the RTD oscillator in Fig. 2.16. For investigating the frequency limitation of RTD oscillators, we can only use the small-signal model for RTD conductance and capacitance, see more details in section 3.5.

The conductance and capacitance of the RTD are calculated as:

$$G_{\text{RTD}} = g_{\text{RTD}} \cdot A, \tag{3.9}$$

$$C_{\text{RTD}} = c_{\text{RTD}} \cdot A, \tag{3.10}$$

where g_{RTD}, c_{RTD} are the specific conductance, capacitance (per unit area), and A is the mesa area of the RTD.

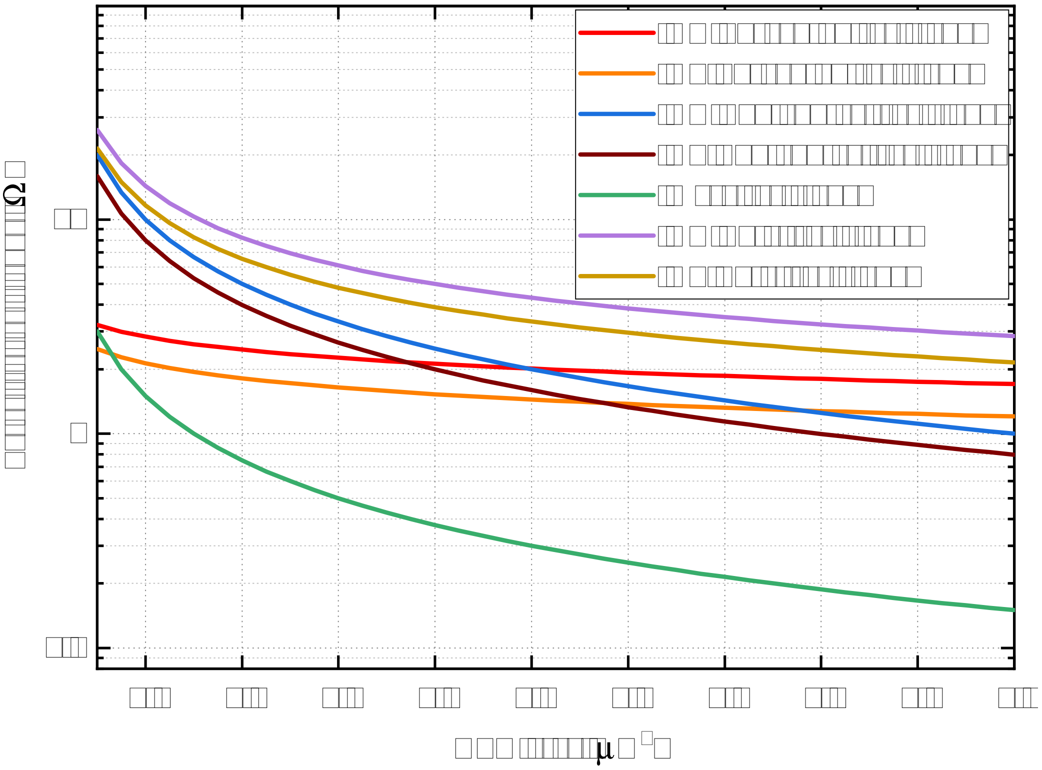

Figure 3.16: Comparison of the contributions of the parasitic resistances. The RTD area is from 0.1 to 2.0 µm^2. The HS case is considered as the frequency at 2 THz.

The admittance of the RTD and the contact parasitics are written as:

$$Y_{\mathrm{RTD}} = G_{\mathrm{RTD}} + i \cdot \omega \cdot C_{\mathrm{RTD}}, \tag{3.11}$$

$$Y_{\mathrm{c}} = \frac{1}{R_{\mathrm{c}}} + i \cdot \omega \cdot C_{\mathrm{c}}, \tag{3.12}$$

with R_{c} and C_{c} are the contact resistance and capacitance.

The admittance of the circuit from the left side of the points 2-2’ in Fig. 2.16 (including antenna, contact parasitics and spreading components) is:

$$Y_{\mathrm{circ}} = \left(\frac{1}{Y_{\mathrm{a}}} + \frac{1}{Y_{\mathrm{c}}} + R_{\mathrm{spr}}\right)^{-1}, \tag{3.13}$$

where R_{spr} is the spreading resistance, Y_{a} is the antenna admittance (the parasitic RTD capacitance C_{par} is included in Y_{a} as a parallel capacitor to the antenna).

We can then write the total admittance of the RTD oscillator as:

$$Y_{\mathrm{total}} = Y_{\mathrm{circ}} + Y_{\mathrm{RTD}}, \tag{3.14}$$

or:

$$\mathrm{Re}(Y_{\mathrm{total}}) = \mathrm{Re}(Y_{\mathrm{circ}}) + G_{\mathrm{RTD}}, \tag{3.15}$$

$$\mathrm{Im}(Y_{\mathrm{total}}) = \mathrm{Im}(Y_{\mathrm{circ}}) + \omega \cdot C_{\mathrm{RTD}}. \tag{3.16}$$

The oscillation condition is satisfied when $\mathrm{Im}(Y_{\mathrm{total}}) = 0$, and $\mathrm{Re}(Y_{\mathrm{total}}) < 0$.

Figure 3.17 shows the dependence of the frequency limitation of the slot-antenna RTD oscillator on the RTD area with different values of the contact resistivity ρ_c from 1 to 10 $\Omega\mu\mathrm{m}^2$, The RTD specific contact capacitance c_c is taken as 19 $\mathrm{fF}/\mu\mathrm{m}^2$, and the parasitic RTD capacitance C_{par} is assumed $\sim$ 1 $\mathrm{fF}/\mu\mathrm{m}^2$. In this example, only the contact parasitics are taken into account of the system. The width of the slot antenna is 4 μm, and the length varies from 12 to 100 μm. The RTD in this case has 1.6 nm thick barrier with the peak current density of around 6 $\mathrm{mA}/\mu\mathrm{m}^2$. The points in the brackets show the RTD area and the maximum oscillation frequency that the RTD oscillator can achieve with certain value of the contact resistivity. The highest oscillation frequency in this case is about 732 GHz on the RTD oscillator with 1.5 $\mu\mathrm{m}^2$ RTD, 20 μm slot-antenna length, and the contact resistivity 1 $\Omega\mu\mathrm{m}^2$.

The spreading resistance now is also taken into the system together with the contact parasitics. As can be seen from Figure 3.18, the maximum oscillation frequencies of the RTD oscillator decrease a lot in comparison with the above case when only the contact parasitics are involved in the system. The highest oscillation frequency in this case is about 480 GHz on the RTD oscillator with 1.5 $\mu\mathrm{m}^2$ RTD, 50 μm slot-antenna length, and the contact resistivity 1 $\Omega\mu\mathrm{m}^2$.

Figures 3.17 and 3.18 also show that for small RTD areas (in the range of 1 $\mu\mathrm{m}^2$), the maximum oscillation frequencies change not much (correspond to the antennas with lengths 75 μm and 100 μm). In this RTD area range, as discussed above, the contact resistance is dominant over the spreading resistance, see Fig. 3.16. For the larger RTD areas, where the impact of the spreading resistance is dominant, the maximum oscillation frequencies decrease a lot in the case when the spreading resistance is employed to the system (Fig. 3.18).

Based on the results represented in Fig. 3.18, one can define the antenna parameters (length and width) and the RTD area in order to achieve the highest oscillation frequencies of the slot-antenna RTD oscillator on certain contact resistivity for a given RTD wafer. However, together with maximizing oscillation frequencies, achieving high output powers of the RTD oscillators is also important, and it will be addressed in the next chapter.

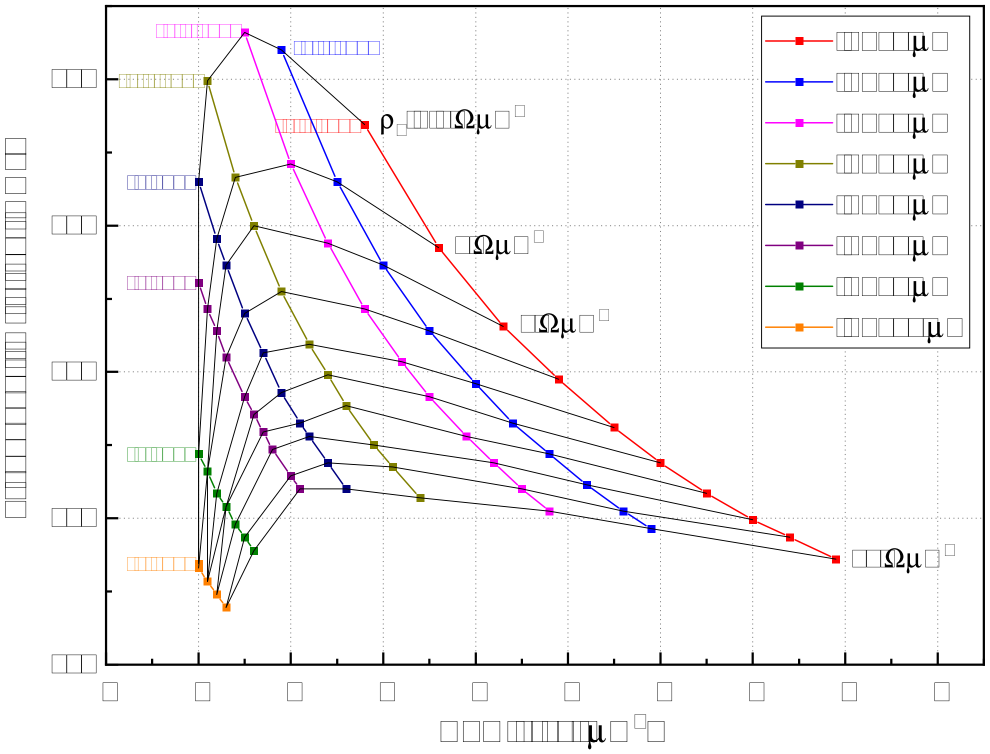

Figure 3.17: : The dependence of the frequency limitation of the slot-antenna RTD oscillator on the RTD area with different contact resistivity. Only the contact parasitics are taken into account in this case.

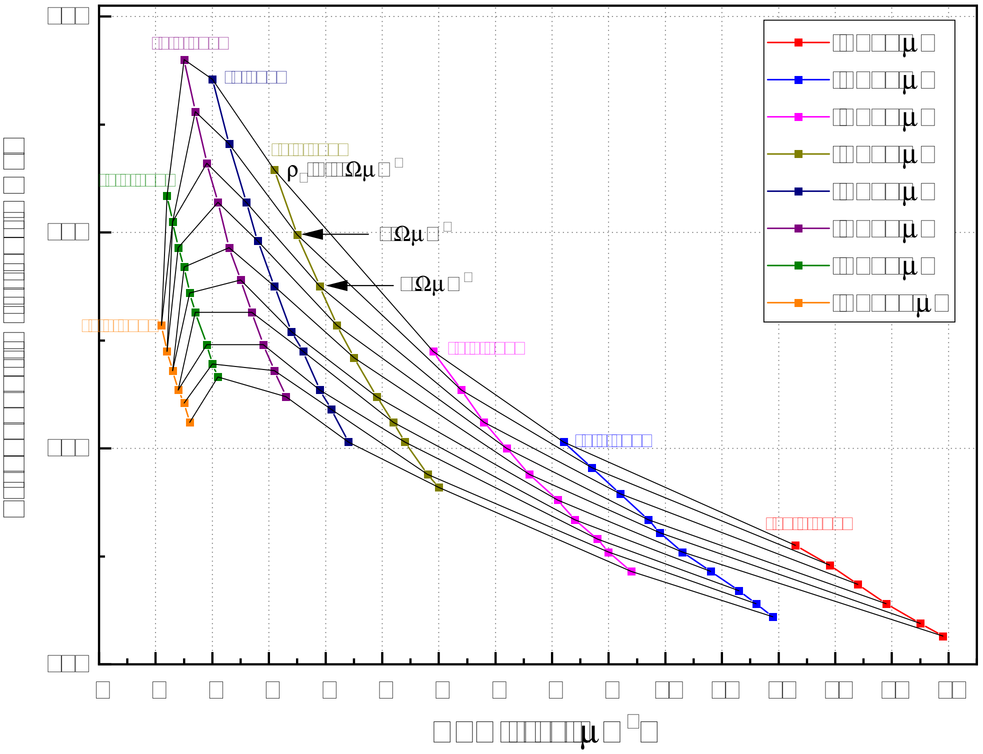

Figure 3.18: : The dependence of the frequency limitation of the slot-antenna RTD oscillator on the RTD area with different contact resistivity. The contact parasitics and spreading resistance are taken into account in this case.

3.4.2 Resonator/Antenna losses

In order to increase the oscillation frequency, it is necessary to bring the antenna loss down to a lower value. The losses of the antenna consist of conduction loss and radiation loss. In a short antenna, the conduction loss accounts for the majority of the total antenna losses as the radiation conductance is quite small (was approximately one tenth that of the antenna conductance $\mathrm{Re}(Y_\mathrm{a})$. A decrease in the antenna's conduction loss is required in order to achieve an additional increase in the oscillation frequency limit. Further discussion about reducing antenna losses will be shown in Chapter 5.

3.5 Conclusions

In this chapter, we have presented the structure design of the symmetrical slot-antenna RTD oscillator. We have shown the general fabrication processes of the RTD oscillator, and we have explored the key design considerations for developing RTD oscillators in both cases of high oscillation frequencies and high output powers.

Next, we have presented the simulation model of RTD oscillators where we use a small-signal analysis for calculating the oscillation frequencies and s large-signal analysis for the output powers. Lastly, we have described some factors that limit the maximum oscillation frequencies os the RTD oscillators, such as the contact parasitics, the spreading resistance, the antenna losses. By adjusting the effects of these parasitic elements, we can define the parameters of the antenna (such as the length and the width of the slot antenna) and the RTD mesa areas to maximize the oscillation frequencies of the RTD oscillators for a given RTD wafer.

Chapter 4

Impact of Slot Width on Performance of Symmetrical-Slot-Antenna Resonant-Tunneling-Diode Oscillators

Results shown in this chapter were published in the peer-reviewed journal article **Dinh Tuan Nguyen**, Gabriele Picco, Petr Ourednik, Christian Spudat, and Michael Feiginov, “Impact of slot width on performance of symmetrical-slot-antenna resonant-tunneling-diode oscillators,” *IEEE Transactions on Terahertz Science and Technology*.

4.1 Introduction

The slot-antenna RTD oscillator is one of the most simple type of sub-THz and THz oscillators. The slot antenna integrated to the RTD oscillators acts simultaneously as a resonator and a radiator. The RTD is, in this case, directly placed on one side of the slot antenna. The simple slot-antenna oscillators radiate output power into the substrate and require to be mounted on a relatively bulky Si lens to out-couple their radiation;

We can categorize the on-chip slot-antenna RTD oscillators into two basic variants: symmetric and asymmetric, see also Chapter 2. By symmetric slot antenna, we mean that both arms of the slot antenna have the same lengths, i.e., the RTD is connected to the slot antenna at the middle of its length. The reason why we use the symmetric design was discussed in Chapter 1 and Chapter 3.

A symmetrical slot antenna with an RTD in the slot center is defined by two parameters: slot length (l) and width (w). The slot length is chosen according to the target oscillator frequency: the higher the frequency, the shorter the slot. On the other hand, the slot width is typically chosen to be equal to 4 µm in the sub-THz and THz RTD oscillators [9], [105, 119–121, 57]. Usually, the slot width is not used as a degree of freedom in the optimization of the oscillators. There is just one publication [122] where the impact of the variation of the slot width on the characteristics of on-chip symmetrical-slot-antenna RTD oscillators was studied (it should noted that the impact of the radiator width on the performance of asymmetrical-slot RTD oscillators was studied in more details, see [123]). In [122], it was indicated that the oscillation frequency increases with the decrease in the slot width. This tendency was confirmed by experimental data with 2 and 4 µm wide slot antennas at ≈350 GHz. In the same work, it was expected that the output power of RTD oscillators should be almost independent of the slot width.

In the present work, we show that the output power of symmetrical-slot-antenna RTD oscillators depends on the slot width. Although the dependence is not very strong for wider slots, it could be used as a fine tuning degree of freedom to increase the output power of the oscillators. The fine-tuning mechanism is related to maximizing the RTD-oscillation amplitude by a proper balance between the slot-antenna radiation and ohmic losses, and the slot susceptance. In this work, we present an extensive set of experimental data on RTD oscillators with different slot widths, which is in reasonably good agreement with the theory to prove the validity of the impact of the slot width on the oscillator characteristics. We report the output powers of 283 µW at 184 GHz and 82 µW at 368 GHz, which are very close to the state-of-the-art literature data for the given type of RTD oscillators.

4.2 Design of slot-antenna RTD oscillators and their output power

The schematic of a symmetrical slot-antenna RTD oscillator we investigate in this work is shown in Fig. 3.1. The oscillator consists of two main parts: (i) the RTD as a source of spontaneous oscillations; (ii) slot antenna as the radiator and resonator that defines the fundamental frequency of the oscillator. The RTD requires DC biasing to bring it into the oscillation region. A conductive bridge over the slot is needed to grant that the RTD mesa top electrode and the opposite side of the antenna, where the bias is applied, are connected, see Fig. 3.1. Also, to separate the DC biasing circuit from the ac circuit of the oscillator, a metal-insulator-metal (MIM) structure is required. In addition, a shunt resistor is needed to suppress low-frequency parasitic oscillations in external circuits including the bias line.

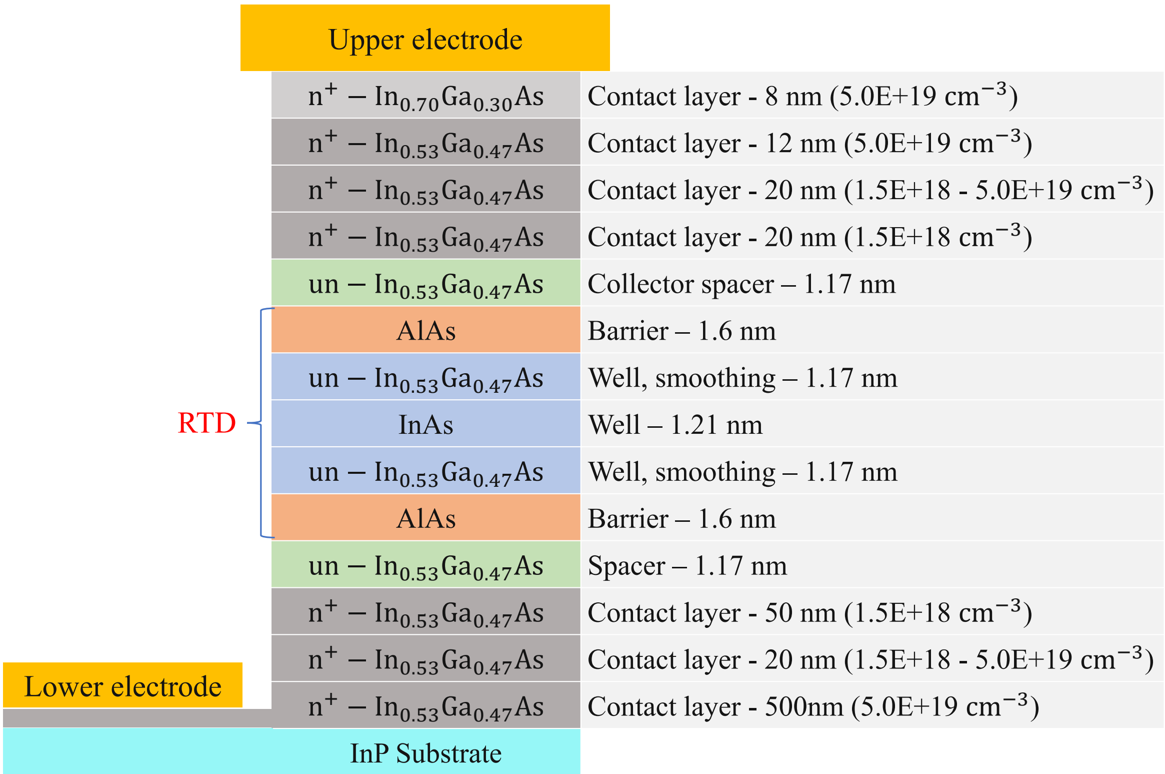

$n^+ - In_{0.70}Ga_{0.30}As$	Contact layer - 8 nm (5.0E+19 cm^{-3})
$n^+ - In_{0.53}Ga_{0.47}As$	Contact layer - 12 nm (5.0E+19 cm^{-3})
$n^+ - In_{0.53}Ga_{0.47}As$	Contact layer - 20 nm (1.5E+18 - 5.0E+19 cm^{-3})
$n^+ - In_{0.53}Ga_{0.47}As$	Contact layer - 20 nm (1.5E+18 cm^{-3})
$un - In_{0.53}Ga_{0.47}As$	Collector spacer – 1.17 nm
AlAs	Barrier – 1.6 nm
$un - In_{0.53}Ga_{0.47}As$	Well, smoothing – 1.17 nm
InAs	Well – 1.21 nm
$un - In_{0.53}Ga_{0.47}As$	Well, smoothing – 1.17 nm
AlAs	Barrier – 1.6 nm
$un - In_{0.53}Ga_{0.47}As$	Spacer – 1.17 nm
$n^+ - In_{0.53}Ga_{0.47}As$	Contact layer - 50 nm (1.5E+18 cm^{-3})
$n^+ - In_{0.53}Ga_{0.47}As$	Contact layer - 20 nm (1.5E+18 - 5.0E+19 cm^{-3})
$n^+ - In_{0.53}Ga_{0.47}As$	Contact layer - 500nm (5.0E+19 cm^{-3})

Figure 4.1: RTD-wafer parameters.

The oscillation condition of the structure is satisfied when the negative differential conductance (NDC) of the RTD compensates for the conductance of the external circuit (including the slot antenna and parasitic elements) as shown in Eqs. (2.11) and (2.12). The output power (P) of an RTD oscillator can be calculated with the Eq. (2.13) as:

$$P = \frac{1}{2}\left|\frac{Y_{\mathrm{circ}}}{Y_{\mathrm{a}}}\right|^2 G_{\mathrm{r}} V_{\mathrm{AC}}^2.$$

4.3 1.6nm RTD parameters

In this study, a double barrier InGaAs/AlAs resonant tunneling diode (RTD) has been employed, which was grown on an InP substrate, see more detailed in Fig. 4.1. The layer design of these RTDs is comparable to the one utilized in previous RTD oscillators, as documented in references [5], [124–126]. The RTDs utilized AlAs barriers with a thickness of 1.6 nm, which were positioned on either side of a composite quantum well (QW) consisting of $In_{0.53}Ga_{0.47}As/AlAs/In_{0.53}Ga_{0.47}$. Each sublayer within the QW had a nominal thickness of 1.2 nm. The $In_{0.53}Ga_{0.47}$ layers that enclose the barriers are doped with n-type impurities

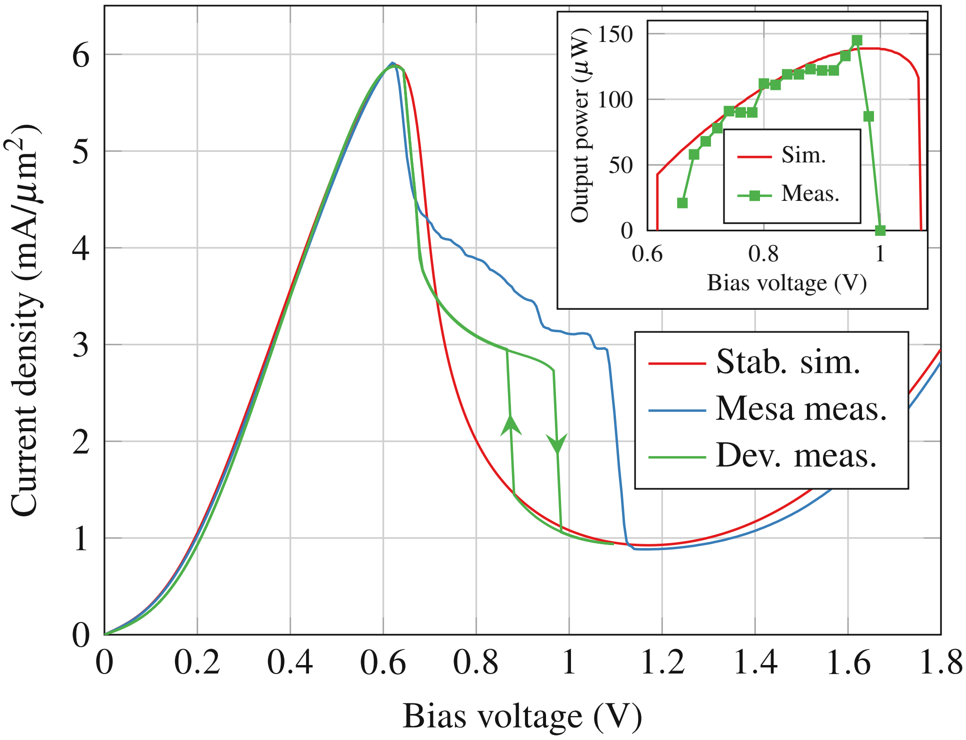

Figure 4.2: I-V curves of a 2.0 µm^2 RTD integrated with a slot antenna with 150 µm length. The measured I-V curve is shown in green, the simulated one in red, and the I-V curve of a free-standing RTD is shown in blue. The inset shows the dependence of the oscillator output power on the bias voltage.

at a concentration of $1.5 \times 10^{18}\mathrm{cm}^{-3}$, with the exception of 1.2 nm undoped spacers located directly adjacent to the barriers. The $\mathrm{In}_{0.53}\mathrm{Ga}_{0.47}$ layers located further away were doped with a nominal concentration of $5 \times 10^{19}\mathrm{cm}^{-3}$.

Figure 4.2 shows the I-V characteristics of 1.6 nm barrier RTD with an area of 2.0 µm^2. All the curves are normalized to the value of the current density of the RTD which is $\approx$ 5.8 mA/µm^2. The PVCR of this RTD is around 9. The theoretical I-V curve is shown in red color. The blue curve shows the experiment data of the RTD before the ITO shunt resistor deposition, and the green one is the data in the oscillation mode after subtraction the ITO shunt resistance. Those are typical parameters for RTDs used in the sub-THz frequency range. In the past, we have used this wafer in the RTD oscillators, working at frequencies of $\approx$100-500 GHz [57], [98]. We also use this RTD wafer in the experimental part of this work.

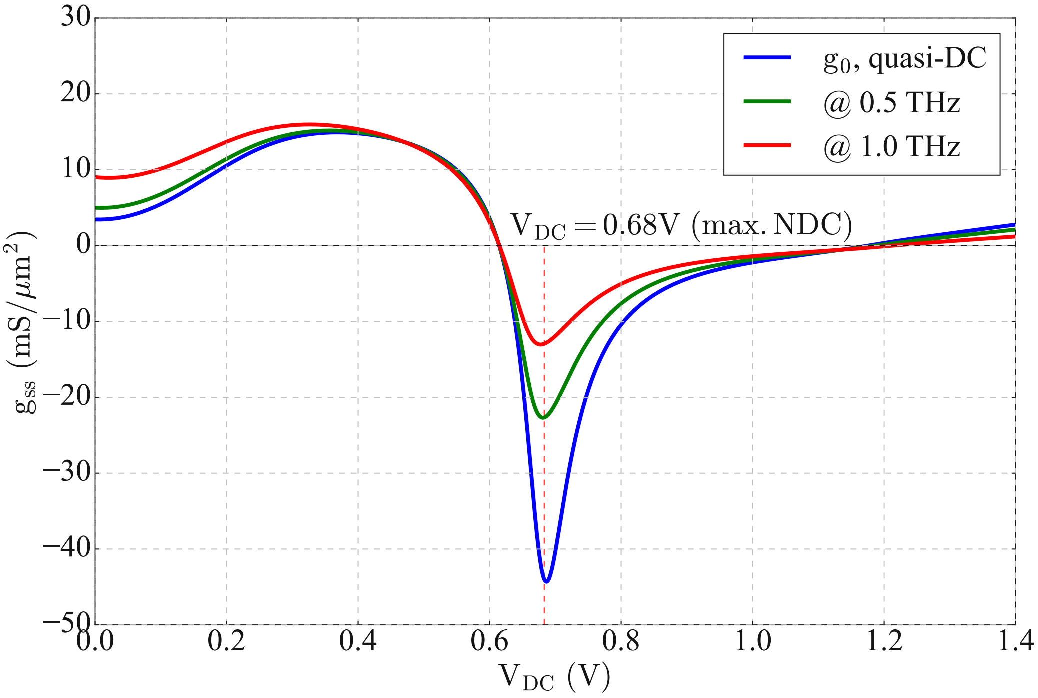

Figure 4.3: Dependence of the small-signal RTD conductance on the bias voltage, $g_{SS}(V_{DC})$, in the quasi-DC case and at several frequencies.

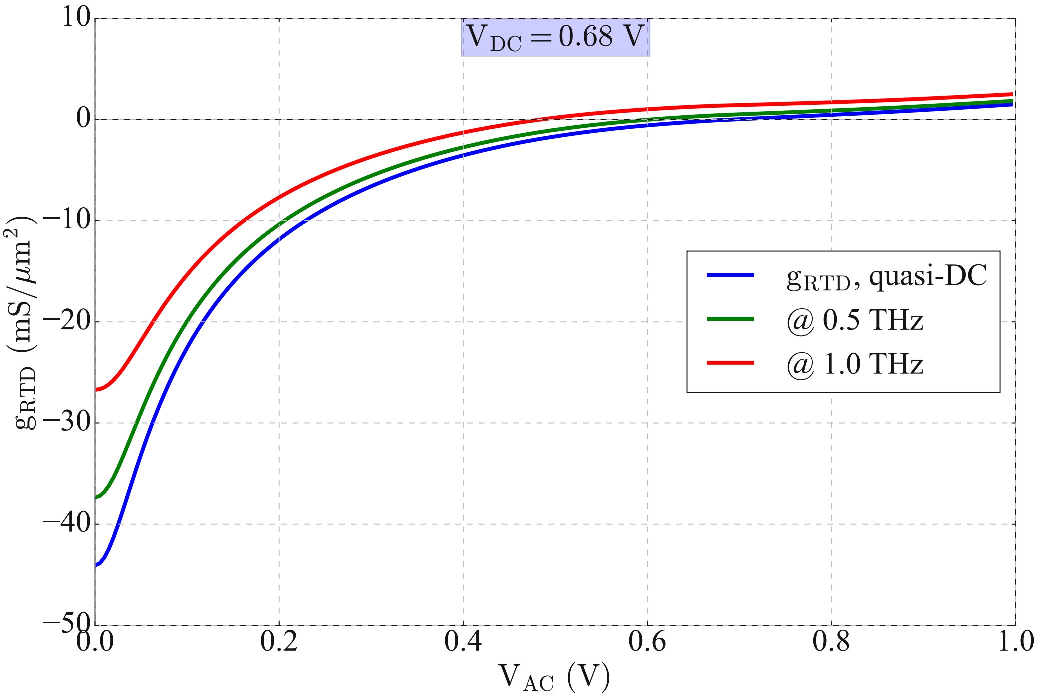

Figure 4.4: Dependence of the RTD conductance on the AC voltage amplitude, $g_{RTD}(V_{AC})$, at V_{DC}=0.68 V in the quasi-DC case and at several frequencies.

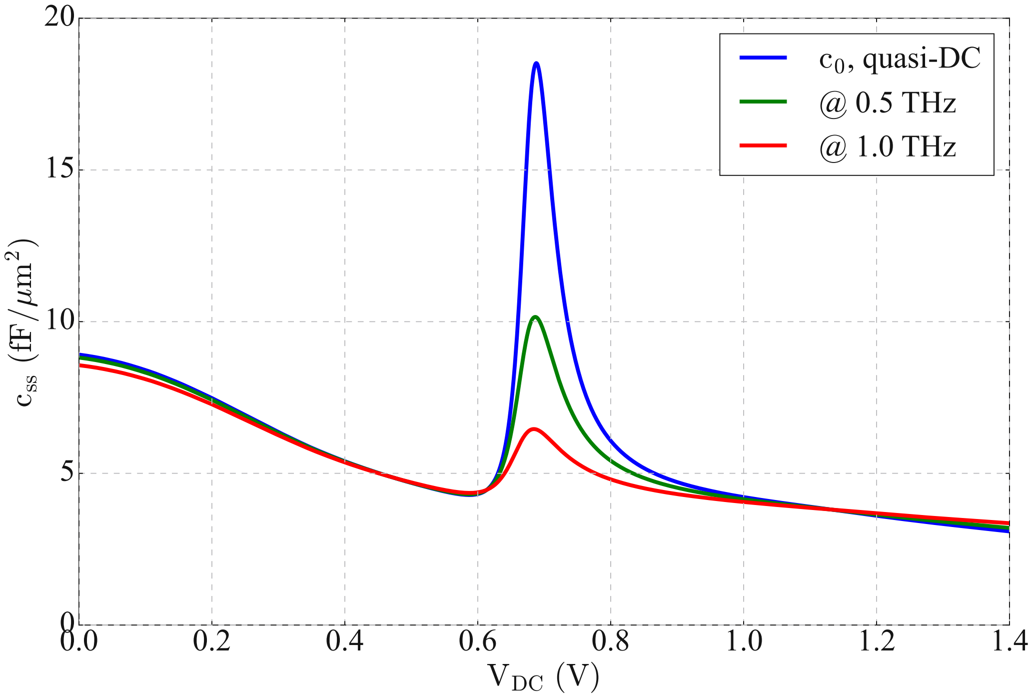

Figure 4.5: Dependence of the small-signal RTD capacitance on the bias voltage, $c_{SS}(V_{DC})$, in the quasi-DC case and at several frequencies.

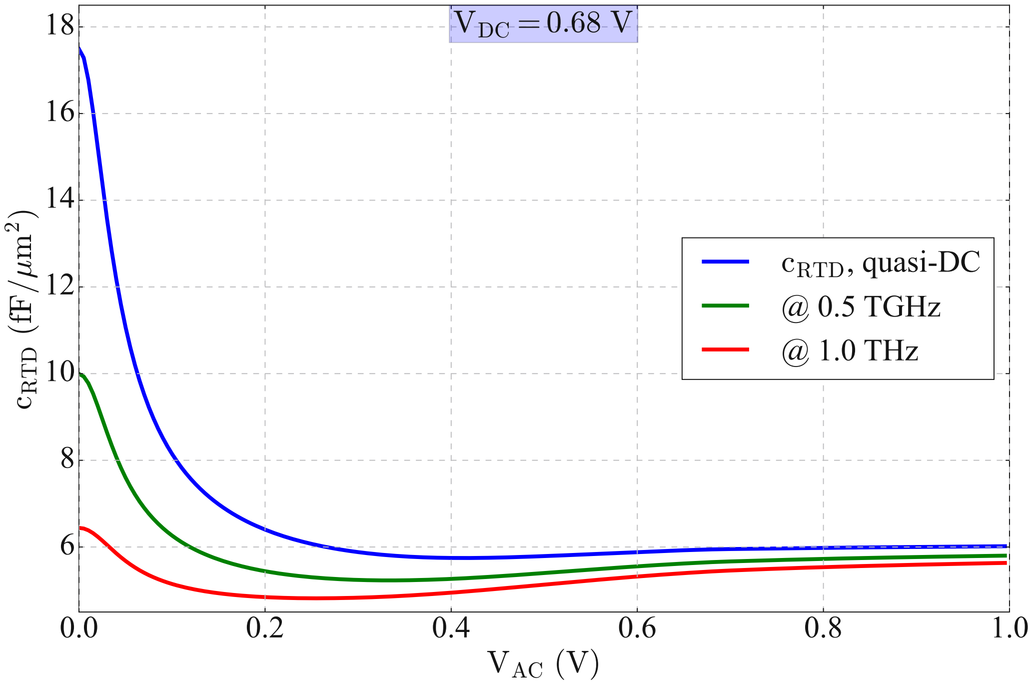

Figure 4.6: Dependence of the RTD capacitance on the AC voltage amplitude, $c_{RTD}(V_{AC})$, at V_{DC}=0.68 V in the quasi-DC case and at several frequencies.

Based on the simulation analysis in the chapter 2, we calculate the small-signal RTD conductance g_{SS}, capacitance c_{SS} dependence on applied voltage V_{DC}, also the RTD conductance g_{RTD} and capacitance c_{RTD} on the AC voltage amplitude V_{AC}. Figure 4.3 shows $g_{\mathrm{SS}}(V_{\mathrm{DC}})$ in the quasi-static regime and at the frequencies of 0.5 THz and 1.0 THz. The maximum of the static NDC is achieved at the DC bias of 0.68 V. The variation of $g_{\mathrm{RTD}}(\omega, V_{\mathrm{AC}})$ at V_{DC}=0.68 V with V_{AC} in the quasi-static regime and at several frequencies is shown in Fig. 4.4; the plots are calculated with Eq. (2.15). Fig. 4.5 shows SS RTD capacitance ($c_{\mathrm{SS}}(V_{\mathrm{DC}})$) calculated with Eq. (2.17) at several frequencies. Fig. 4.6 illustrates variation of $c_{\mathrm{RTD}}(\omega, V_{\mathrm{AC}})$ with V_{AC} calculated with Eq. (2.16), V_{DC} was taken equal to 0.68 V. In this work, the analysis of the oscillation frequencies and oscillator output power was performed assuming that the RTD is operated at V_{DC}=0.68 V, where NDC has a maximum.

4.4 Numerical simulations

For the simulation of the antenna characteristics (admittance, radiation and loss conductances, etc.), we used a commercial electromagnetic simulator (ANSYS HFSS). For given slot-antenna dimensions, the simulated antenna admittance is substituted into Eqs. (2.11) and (2.12), the equations are then solved for different RTD areas (A), giving the corresponding oscillation frequencies and the steady-oscillation amplitude (V_{AC}). Afterward, in the general case, the oscillator output power is calculated with Eq. (2.13).

The full analysis and numerical simulations of this work were clearly described in ref. [REF:impact of slot width...]. This section will show some results of these simulations (which were done by our colleagues who are also the main contributors of the article) combining with a set of experiment data.

In this study, we assume the RTD contact resistance of $\rho_c = 2\ \Omega\,\mu m^2$. The simulation results in this case for the output power at 375 GHz are shown in Fig. 4.7. The maximum output power is ≈90 µW. An optimal slot geometry to achieve the global power maximum are: slot length is ≈80-90 µm and the slot width is ≈5 µm. Fig. 4.8 shows similar simulation data for approximately twice the lower frequency of 185 GHz. The global maximum of ≈300 µW should be achieved for the slot length of ≈200-210 µm and the slot width of ≈5-6 µm.

Figs. 4.7 and 4.8 also include contour lines for the RTD-mesa area required for each combination of the slot length and width to make the oscillator work at the chosen frequencies. The contour lines indicate that the RTD-mesa areas decrease with the increase of w, since the antenna susceptance B_{a} drops and that needs to be compensated by the reduction of

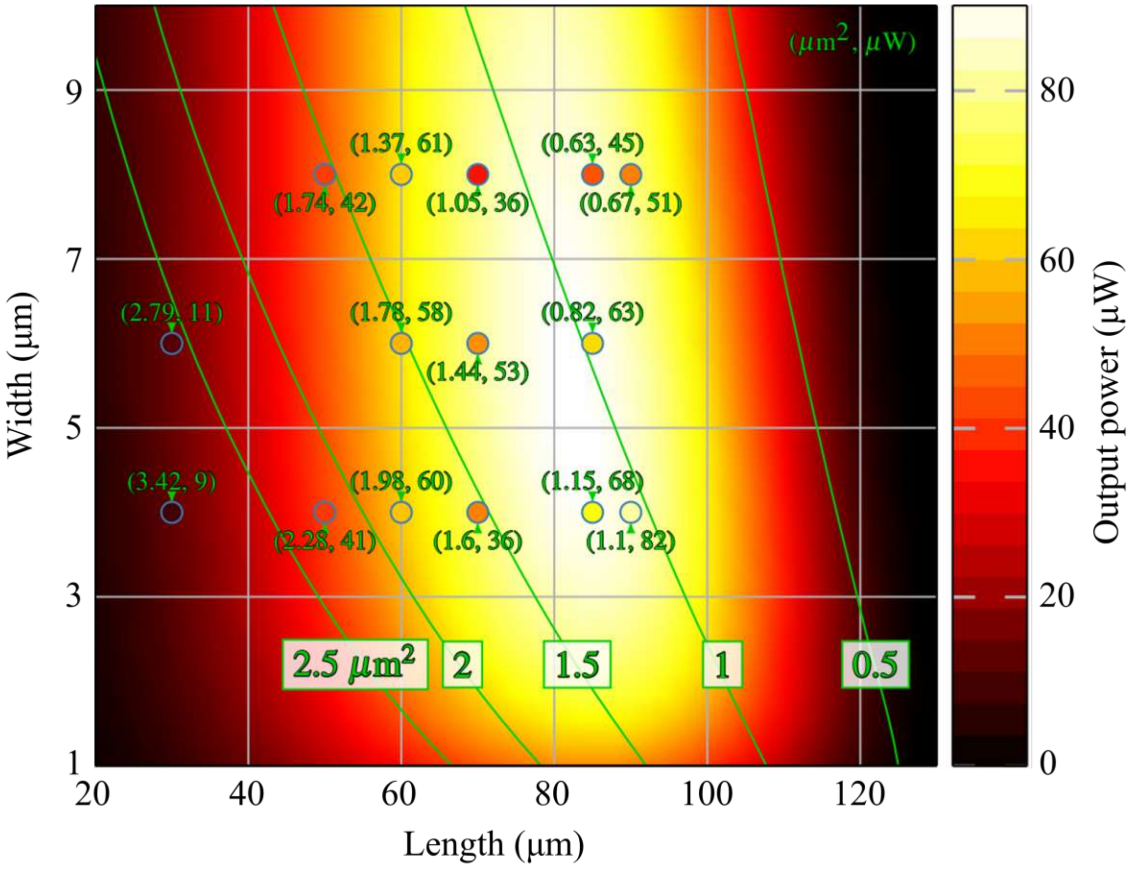

Figure 4.7: Color map of the output power of slot-antenna RTD oscillators at 375 GHz. The green contour lines show the design RTD-mesa area in µm^2 to achieve the target oscillation frequency. The color dots represent the experimental data for RTD oscillators working in the frequency range of 375±10 GHz. The first number next to each dot shows the RTD-mesa area, and the second one gives the output power (also indicated by the dot color) for each oscillator.

the RTD-mesa area. This behavior also aligns with the observation made in [122] that the oscillation frequency increases with the decrease of the slot width. Indeed, one can see the increase of RTD-mesa area with the decrease of w as a means to reduce the oscillation frequency: if the RTD-mesa area would be kept fixed with the decrease of w, then the oscillation frequency would increase. However, decreasing the slot width is not an optimal design strategy: as Figs. 4.7 and 4.8 show, if the slot width is made too narrow, then the output power will reduce; there is an optimal parameter range for the slot antennas to get the highest output power at a given frequency. Specifically, for the RTD wafer we use and for the given frequencies, an optimal slot width is in the range of ≈4-8 µm. If the slot width were reduced to 2 µm that should have led to a certain output-power reduction.

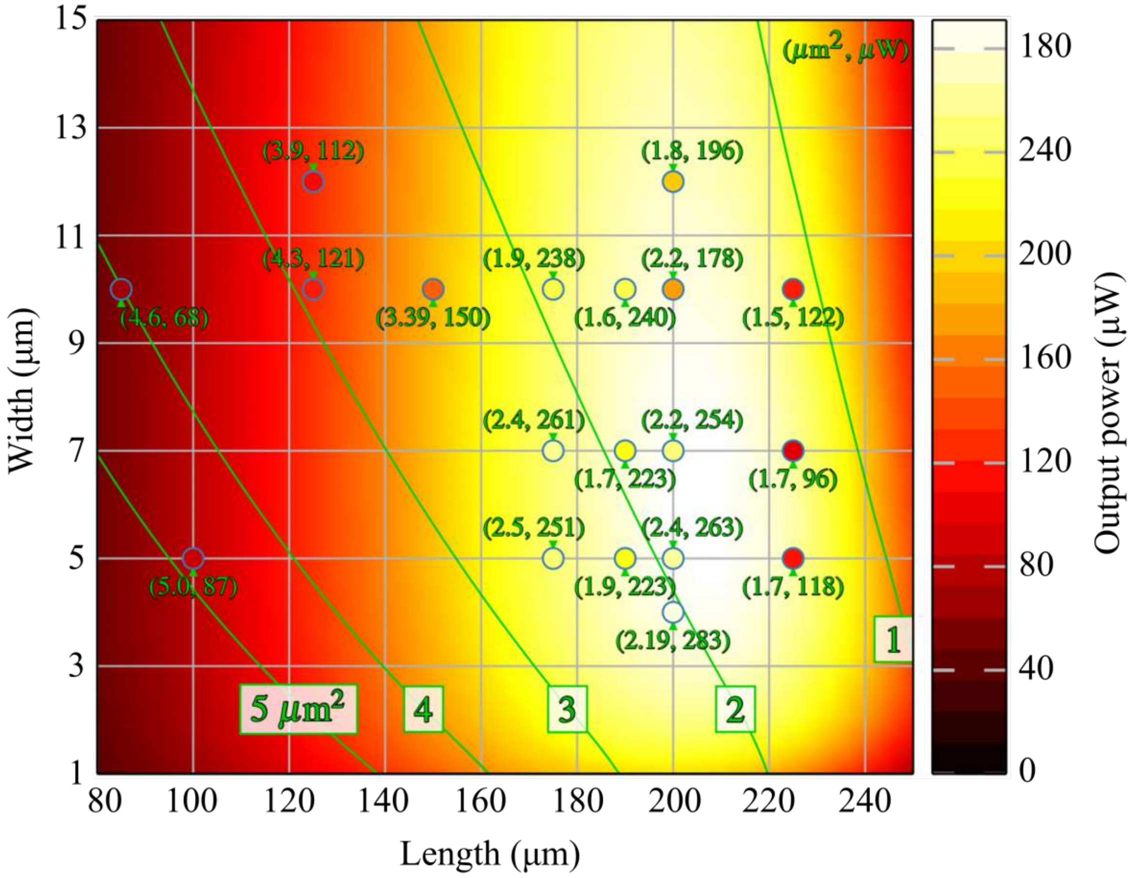

Figure 4.8: Color map of the output power of slot-antenna RTD oscillators at 185 GHz. The color-dots represent the experimental data for RTD oscillators working in the frequency range 185±10 GHz. See other notations in Fig. 4.7.

4.5 Sample fabrication and measurements

To verify the simulation predictions, we fabricated several batches of samples with different slot-antenna and RTD-mesa dimensions. The oscillator parameters in one batch were chosen to make them operate at 375 GHz. In the second batch, we chose 185 GHz as the target frequency. In the third batch for output power analysis, we fixed the slot width at 4 µm and varied the slot length and RTD-mesa area, resulting in RTD oscillators working at different frequencies. The fabrication process of all these samples was identical.

The fabrication process is based on optical lithography, except for one step. The process started with the deposition of the upper RTD-mesa electrodes: 200 nm Ti/Pd/Au. The electrodes were then used as a mask and whole areas around RTDs were wet etched ≈ 180 nm down to the n++ bottom layer, forming the RTD mesas. Then, the lower RTD-electrode

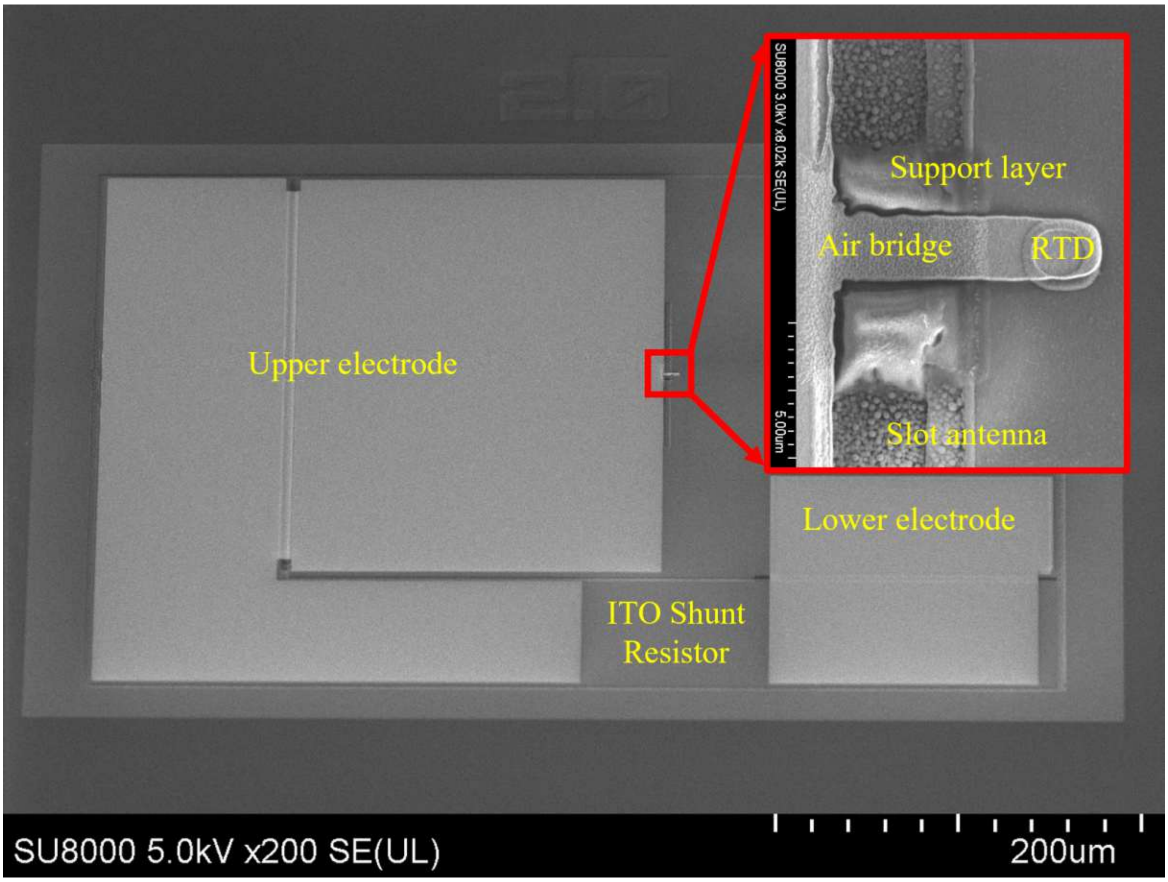

Figure 4.9: SEM image of a slot-antenna RTD oscillator with a slot length of 200 µm and width of 4 µm, the RTD mesa was 2.2 μm^2.

metallization (100 nm Ti/Pd/Au) was deposited covering the RTD, but with an opened window for the slot antenna, see schematics in Figs. 3.1 and 4.1. The offset of the RTD from the edge of the slot antenna is 3 µm in all our samples. The n++ layers in the slot and the isolation trenches surrounding the lower electrode were later removed by dry etching. Further, a 200 nm Si_3N_4 layer was deposited on the entire sample surface. It serves as a passivation layer and as a dielectric in the MIM capacitor, see Fig. 3.1. As a next step, the Si_3N_4 layer was opened at the tops of the RTD mesas using E-beam lithography. After, a photoresist layer was deposited in the slot-antenna trench next to the RTD as a support layer for the air bridge and then the last metallization layer was deposited (300 nm Ti/Au), forming the air bridge across the slot to the RTD and the upper metallization of the MIM capacitor, see an SEM image of a fabricated sample in Fig. 4.9. As a final step, an ITO shunt resistor was deposited.

The emission spectra of RTD oscillators were measured with a Martin-Puplett interferometer, which has a frequency resolution of $\approx$1 GHz and continues frequency coverage from

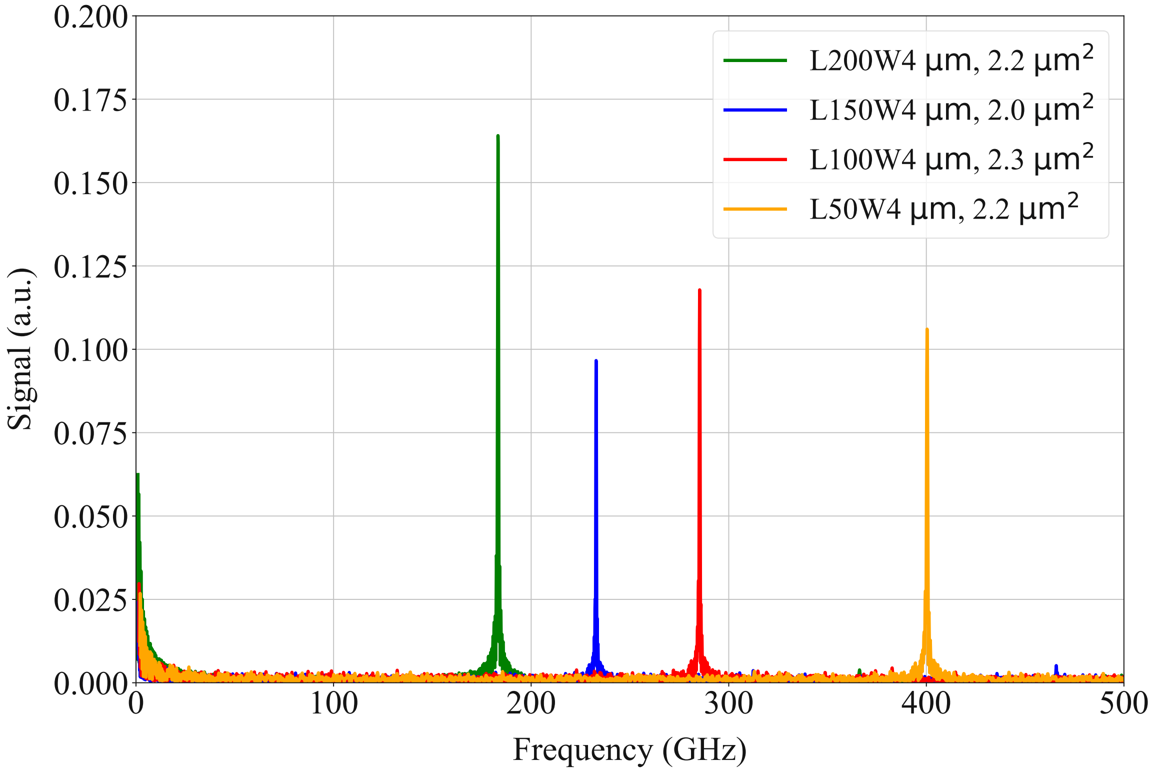

Figure 4.10: Measured frequency spectra for oscillators with antenna lengths between 50 and 200 µm, the slot width is 4 µm, and the RTD mesas for these devices were in the range 2.0-2.3 µm^2.

≈50 GHz to ≈5 THz. A Golay cell has been used as a THz detector in the interferometer. Typical measured spectra of several oscillators are shown in Fig. 4.10. All spectra are clean and do not show any parasitic lower-frequency lines, proving that the oscillators were working at the fundamental frequency.

For the output power measurements, as well as during the spectrum measurements above, the oscillator chips were placed on top of a hemispherical Si lens. The radiation of an on-chip slot-antenna oscillator is predominantly emitted into the (InP) substrate, and it is further out-coupled by the Si lens into the free space. During the output-power measurements, a calibrated pyroelectric detector was placed directly underneath the Si lens. On the way from the oscillator to the detector, 30 % of the radiation is back-reflected at the Si/air interface and further only a fraction of the radiation in the air is collected by the detector. This fraction is determined by the overlap of the slot-antenna radiation pattern and the input aperture of the detector. Our estimates based on the simulations of the antenna radiation pattern show that only ≈ 25 % of the total antenna radiation reaches the detector. Therefore, the emitted oscillator power throughout this paper corresponds to the measured detector power multiplied by a factor of 4.

4.6 Experimental data on symmetrical slot-antenna RTD oscillators

In the first batch of samples, the RTD oscillators were working at the frequencies 375±10 GHz. The slot antennas had a length in the range of 30-90 μm and a width in the range of 3-8 μm. The RTD-mesa area was adjusted accordingly to match the target frequency of 375 GHz. The measurement and simulation data for the output power of the oscillators are shown in Fig. 4.7. An oscillation frequency of 368 GHz with an output power of 82 μW was measured for a slot-antenna length and width of 90 μm and 4 μm, respectively, and an RTD area of 0.82 μm^2.

Fig. 4.8 shows similar measurement and simulation data for the second batch of samples at 185±10 GHz. The length of the slot antennas was in the range 85-225 μm and the width in the range 4-12 μm. Maximum power of 283 μW was obtained at a frequency of 184 GHz with an antenna length and width of 200 μm and 4 μm, respectively, and an RTD area of 2.2 μm^2.

Several experimental points in Fig. 4.7 are close to the theoretically-expected global maximum of the output power (slot length of ≈80-90 μm and the slot width of ≈4-6 μm). The measured output power is the highest at these points. The other experimental points are either outside the global-maximum region or close to its edge; the output power is lower at these points. A similar picture can be seen in Fig. 4.8. The points for the slot length of ≈170-200 μm and the slot width of ≈4-7 μm are close to the global maximum, and the output power is the highest for those samples. The other samples have slot dimensions closer to the edge of the global maximum and the output power is somewhat lower for those samples. However, the experimental data indicate that their maximum is shifted to slightly shorter slots compared to numerical-simulation data. Overall, the experimental data are in reasonably good agreement with the theoretical predictions. We attribute the deviations and certain scattering of the experimental data to the uncontrollable variations of the fabricated samples due to the limitations of the optical lithography used in this study.

The above analysis indicates that an optimum slot-antenna width in the 150-400 GHz frequency range is close to 4 μm. Therefore, as a next step, we fabricated a third batch of RTD oscillators with a slot width of 4 μm and slot lengths of 50 μm, 100 μm, 150 μm, and 200 μm with different RTD-mesa areas. The output power of these samples is shown in Fig. 4.11. For each given antenna length, when the RTD area is small, the oscillation frequency is the highest, but the output power is not at the maximum since RTD is small.

Table 4.1: Output power for different types of RTD oscillators.

References	**Frequency** GHz	**Power** μW	**Oscillator type**
This work	184	283	Sym. slot
	368	82	Sym. slot
[57]	90	500	Sym. slot
[57]	110	376	Sym. slot
[105]	342	23	Sym. slot
[119]	425	10	Sym. slot
[121]	520	50	Sym. slot
[120]	1250	30	Sym. slot
[8]	260	1000	CPW resonator
[98]	330	70	Patch
[107]	354	31	Slot ring
[100]	405	60	Slot + Vivaldi
[6]	450	320	Patch
[10]	548	420	Asym. slot
[2]	660	27	Patch
[127]	730	131	Cavity resonator
[7]	1040	36	Slot + Yagi-Uda
[2]	1090	9	Patch
[6]	450	11800	Patch array
[11]	530	770	Asym.-slot array
[10]	620	610	Asym.-slot array
[11]	630	87	Sym.-slot array
[128]	675	47	CPW array + dipole
[11]	700	300	Asym.-slot array

When RTD is large, then the frequency is the lowest; still, the output power is getting low again since the radiation conductance of the slot antenna is getting low when the slot antenna is operated much below its eigenfrequency. In between, for some middle values of the RTD area, the oscillator's output power reaches a maximum at some intermediate frequencies. The experimental data and the theoretical output-power curves in Fig. 4.11 follow this qualitative behavior. The figure includes additionally several data points corresponding to the samples with the highest output power from the first two batches of devices with frequencies near 185 GHz and 375 GHz.

The output power of our RTD oscillators in Fig. 4.11 is very close to the best symmetrical-slot-antenna RTD oscillators reported in the literature. A set of representative literature data for the symmetrical-slot-antenna RTD oscillators is shown in Fig. 4.11 and in Tab. 4.1. High output power in our oscillators was achieved due to two reasons. First, the slot-antenna parameters are close to the optimum in our oscillators. Second, due to a small value of τ_{RTD} in our RTDs, which allows one to reduce γ (see Eq. (4.3)), and since our RTDs have a sufficiently large value of the non-linearity parameter $\alpha(\gamma)$ at small γ. As a result, that leads to large values of the output power, given by Eq. (4.1). For more details about the calculation, see Ref. [Tuan1][IMPACT OF SLOT WIDTH...](submitted, under review).

$$P = \frac{1}{2} G_{\mathrm{r}} \Delta V^2 (1-\gamma)\, \alpha(\gamma), \tag{4.1}$$

where

$$V_{\mathrm{AC}}^2 = \Delta V^2 (1-\gamma)\, \alpha(\gamma), \tag{4.2}$$

$$\gamma = \omega \tau_{\mathrm{RTD}} \frac{G_{\mathrm{r}} + G_{\mathrm{l}}}{B_{\mathrm{a}}}, \tag{4.3}$$

We should stress, that this study is limited to symmetrical-slot-antenna RTD oscillators: RTD oscillators with asymmetrical slot antennas [10] and other types of RTD oscillators do provide even higher output powers. For comparison, Tab. 4.1 shows representative literature data for diverse RTD oscillators: with coplanar-waveguide (CPW) resonators, patch and slot-ring antennas, additional radiators (e.g., Vivaldi or Yagi-Uda antennas), coherent arrays, etc. Different RTD-oscillator types have their advantages and disadvantages, but symmetrical-slot-antenna RTD oscillators stand out due to their simplicity and symmetrical radiation pattern. As such, they still keep their niche in the ongoing investigation and development of RTD oscillators, particularly as a building block in the more complicated and array designs of RTD oscillators [11], [13].

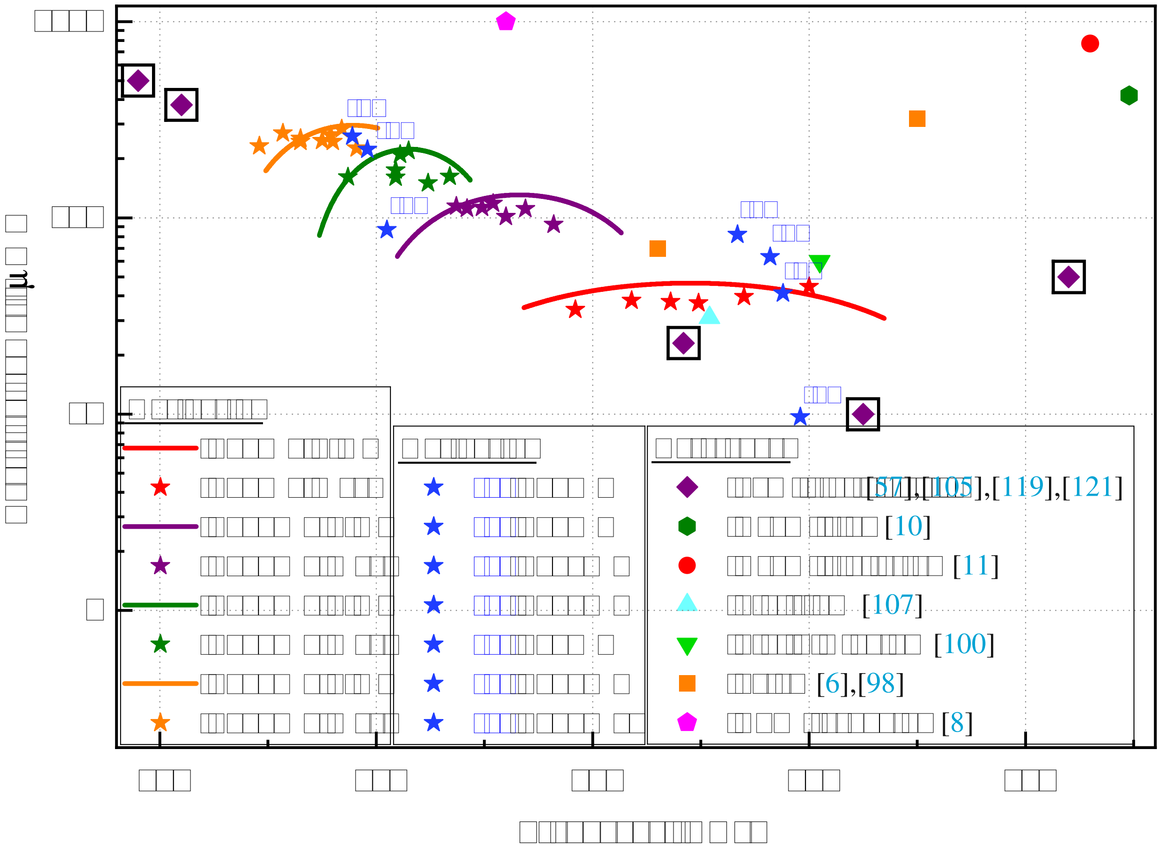

Figure 4.11: Radiated power vs. oscillation frequency of the fabricated slot antenna RTD oscillators. In this device batch, the slot antenna length was set to 50 µm, 100 µm, 150 µm, and 200 µm, with a constant width of 4 µm. The RTD areas ranged from 2.0 μm^2 to 5.0 μm^2. The solid lines show simulated output power, and the star points indicate the measured ones. Additionally, several data points with a high level of output power from the other two batches of samples (see Figs. 4.7 and 4.8) are also shown. For comparison, we show the literature data on symmetrical-slot-antenna RTD oscillators and a few characteristic data points for the other types of RTD oscillators.

4.7 Conclusion

We show that the output power of symmetrical-slot-antenna RTD oscillators depends on the slot width and that the slot width is an important degree of freedom for fine tuning the slot geometry in the RTD oscillators. Our data also indicate that the commonly used 4 µm slot width is close to an optimal slot-parameter range, corresponding to the global output-power maximum, at least in the sub-THz frequency range. This is confirmed both by our theoretical and experimental data.

4. Impact of Slot Width on Performance of Symmetrical-Slot-Antenna Resonant-Tunneling-Diode Oscillators

We present an extensive set of experimental data on RTD oscillators with different slot widths. The data reasonably agree with the theoretical analysis and support its validity. Some oscillators exhibit the output-power level close to the state-of-the-art for fundamental-frequency symmetrical-slot-antenna RTD oscillators in the frequency range of 150-400 GHz. Specifically, we report 283 μW at 184 GHz and 82 μW at 368 GHz.

Chapter 5

Island THz on-chip slot-antenna resonant-tunneling-diode oscillators

Results shown in this chapter were published in the peer-reviewed journal article **D. Tuan Nguyen**, P. Ourednik, and M. Feiginov, "Island THz on-chip slot-antenna resonant-tunneling-diode oscillators," *Applied Physics Letters*, and **D. Tuan Nguyen**, P. Ourednik, and M. Feiginov, "Conventional vs. island THz slot-antenna resonant-tunneling-diode oscillators," *Conf. Infrared, Millimeter, and Terahertz Waves (IRMMW-THz), 2023.*

5.1 Introduction

Slot-antenna RTD oscillators are good candidate for THz frequency applications.[3],[4] The frequencies up to almost 2 THz was achieved with this type of RTD oscillators.[9]. However, to achieve higher frequencies and improve the performance of RTD oscillators in the THz range, one needs to reduce the oscillator losses.[3],[4] The losses of the RTD oscillators have two main sources. One is related to the parasitics of the RTD itself. The main contribution to parasitics comes from the RTD contact resistance, which is nowadays in the range of 1-3 $\Omega\,\mu\mathrm{m}^2$ in good RTDs, and there is not much one can do to improve it further. The other source of losses is in the resonator/antenna of an RTD oscillator. A few concepts are being discussed on how to radically minimize those losses by switching to unconventional resonator concepts.[129],[130] However, they still need to be demonstrated to be advantageous in practice. In this work, our primary concern is optimizing the design of the most basic and simple slot-antenna RTD oscillators. Only such oscillators have been demonstrated to work at fundamental frequencies above or around 1.5 THz so far.[9], [95], [96], [97], [121]

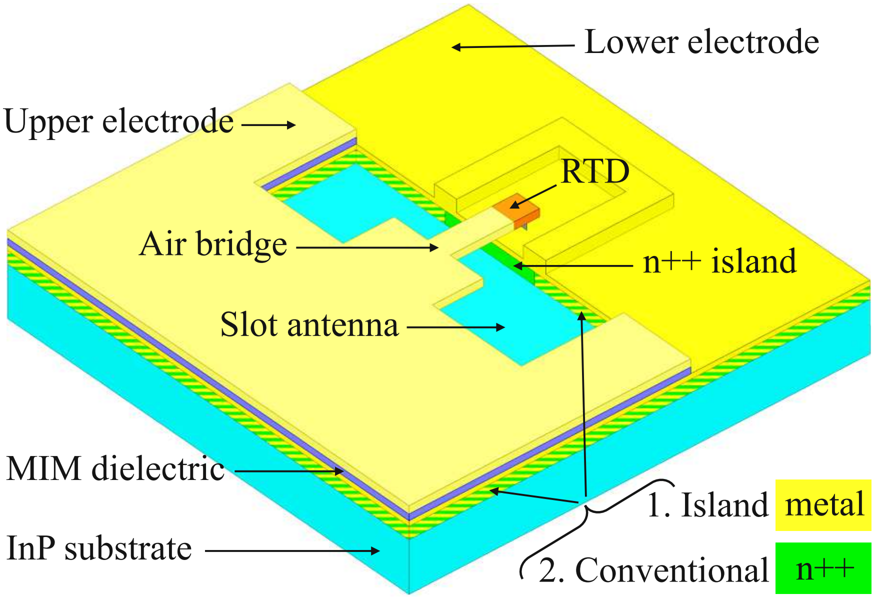

Figure 5.1: Schematic of an island/conventional slot-antenna RTD oscillator. In the island design, the n++ InGaAs layer (except for n++ island) was replaced by metal (Au).

In this study, we demonstrate an "island" design of on-chip slot-antenna resonant-tunneling-diode (RTD) oscillators, where the contact n++ layer is removed everywhere except for a small island under the RTD. At frequencies around 2 THz, this design leads to a significant reduction (by a factor of ≈ 2) of the total ohmic losses at the conducting surfaces of the slot antenna. With this design, we achieve the highest radiated power for RTD oscillators in the frequency range 1.6-1.74 THz with around 2.2 µW at the fundamental frequency of 1.74 THz. Theoretical analysis of the oscillators indicates that with the used RTD design, the operating frequencies beyond 2 THz should be reached if the RTD contact resistance is reduced to 1-1.5 $\Omega\,\mu\mathrm{m}^2$.

5.2 Design of island slot-antenna RTD oscillators

The design of a slot-antenna oscillator we investigated in this study is sketched in Fig. 5.1. It contains a slot antenna on a semiconductor substrate; almost all its radiation is emitted into the substrate. An air bridge connects RTD across the slot to a metal-insulator-metal (MIM) capacitor on the other side. The design of the island slot-antenna RTD oscillator was done by changing the concept of a conventional slot-antenna RTD oscillator. In the island design, the n++ InGaAs layer was left only as a small contact patch/island directly under the RTD as its bottom contact and removed everywhere else, see Fig. 5.1. Such design has been used in the past in the membrane slot-antenna RTD oscillators,[5] but it has not been applied to slot-antenna RTD oscillators on substrates, and the impact of the island design on the oscillator losses has not been quantitatively analyzed.

To have a clear picture about the advantages of the island slot-antenna RTD oscillator over the conventional one, we will study the loss mechanism of these two slot-antenna designs in the next section.

5.3 Loss resistance of a slot antenna

This section examine the total loss resistance and its constituent parts of the conventional and the island slot antennas at frequency of 2 THz. Except for the desirable radiation losses, such oscillators are subject to the ohmic losses at the outer metal surfaces, in the MIM (due to surface currents at the inner sides of the metal layers sandwiching the MIM dielectric), in the highly-doped semiconductor layer (n++ RTD contact layer), and in the air bridge. Among these losses, the ones in the n++ layer and at the outer metal surfaces are the largest loss contributions.

The slot antennas in RTD oscillators are usually small compared to the wavelength of the radiated waves.[9, 45, 95, 96], [97, 3, 4], [121] Consequently, these slot antennas work in the inductive regime with a dominant magnetic field. Additionally, the antennas usually have low losses, i.e., their inductive reactance is large compared to their total loss resistance. In this case, the slot inductance, the distribution of the magnetic field around the slot, and the distribution of the currents flowing around the slot circumference are determined solely by the geometry of the conducting layers composing the slot antenna (as if the layers were ideally conducting). If a metal layer of the slot is significantly thicker than its skin depth, then the slot currents are localized as surface currents at the top and bottom sides of the slot conducting layers. In the conventional slot-antenna design, the bottom conducting layer is an n++ layer everywhere underneath the slot lower-electrode (LE) metallization. If the n++ thickness is large or comparable to the n++ skin depth (that happens at THz frequencies and, in particular, close to 2 THz), then the surface currents flow to a large extent within the skin depth at the bottom surface of the n++ layer.

Further, we note that the strength of the surface currents is determined by the strength of the magnetic field at the conducting surfaces. Since the slot is nearly flat, thin, and embedded into a non-magnetic antenna environment, the magnetic field of the slot should be nearly identical at the top and bottom sides of the slot plane. Consequently, the surface currents' strength and distribution should also be nearly identical at the top and the bottom of the

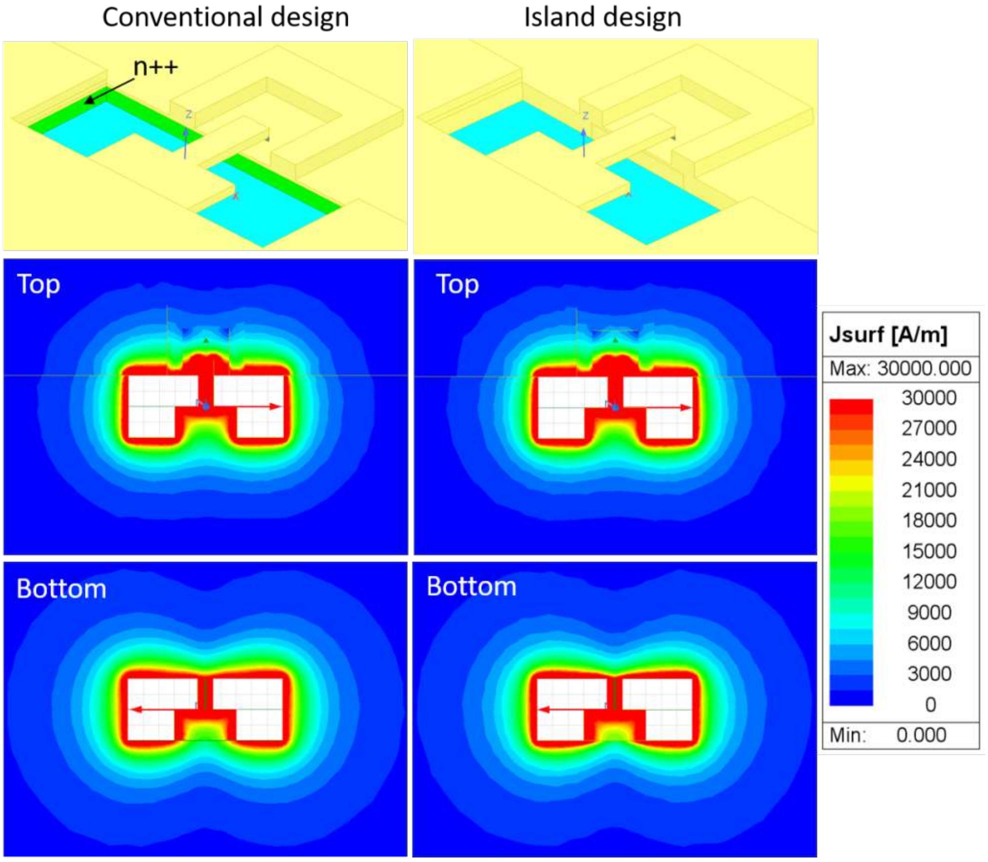

Figure 5.2: Surface currents at the top and bottom surfaces of a slot antenna with both conventional (with n++ layer) and island (no n++ layer) designs at 2 THz. For clarity, we sketch slot antennas with a single-layer metallization without MIM.

slot conducting layers. This is where the problem with the conventional design of the slot antennas lies: one-half of the total antenna current (at the antenna bottom side) flows at the surface of a highly-resistive n++ layer. That creates excessive ohmic losses.

To illustrate the loss mechanism in the n++ layer in more detail, Fig. 5.2 shows the surface-current distribution at the top and bottom sides of conventional (with n++ layer) and island designs of the slot-antenna RTD oscillators. LE of the conventional design is composed of two layers: 500 nm n++ and 100 nm gold. In the island design, the n++ layer was replaced by gold. For clarity of these simplified simulations, we excluded MIM (its dielectric is replaced by gold) and also replaced the n++ island with gold in the island-design simulation. To illustrate the situation, when the skin depth is small compared to the layer thicknesses, we calculated only the surface currents in Fig. 5.2. The slot length and width were taken as 10 µm and 4 µm, respectively, and the calculations were done at the frequency of 2 THz. Fig. 5.2 shows that the level and distributions of the surface currents around the slot antenna are almost identical in conventional and island designs. The top and bottom surface currents are very similar in both cases, in agreement with the qualitative arguments above. The surface-current power loss is proportional to the skin-layer resistance, which is proportional to $\sqrt{\sigma}$, where σ is the material conductance. Since the gold conductance is ≈ 40 times higher than the conductance of n++ (see later the specification of n++ in our design), the loss power and resistances are ≈ 6 times higher in the n++ layer than in gold for the same surface current. That leads us to a straightforward comparative assessment of the surface-current losses in both cases. Denoting as P_0 the power loss at the top (gold) surface, we can write the total surface loss for the island design as $P_{\mathrm{Surf}}^{\mathrm{Isl}} \approx 2P_0$, accounting for both the bottom and top surfaces. In the conventional design with the n++ layer, the surface loss can be approximated as $P_{\mathrm{Surf}}^{\mathrm{Conv}} \approx P_0 + 6P_0 \approx 7P_0$, i.e., the surface resistance in the conventional design is ≈ 3.5 times higher than that in the island design. The actual difference between these two designs is not at this extreme level (since the skin depth in n++ is not much smaller, but only comparable to the layer thickness at 2 THz). Still, it is very significant indeed, as it will be shown below.

To analyze the loss mechanisms in the fabricated samples, we plotted the total loss resistance (R_{Ant}) for the island-design (see Fig. 5.1) slot antenna and its constituting parts: outer-surface-current (R_{Surf}), radiation (R_{Rad}), MIM (R_{MIM}), and bridge (R_{Bridge}) resistances, see Fig. 5.3. The calculations were done for lower- and upper-electrode thicknesses of 600 nm (100 nm from the original LE thickness as in the conventional design, and another 500 nm by replacing InGaAs n++ layer) and 300 nm, respectively, and with 150-nm thick Si_3N_4 as MIM dielectric, see notations in Fig. 5.1. For comparison, we showed the loss resistances for conventional (but otherwise identical) design, where the LE was 100 nm gold layer lying on top on 500 nm thick InGaAs n++ layer with the doping of 5×10^{19} cm^{-3}. At 2 THz, the skin depth in the n++ layer is approximately 500 nm, which is comparable to the layer thickness (in these simulations, we took into account the volume distribution of the current inside the n++ layer); the skin depth in the evaporated gold at 2 THz is 80 nm, which is smaller than or comparable to the thicknesses of the metal layers. One can see in Fig. 5.3 that the main loss contribution originates from the outer surface currents. This contribution is strongly (by almost factor 2) reduced by the island design compared to the conventional one, as expected from the qualitative considerations above.

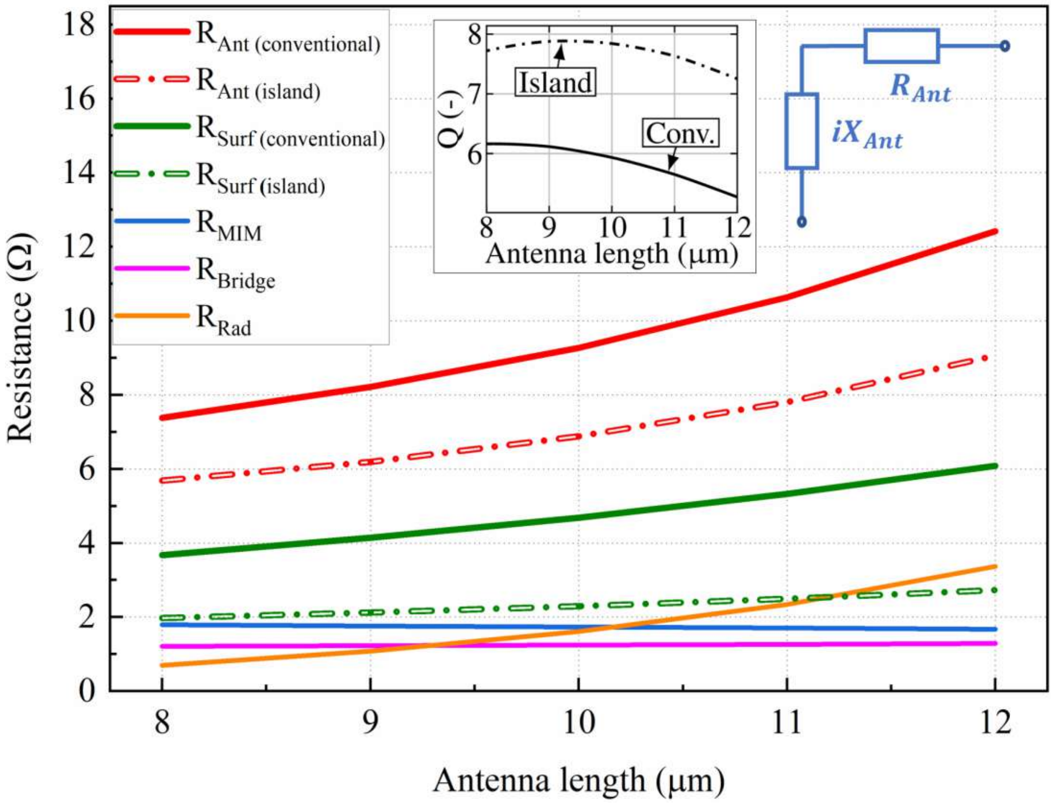

Figure 5.3: The total loss resistance and its constituent parts at 2 THz for slot antennas with different lengths. The simulation data for the island and conventional designs are shown. The antenna impedance was represented as a serial connection of the antenna reactance (X_{Ant}) and loss resistance (R_{Ant}), as indicated by a schematic in the figure. For both cases, the antenna Q factor, defined as $X_{\mathrm{Ant}}/R_{\mathrm{Ant}}$, is also shown as an inset.

5.4 1.0 nm RTD parameters

In this work, we used an RTD-wafer design with a high current density of 23.6 mA/µm^2 and a particularly high peak-to-valley current ratio of 3.7 (see RTD I-V curve in Fig. 5.5). The RTD design was used in double-RTD patch oscillators at ≈ 1.1 THz.[2] The RTD layers were grown on a semi-insulating InP substrate and had nominally 1.0 nm AlAs barriers sandwiching a composite $In_{0.53}Ga_{0.47}As/InAs/In_{0.53}Ga_{0.47}As$ quantum well with the nominal thickness of each sublayer of 1.1 nm. On the emitter side of RTDs, we incorporated a 25 nm long $In_{0.53}Ga_{0.37}Al_{0.1}As$ step emitter[45] with the n-doping of 3×10^{18} cm^{-3}, the collector side contained a 12 nm undoped $In_{0.53}Ga_{0.47}As$ spacer. The other layers surrounding the above barrier region on both sides were $In_{0.53}Ga_{0.47}As$ layers with the n++ doping of 5×10^{19} cm^{-3}, see more details in Fig. 5.4.

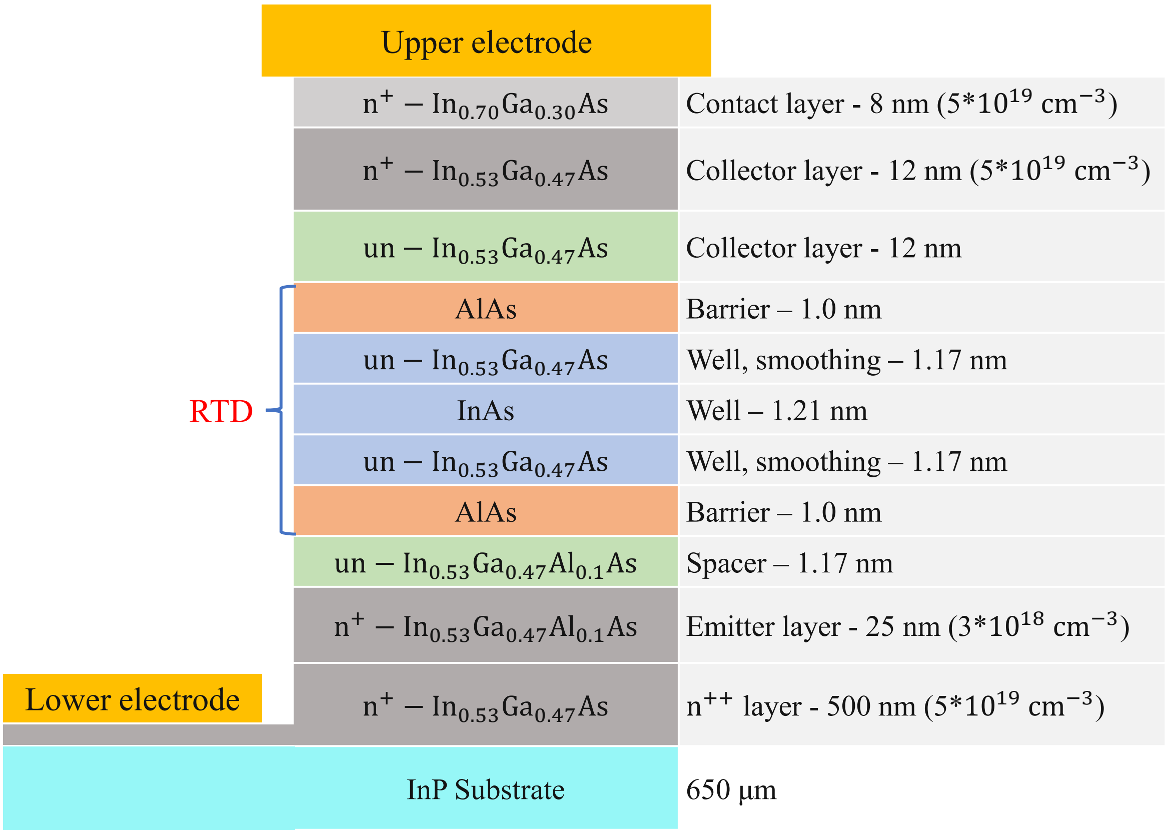

Figure 5.4: Layer stack of 1.0 nm RTD wafer.

Figure 5.5 shows the I-V characteristics of 1.0 nm barrier RTD with an area of 0.2 μm^2. All the curves are normalized to the value of the current density of the RTD which is $\approx$ 23.6 mA/μm^2. The theoretical I-V curve is shown in red color. The blue curve shows the experiment data of the RTD before the ITO shunt resistor deposition, and the green one is the data in the oscillation mode after subtraction the ITO shunt resistance.

Based on the simulation analysis in the chapter 2, we calculate the small-signal RTD conductance g_{SS}, capacitance c_{SS} dependence on applied voltage V_{DC}, also the RTD conductance g_{RTD} and capacitance c_{RTD} on the AC voltage amplitude V_{AC}. Figure 5.6 shows $g_{SS}(V_{DC})$ in the quasi-static regime and at the frequencies of 1.0 THz and 2.0 THz. The maximum of the static NDC is achieved at the DC bias of 0.57 V. The variation of $g_{RTD}(\omega, V_{AC})$ at V_{DC}=0.57 V with V_{AC} in the quasi-static regime and at several frequencies is shown in Fig. 5.7; the plots are calculated with Eq. (2.15). Fig. 5.8 shows SS RTD capacitance ($c_{SS}(V_{DC})$) calculated with Eq. (2.17) at several frequencies. Fig. 5.9 illustrates variation of $c_{RTD}(\omega, V_{AC})$ with V_{AC} calculated with Eq. (2.16), V_{DC} was taken equal to 0.57 V. In this work, the analysis of the

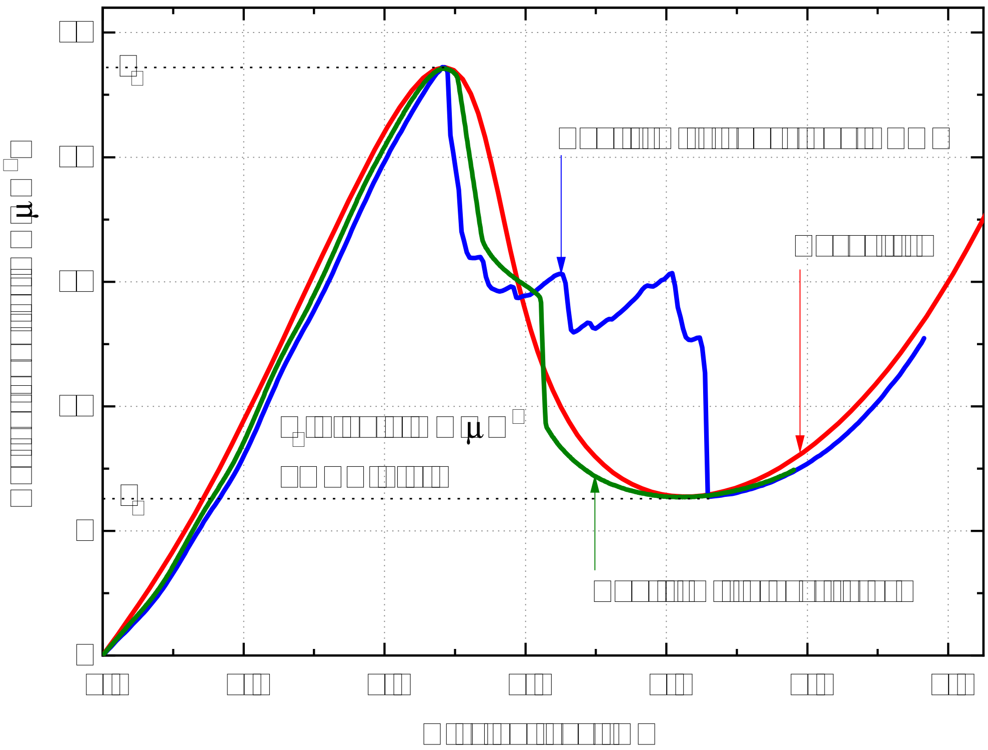

Figure 5.5: IV characteristics of 1.0 nm barrier RTD. The red curve shows the theoretical IV curve. The blue and green ones show the experiment IV curves of a stand-alone and in oscillator RTD mesas, respectively.

oscillation frequencies and oscillator output power was performed assuming that the RTD is operated at V_{DC}=0.57 V, where NDC has a maximum.

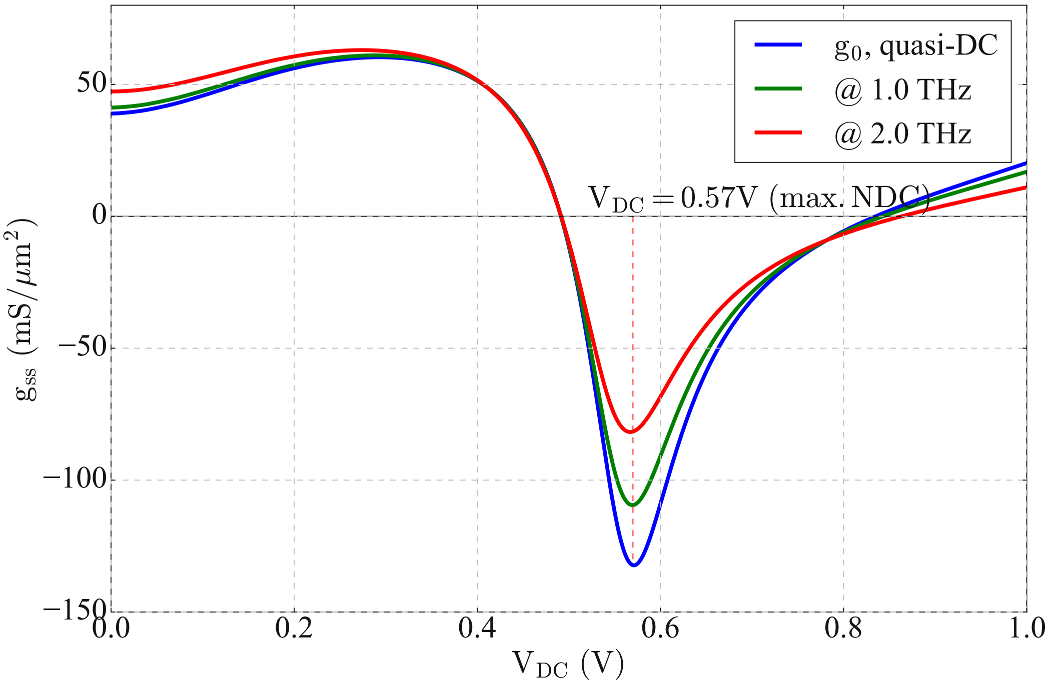

Figure 5.6: Dependence of the small-signal RTD conductance on the bias voltage, $g_{SS}(V_{DC})$, in the quasi-DC case and at several frequencies.

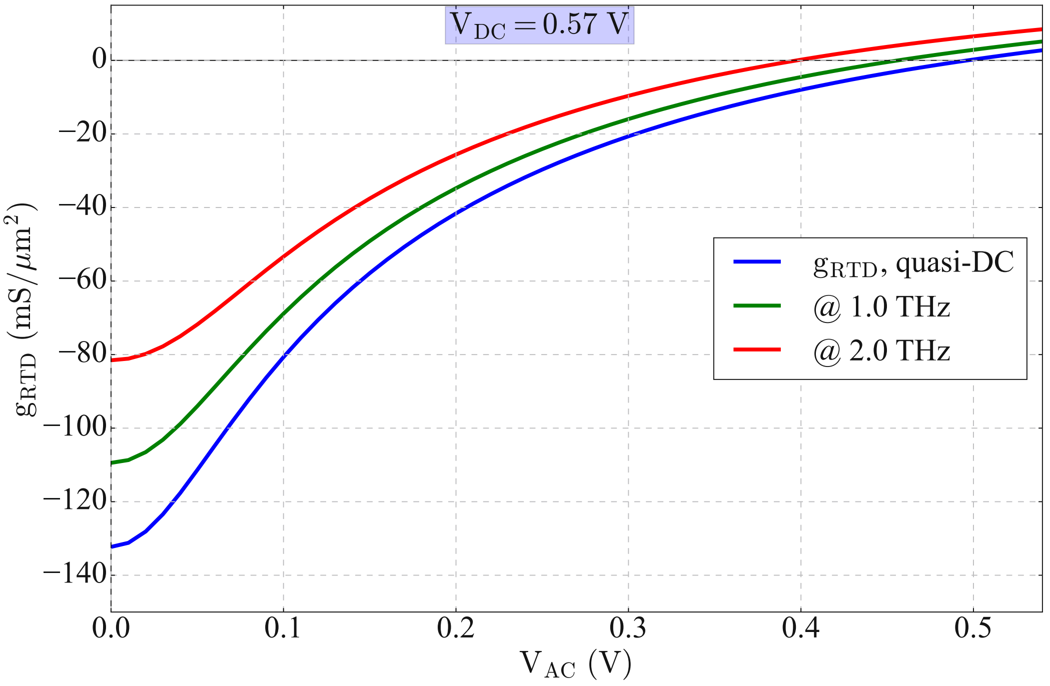

Figure 5.7: Dependence of the RTD conductance on the AC voltage amplitude, $g_{RTD}(V_{AC})$, at V_{DC}=0.57 V in the quasi-DC case and at several frequencies.

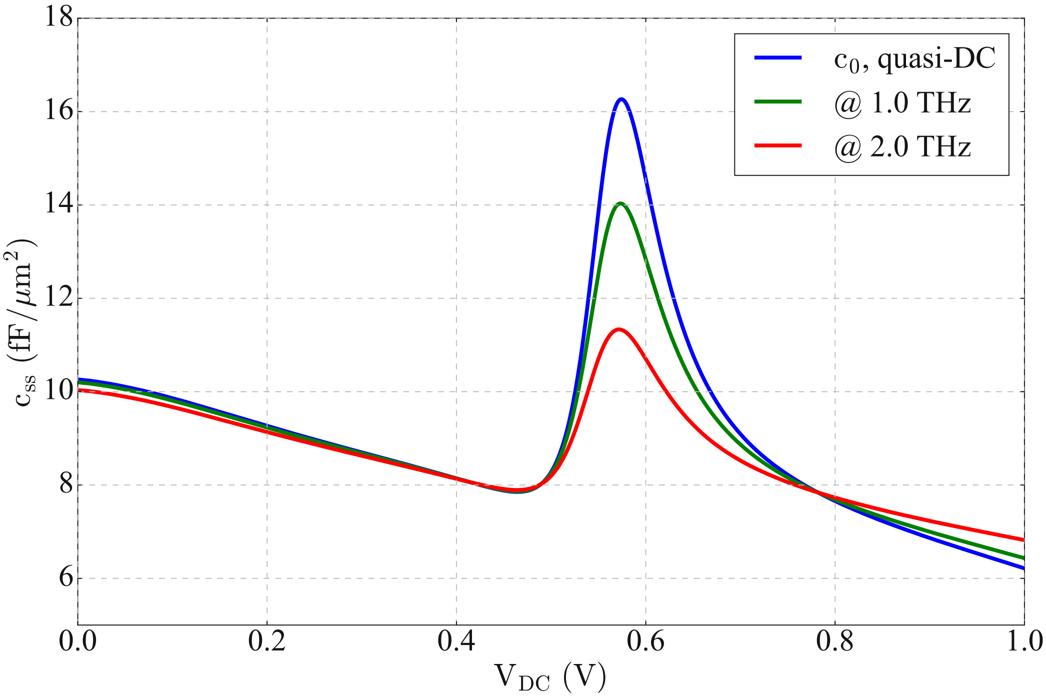

Figure 5.8: Dependence of the small-signal RTD capacitance on the bias voltage, $c_{SS}(V_{DC})$, in the quasi-DC case and at several frequencies.

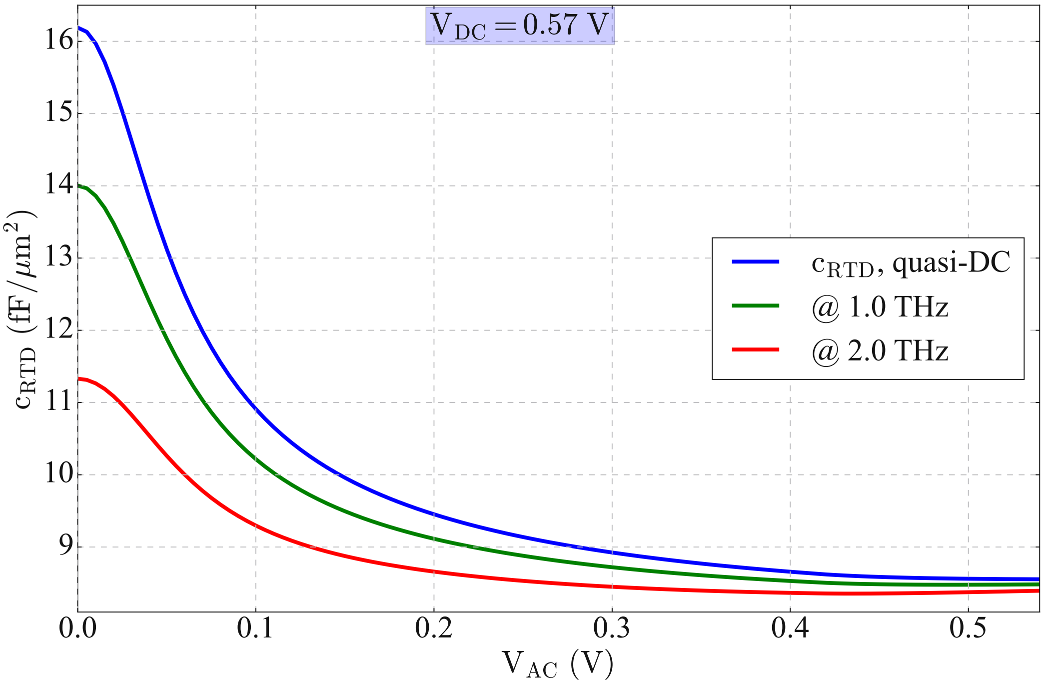

Figure 5.9: Dependence of the RTD capacitance on the AC voltage amplitude, $c_{RTD}(V_{AC})$, at V_{DC}=0.57 V in the quasi-DC case and at several frequencies.

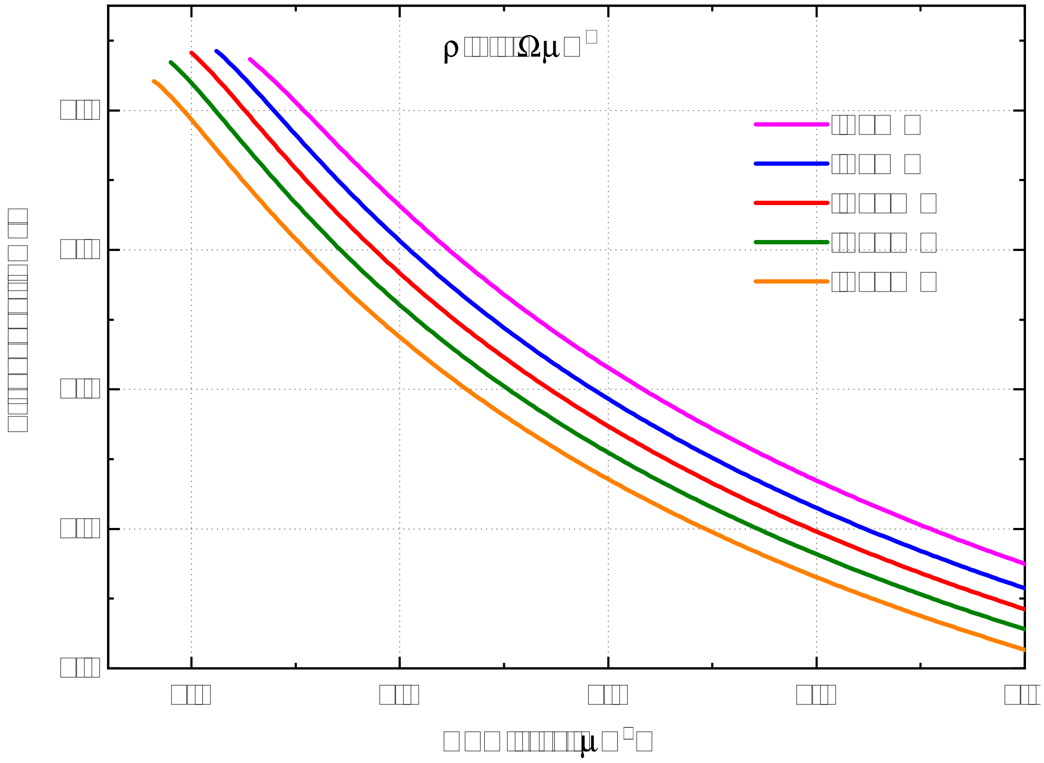

Figure 5.10: Simulated oscillation frequencies of slot antennas with slot lengths from 8 µm to 12 µm and with a contact resistance of 2 Ω µm^2.

5.5 Numerical simulations

The island design of the slot-antenna RTD oscillator was optimized for operation close to 2 THz with the above-mentioned RTD wafer. Fig 5.10 shows the operating frequencies of the oscillators with slots of 4 µm width and lengths from 8 µm to 12 µm. With the increase of the antenna length, the radiation losses increase; when the antenna becomes too short, its total losses get too high. Therefore, an optimal antenna length exists; it roughly corresponds to the maximum of the antenna Q factor shown in the inset in Fig. 5.3. The theoretical curves in Fig. 5.10 shows that the highest frequencies should be achievable with 9 µm and 10 µm long slot antennas, which were chosen for fabrication.

We also show the dependence of the oscillation frequencies on the contact resistance for the slot antenna with 10 µm length and 4 µm width in Fig. 5.11. The frequency above 2 THz can be achieved with this type of RTD oscillators if the RTD contact resistance is reduced to 1-1.5 Ωµm^2.

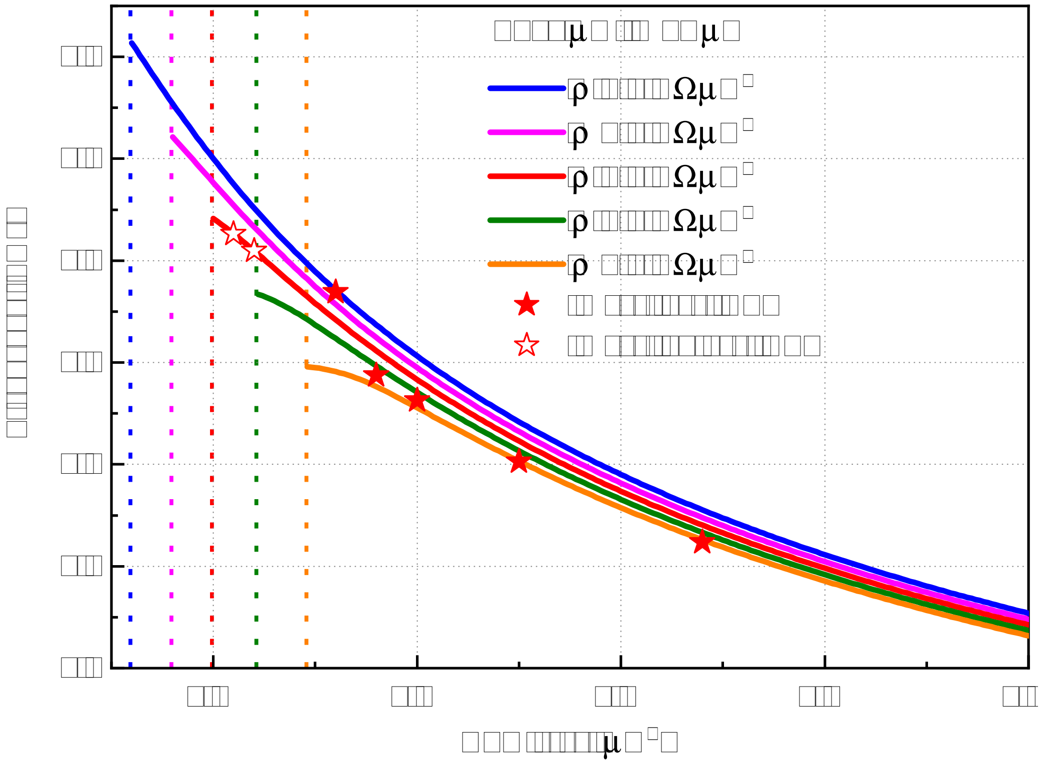

Figure 5.11: Fundamental slot-antenna oscillator frequencies vs. RTD area for the slot length of 10 µm and the width of 4 µm. The theoretical curves are calculated assuming the RTD contact resistance of 1 Ω µm^2, 1.5 Ω µm^2, 2 Ω µm^2, 2.5 Ω µm^2, and 3 Ω µm^2. The continuous lines show the theoretical curves, the dotted lines indicate the upper frequency bound in each case, the filled stars show the measurement data, and the empty stars show the expected frequencies for devices that were not oscillating.

5.6 Sample fabrication and measurement

This section describes the fabrication processes of the island slot-antenna RTD oscillator and the measurement setup. The general processes of the sample fabrication were described in Chapter 3. In this section, we introduce only the main features and the differences in the fabrication procedures of the island design.

The fabrication process of the island slot-antenna RTD oscillators was based on optical lithography except for two electron-beam-lithography (EBL) steps of patterning RTD mesas and opening SiN on RTD mesas . The fabrication started with RTD-mesa EBL patterning, followed by deposition of 180 nm thick (Ti/Au) upper RTD-mesa contact metallization.

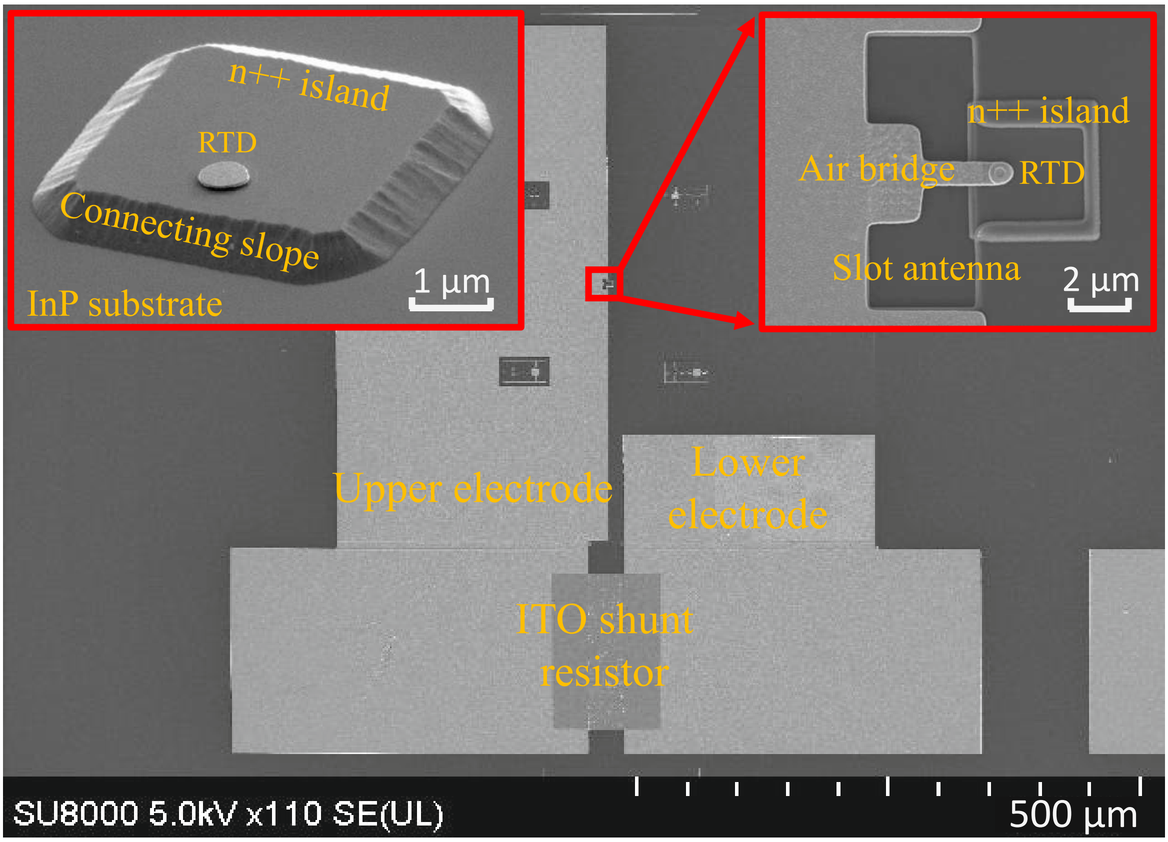

Figure 5.12: SEM image of an island slot-antenna RTD oscillator with 10 µm slot length and 0.16 μm^2 RTD-mesa area. RTD offset from the slot edge is ≈ 1 µm. The left inset shows the island before the deposition of the LE metallization. The island dimensions are $\approx 4 \times 4$ μm^2.

In the conventional slot-antenna RTD oscillator design, the lower electrode (LE) should be formed as the next step. However, the situation is different for the island design as the n++ InGaAs island must be created before LE. The n++ island is formed as followings: an island with a radius of ≈ 2 µm around the RTD mesa was covered by a photoresist, followed by dry etching in RIE for ≈ 300 nm and then subsequent wet etching of the remaining n++ InGaAs layer to guarantee soft slopes at the edges of the island, see Fig. 5.12. Having soft slopes for the island is crucial to avoid any cracks at the edges of the island for the LE metal deposition later. Using pure dry etching or pure wet etching to form the island is not a good choice as the slopes cannot be formed or are too large (the offset between the RTD mesa and the edge of the slot antenna will be increased leading to an increase of the parasitic capacitance), and that is why we use both dry and wet etching for this purpose.

Next, the photoresist was removed from the island, and the RTD mesas were wet etched through the RTD layers until the bottom n++ layer on the island was exposed. In the next step, the slots were covered by a photoresist, and the RTD LE metallization was evaporated with a thickness of around 90 nm (Ti/Au). The formation of the LE was completed by depositing an additional 400 nm of Ti/Au everywhere on top of the first LE metal layer, except for the central part of the island; see Fig. 5.12 and schematic in Fig. 5.1.

Further, the whole chip surface (also RTD mesas) was covered by 150 nm SiN as the MIM dielectric. The sample was then patterned with EBL to open holes in SiN at the top of the RTD mesas. Afterward, a photoresist planarization layer was deposited as a support layer for the air bridge. Then, the upper electrode (300 nm of Ti/Au) was evaporated, forming the air bridge, the upper metallization of the MIM, and an upper RTD contact. As a final step, the ITO shunt resistor (to suppress low-frequency instability of the RTD oscillators) was deposited outside the slot-antenna area; see the completed oscillator in Fig. 5.12.

5.7 Experimental data on island slot-antenna RTD oscillators

The RTD-mesa areas of fabricated oscillators were in the range from 0.11 μm^2 to 0.37 μm^2. The areas were determined by normalizing the RTD-peak currents on the RTD current density. The characteristic measured spectra of several oscillators are shown in Fig. 5.13. The spectra were measured with a Martin–Puplett interferometer, covering the frequency range from $\approx$ 50 GHz up to $\approx$ 5 THz with the resolution of $\approx$ 1 GHz; Golay cell has been used as a detector. The spectra were clean and showed no indications of sub-harmonic lines, proving that the measured spectral lines correspond to the fundamental frequencies of the oscillators.

The oscillators with the slot length of 10 μm were working in the frequency range 1.2-1.74 THz for the RTD areas of 0.16-0.34 μm^2 and the oscillators with 9 μm long slots were working at frequencies 1.2-1.72 THz for the RTD areas of 0.17-0.37 μm^2. These oscillators' operating frequencies agree with the theoretical calculation results shown in Fig. 5.11. The oscillators with the smaller RTD areas were not oscillating, or their output power was not measurable. Fig. 5.11 also shows the expected frequencies of the devices, which were not oscillating. To match the theoretical and experimental data on the upper bound for the oscillating frequency of our oscillators, we assume that the contact resistance of our RTDs is $\approx 2\,\Omega\,\mu m^2$. This number is in agreement with the transfer-length-method (TLM) measurements of the contact resistance on test samples, which was typically in the range $\approx$ 1-2 $\Omega\,\mu m^2$. Fig. 5.11 shows that with a decrease of the contact resistance to 1-1.5 $\Omega\,\mu m^2$, the oscillation frequencies above 2 THz should be achievable with the presented RTD and island slot-antenna design.

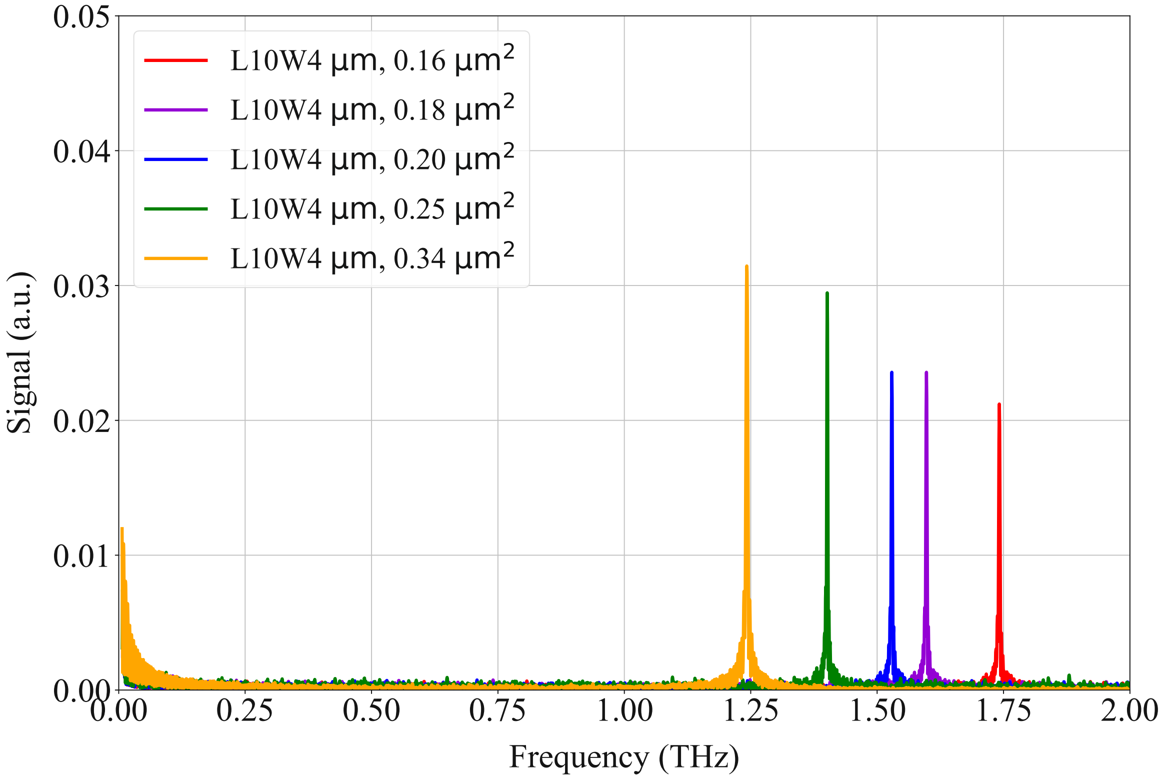

Figure 5.13: Measured frequency spectra for oscillators with the island slot-antenna length and width of 10 μm and 4 μm, respectively. Experimental (0.2 μm^2 RTD) and theoretical RTD I-V curves are shown in the inset.

The methodology of the theoretical analysis of the operating frequencies of RTD oscillators, their output power, and losses is based on the theory described in Refs. [110–112], [57], [125] and was previously applied to the analysis of RTD oscillators in Refs. [2], [5], [57], [98], [124], [125].

Figure. 5.14 illustrates an increase in the island's design oscillation frequency compared to the conventional one for the given RTD wafer. For comparison, we present the improvement of the oscillation frequency if the conventional design had been made with thicker LE (an additional metallization layer on top of the slot), as in Ref. [9]. However, the best performance should be achieved if both the thick-electrode concept (not compatible with our technology so far) of Ref. [9] and our island design are implemented simultaneously in one slot-antenna RTD oscillator, see the orange line in Fig. 5.14. With further increase of the RTD current density and/or reduction of the RTD contact resistance, the oscillation frequencies significantly above 2 THz should be achievable.

The output power of the oscillators was measured by mounting a calibrated pyroelectric detector right after a hemispherical Si lens with the oscillator chip on it. The measured

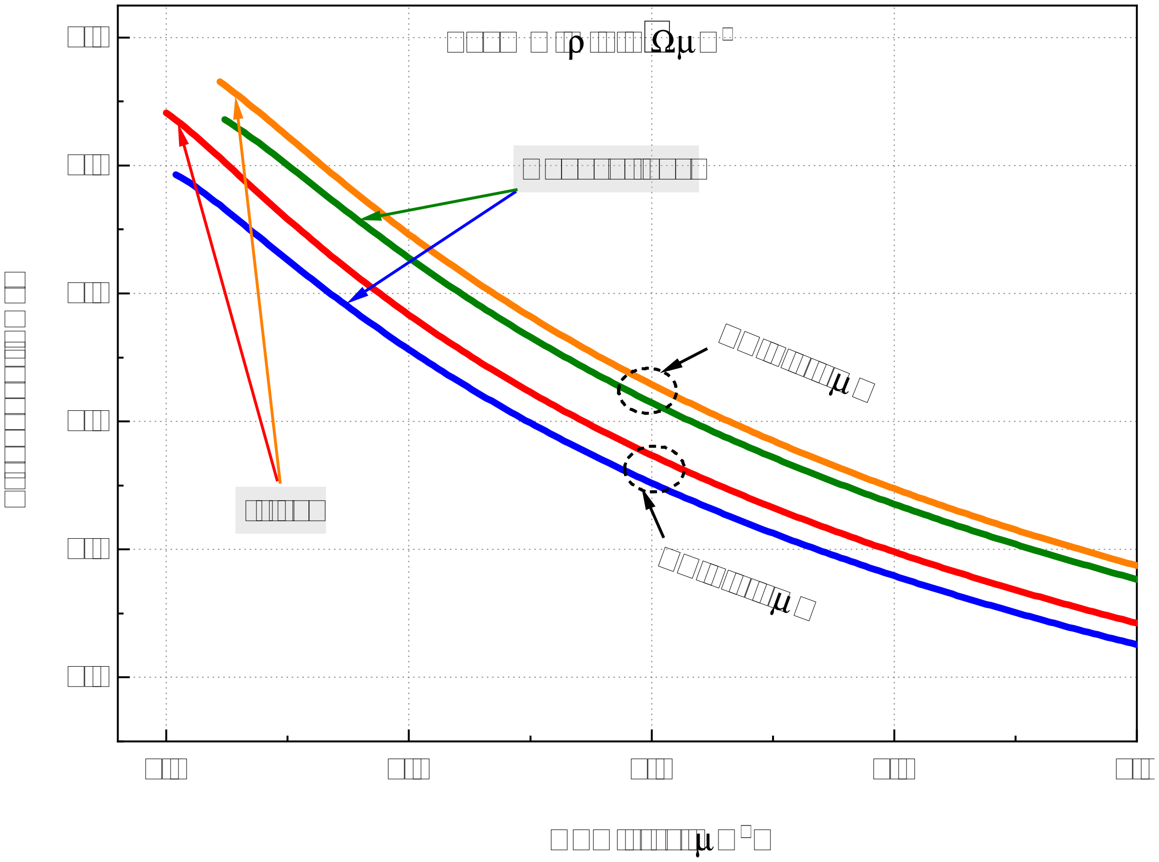

Figure 5.14: Simulated oscillation frequencies of conventional and island slot-antenna oscillators with LE thickness of 0.6 µm and 2.0 µm (with thick-electrode design as in Ref. [9]).

powers on the detector are shown in Fig. 5.15. To estimate the total emitted power of an oscillator, we needed to take into account that only 70% of the emitted power will pass to the air from inside the Si lens due to the back reflection. Further, the detector collects only a fraction of the power passing through the Si lens. This fraction is determined by the overlap of the radiation pattern of the slot antenna and the input aperture of the detector. We estimated (from the electromagnetic simulations of the radiation pattern of our slot antennas and the radiation pattern of a small dipole) this factor to be approximately 1/3 for our measurement setup. As a result, the detected power should be multiplied by a factor of ≈ 4 to estimate the total emitted power of our oscillators. We plotted these estimates in Fig. 5.15 for comparison with the literature data (typically, only such estimates for the emitted power are reported in the publications).

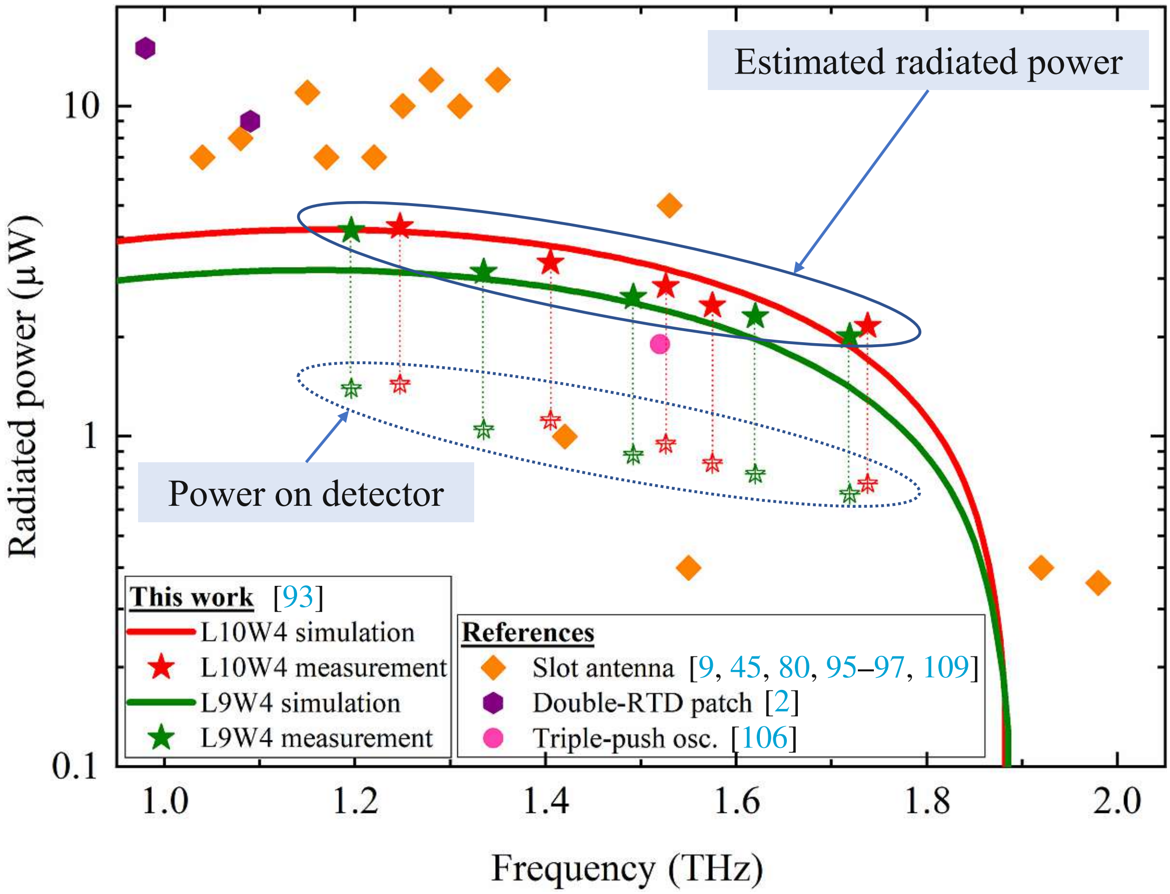

Figure 5.15: Radiated power vs. oscillation frequency of our island slot-antenna RTD oscillators with different slot antenna lengths and RTD areas. The empty stars show power measured on the detector, the filled stars show estimates for the total emitted power of the oscillators, and the solid lines show calculation results, which agree well with the experimental data. The literature data from the following publications Refs. [2, 9, 45, 80, 95–97, 106, 109] are also shown in the figure.

5.8 Conclusion

In conclusion, removing the n++ layer in the island design of the slot-antenna RTD oscillators leads to a drastic reduction of ohmic losses at the surface of the slot antenna at ≈ 2 THz. With this design, we demonstrated the oscillator radiated power of 2.2 µW at the fundamental frequency of 1.74 THz. Higher frequencies should be achievable with a reduction of the RTD contact resistance.

Chapter 6

Thesis Conclusions

This thesis focuses on the examination of RTD oscillators in the context of sub-THz and THz frequency range for both high output power and high oscillation frequency cases. In the first chapter, we have provided an introduction to the THz frequency range and the emerging applications that operate within this frequency region. We have summarized the electronic and optical devices that are progressively fulfilling the THz gap. The electronic sources cover the THz gap from the side of low frequencies; and the optical sources, on the other hand, cover the THz gap from the high-frequency side. The RTDs are good candidates for the sub-THz and THz electronic oscillators as they explore the negative differential conductance in the THz band.

In the second chapter, we have shown a detailed overview of RTD oscillators. We have described the operational principle of RTDs. We have shown the structural parameters of RTDs, such as the growth material systems, the barrier thickness, the spacer thickness, and the QW thickness which affect on the performance of the RTDs. Next, we have presented the early development of the RTD oscillators, and some different types of RTD oscillators. Among them, the symmetrical slot-antenna RTD oscillators have been chosen for the thesis. Next, we have mentioned the key design considerations for developing RTD oscillators in both cases of high oscillation frequencies and high output powers. Lastly, we have presented the simulation model of RTD oscillators for calculating the oscillation frequencies and the output powers.

In the third chapter, we have shown the structure design of the symmetrical slot-antenna RTD oscillator. We have described the fabrication processes of the RTD oscillator. Next, we have analyzed some factors that limit the maximum oscillation frequencies os the RTD oscillators, such as the contact parasitics, the spreading resistance, the antenna losses. In the high-frequency regime, the RTD areas of the RTD oscillators are quite small (in the range from 0.1 μm^2 to 0.5 μm^2), and the spreading resistance in this case has small impact; however, the top contact resistance plays a huge contribution on the total parasitic resistance. The spreading resistance is dominant for large RTD areas corresponding to the low-frequency regime of the RTD oscillators. For the simple analysis of maximizing the oscillation frequencies of RTD oscillators, by adjusting the effects of these parasitic elements, we can define the parameters of the antenna (such as the length and the width of the slot antenna) and the RTD mesa areas for a given RTD wafer.

In the fourth chapter, we have shown that the output power of symmetrical-slot-antenna RTD oscillators depends on the slot width and that the slot width is an important degree of freedom for fine tuning the slot geometry in the RTD oscillators. Our data also indicate that the commonly used 4 µm slot width is close to an optimal slot-parameter range, corresponding to the global output-power maximum, at least in the sub-THz frequency range. This is confirmed both by our theoretical and experimental data. We present an extensive set of experimental data on RTD oscillators with different slot widths. The data reasonably agree with the theoretical analysis and support its validity. Some oscillators exhibit the output-power level close to the state-of-the-art for fundamental-frequency symmetrical-slot-antenna RTD oscillators in the frequency range of 150-400 GHz. Specifically, we report 283 µW at 184 GHz and 82 µW at 368 GHz. The used RTDs have 1.6 nm barriers thickness. The peak current density is $\approx$ 6 mA/μm^2, and the peak to valley current ratio is $\approx$ 9), which allowed us for the fabrication of the oscillators to use solely optical lithography processes.

In the fifth chapter, we have presented an island slot-antenna RTD oscillator, where the contact n++ layer is removed everywhere except for a small island under the RTD. At frequencies around 2 THz, this design leads to a significant reduction (by a factor of $\approx$ 2) of the total ohmic losses at the conducting surfaces of the slot antenna. With this design, we have demonstrated the highest radiated power for RTD oscillators in the frequency range 1.6-1.74 THz with around 2.2 µW at the fundamental frequency of 1.74 THz. The RTD used in this work has 1.0 nm thick barrier, and its peak current density is 23.6 mA/ μm^2. We further demonstrate that the oscillation frequency above 2 THz should be reached if the RTD contact resistance is reduced to 1-1.5 $\Omega\mu m^2$.

Bibliography

[1] E. R. Brown, J. R. Söderström, C. D. Parker, L. J. Mahoney, K. M. Molvar, and T. C. McGill. Oscillations up to 712 GHz in InAs/AlSb resonant-tunneling diodes. *Applied Physics Letters*, 58(20):2291–2293, 1991. DOI: 10.1063/1.104902.

[2] P. Ourednik and M. Feiginov. Double-resonant-tunneling-diode bridge-less patch-antenna oscillators operating up to 1.09 THz. *Applied Physics Letters*, 120(18):183501, 2022. DOI: 10.1063/5.0090519.

[3] M. Asada and S. Suzuki. Room-temperature oscillation of resonant tunneling diodes close to 2 THz and their functions for various applications. *Journal of Infrared, Millimeter, and Terahertz Waves*, 37:1185–1198, 2016. DOI: 10.1007/s10762-016-0321-6.

[4] M. Feiginov. Frequency limitations of resonant-tunnelling diodes in sub-THz and THz oscillators and detectors. *Journal of Infrared, Millimeter, and Terahertz Waves*, 40:365–394, 2019. DOI: 10.1007/s10762-019-00573-5.

[5] M. Feiginov, C. Sydlo, O. Cojocari, and P. Meissner. Resonant-tunnelling-diode oscillators operating at frequencies above 1.1 THz. *Applied Physics Letters*, 99: 233506, 2011. DOI: 10.1063/1.3667191.

[6] Y. Koyama, Y. Kitazawa, K. Yukimasa, T. Uchida, T. Yoshioka, K. Fujimoto, T. Sato, J. Iba, K. Sakurai, and T. Ichikawa. A high-power terahertz source over 10 mW at 0.45 THz using an active antenna array with integrated patch antennas and resonant-tunneling diodes. *IEEE Transactions on Terahertz Science and Technology*, 12(5): 510–519, 2022. DOI: 10.1109/TTHZ.2022.3180492.

[7] K. Kasagi, S. Suzuki, and M. Asada. Large-scale array of resonant-tunneling-diode terahertz oscillators for high output power at 1 THz. *Journal of Applied Physics*, 125 (15), 2019. DOI: 10.1063/1.5051007.

[8] A. Al-Khalidi, K. H. Alharbi, J. Wang, R. Morariu, L. Wang, A. Khalid, J. M. L. Figueiredo, and E. Wasige. Resonant tunneling diode terahertz sources with up to 1 mW output power in the J-band. *IEEE Transactions on Terahertz Science and Technology*, 10(2):150–157, 2020. DOI: 10.1109/TTHZ.2019.2959210.

[9] R. Izumi, S. Suzuki, and M. Asada. 1.98 THz resonant-tunneling-diode oscillator with reduced conduction loss by thick antenna electrode. In *42nd International Conference on Infrared, Millimeter and Terahertz Waves (IRMMW-THz)*, pages 1–2, 2017. DOI: 10.1109/IRMMW-THz.2017.8066877.

[10] S. Suzuki, M. Shiraishi, H. Shibayama, and M. Asada. High-power operation of terahertz oscillators with resonant tunneling diodes using impedance-matched antennas and array configuration. *IEEE Journal of Selected Topics in Quantum Electronics*, 19: 8500108, 2013. DOI: 10.1109/JSTQE.2012.2215017.

[11] T. V. Mai, M. Asada, T. Namba, Y. Suzuki, and S. Suzuki. Coherent Power Combination in a Resonant-Tunneling-Diode Arrayed Oscillator with Simplified Structure. *IEEE Transactions on Terahertz Science and Technology*, pages 1–11, 2023. DOI: 10.1109/TTHZ.2023.3270672.

[12] M. Reddy, S. C. Martin, A. C. Molnar, R. E. Muller, R. P. Smith, P. H. Siegel, M. J. Mondry, M. J. W. Rodwell, H. Kroemer, and S. J. Allen. Monolithic Schottky-collector resonant tunnel diode oscillator arrays to 650 GHz. *IEEE Electron Device Letters*, 18 (5):218–221, 1997. DOI: 10.1109/55.568771.

[13] D. J. Headland, Y. Nishida, X. Yu, M. Fujita, and T. Nagatsuma. Terahertz Oscillator Chips Backside-Coupled to Unclad Microphotonics. *IEEE Journal of Selected Topics in Quantum Electronics*, 29(3: Photon. Elec. Co-Inte. and Adv. Trans. Print.):1–10, 2023. DOI: 10.1109/JSTQE.2022.3215524.

[14] G. Carpintero, E. Garcia-Munoz, H. Hartnagel, S. Preu, and A. Raisanen. *Semiconductor terahertz technology: devices and systems at room temperature operation*. John Wiley & Sons, 2015.

[15] D. Pavlidis. Introduction to THz technologies. *Fundamentals of Terahertz Devices and Applications*, pages 1–4, 2021. DOI: 10.1002/9781119460749.

[16] S. Fan, F. Qi, T. Notake, K. Nawata, T. Matsukawa, Y. Takida, and H. Minamide. Real-time terahertz wave imaging by nonlinear optical frequency up-conversion in a 4-dimethylamino-N-methyl-4-stilbazolium tosylate crystal. *Applied Physics Letters*, 104(10), 2014. DOI: 10.1063/1.4868134.

[17] T. S. Hartwick, D. T. Hodges, D. H. Barker, and F. B. Foote. Far infrared imagery. *Applied Optics*, 15(8):1919–1922, 1976. DOI: 10.1364/AO.15.001919.

[18] I. F. Akyildiz, J. M. Jornet, and C. Han. Terahertz band: Next frontier for wireless communications. *Physical Communication*, 12:16–32, 2014. DOI: 10.1016/j.phycom.2014.01.006.

[19] K. Ohata, K. Maruhashi, M. Ito, S. Kishimoto, K. Ikuina, T. Hashiguchi, K. Ikeda, and N. Takahashi. 1.25 Gbps wireless Gigabit Ethernet link at 60GHz-band. In *IEEE MTT-S International Microwave Symposium Digest, 2003*, volume 1, pages 373–376. IEEE, 2003. DOI: 10.1109/MWSYM.2003.1210955.

[20] J. Dong, A. Locquet, M. Melis, and D. S. Citrin. Global mapping of stratigraphy of an old-master painting using sparsity-based terahertz reflectometry. *Scientific Reports*, 7 (1):15098, 2017. DOI: 10.1038/s41598-017-15069-2.

[21] A. Dobroiu, M. Yamashita, Y. N. Ohshima, Y. Morita, C. Otani, and K. Kawase. Terahertz imaging system based on a backward-wave oscillator. *Applied Optics*, 43 (30):5637–5646, 2004. DOI: 10.1364/AO.43.005637.

[22] A. WM Lee, Qi Qin, S. Kumar, B. S. Williams, Q. Hu, and J. L. Reno. Real-time terahertz imaging over a standoff distance (> 25meters). *Applied Physics Letters*, 89 (14), 2006. DOI: 10.1063/1.2360210.

[23] H. Hoshina, Y. Sasaki, A. Hayashi, C. Otani, and K. Kawase. Noninvasive mail inspection system with terahertz radiation. *Applied Spectroscopy*, 63(1):81–86, 2009.

[24] F. Friederich, W. Von Spiegel, M. Bauer, F. Meng, M. D. Thomson, S. Boppel, A. Lisauskas, B. Hils, V. Krozer, A. Keil, et al. THz active imaging systems with real-time capabilities. *IEEE Transactions on Terahertz Science and Technology*, 1(1): 183–200, 2011. DOI: 10.1109/TTHZ.2011.2159559.

[25] G. J. Kim, J. I. Kim, S. G. Jeon, J. Kim, K. K. Park, and C. H. Oh. Enhanced continuous-wave terahertz imaging with a horn antenna for food inspection. *Journal of Infrared, Millimeter, and Terahertz Waves*, 33:657–664, 2012. DOI: 10.1007/s10762-012-9902-1.

[26] A. Lisauskas, M. Bauer, S. Boppel, M. Mundt, B. Khamaisi, E. Socher, R. Venckevičius, L. Minkevičius, I. Kašalynas, D. Seliuta, et al. Exploration of terahertz imaging with silicon MOSFETs. *Journal of Infrared, Millimeter, and Terahertz Waves*, 35: 63–80, 2014. DOI: 10.1007/s10762-013-0047-7.

[27] S. Augustin, S. Frohmann, P. Jung, and H. W. Hübers. Mask responses for single-pixel terahertz imaging. *Scientific Reports*, 8(1):4886, 2018. DOI: 10.1038/s41598-018-23313-6.

[28] Y. C. Shen, P. C. Upadhya, H. E. Beere, E. H. Linfield, A. G. Davies, I. S. Gregory, C. Baker, W. R. Tribe, and M. J. Evans. Generation and detection of ultrabroadband terahertz radiation using photoconductive emitters and receivers. *Applied Physics Letters*, 85(2):164–166, 2004. DOI: 10.1063/1.1768313.

[29] Yao-Chun Shen. Terahertz pulsed spectroscopy and imaging for pharmaceutical applications: A review. *International Journal of Pharmaceutics*, 417(1-2):48–60, 2011. DOI: 10.1016/j.ijpharm.2011.01.012.

[30] M. Polese, J. M. Jornet, T. Melodia, and M. Zorzi. Toward end-to-end, full-stack 6G terahertz networks. *IEEE Communications Magazine*, 58(11):48–54, 2020. DOI: 10.1109/MCOM.001.2000224.

[31] T. Kleine-Ostmann, K. Pierz, G. Hein, P. Dawson, and M. Koch. Audio signal transmission over THz communication channel using semiconductor modulator. *Electronics Letters*, 40(2):124–126, 2004. DOI: 10.1049/el:20040106.

[32] A. Hirata, R. Yamaguchi, H. Takahashi, T. Kosugi, K. Murata, N. Kukutsu, and Y. Kado. Effect of rain attenuation for a 10-Gb/s 120-GHz-band millimeter-wave wireless link. *IEEE transactions on Microwave Theory and Techniques*, 57(12): 3099–3105, 2009. DOI: 10.1109/TMTT.2009.2034342.

[33] T. Nagatsuma, M. Sonoda, T. Higashimoto, L. Yi, and J. Hesler. 12.5-Gbit/s wireless link at 720 GHz based on photonics. In *2019 44th International Conference on Infrared, Millimeter, and Terahertz Waves (IRMMW-THz)*, pages 1–2. IEEE, 2019. DOI: 10.1109/IRMMW-THz.2019.8873870.

[34] C. A. Burrus. Gallium Arsenide Esaki Diodes for High-Frequency Applications. *Journal of Applied Physics*, 32(6):1031–1036, 1961. DOI: 10.1063/1.1736154.

[35] D. T. Young, C. A. Burrus, and R. C. Shaw. High efficiency millimeter–wave tunnel–diode oscillators. *Proceedings of the IEEE*, 52(10):1260–1261, 1964. DOI: 10.1109/PROC.1964.3338.

[36] H. Eisele. Third-harmonic power extraction from InP Gunn devices up to 455 GHz. *IEEE Microwave and Wireless Components Letters*, 19(6):416–418, 2009. DOI: 10.1109/LMWC.2009.2020044.

[37] Z. S Gribnikov, R. R Bashirov, and V. V. Mitin. Negative effective mass mechanism of negative differential drift velocity and terahertz generation. *IEEE Journal of Selected Topics in Quantum Electronics*, 7(4):630–640, 2001. DOI: 10.1109/2944.974235.

[38] A. Acharyya and J. P. Banerjee. Prospects of IMPATT devices based on wide bandgap semiconductors as potential terahertz sources. *Applied Nanoscience*, 4:1–14, 2014. DOI: 10.1007/s13204-012-0172-y.

[39] G. I. Haddad, J. R. East, and C. Kidner. Tunnel transit-time (tunnett) devices for terahertz sources. *Microwave and Optical Technology Letters*, 4(1):23–29, 1991. DOI: 10.1002/mop.4650040109.

[40] J. Nishizawa, P. Płotka, T. Kurabayashi, and H. Makabe. 706-GHz GaAs CW fundamental-mode TUNNETT diodes fabricated with molecular layer epitaxy. *Physica Status Solidi C*, 5(9):2802–2804, 2008. DOI: 10.1002/pssc.200779256.

[41] D. M. Pozar. *Microwave engineering*. John wiley & sons, 2011.

[42] M. Urteaga, Z. Griffith, M. Seo, J. Hacker, and M. J. W. Rodwell. InP HBT technologies for THz integrated circuits. *Proceedings of the IEEE*, 105(6):1051–1067, 2017. DOI: 10.1109/JPROC.2017.2692178.

[43] U. R. Pfeiffer, Y. Zhao, J. Grzyb, R. Al Hadi, N. Sarmah, W. Förster, H. Rücker, and B. Heinemann. A 0.53 THz reconfigurable source module with up to 1 mW radiated power for diffuse illumination in terahertz imaging applications. *IEEE Journal of Solid-State Circuits*, 49(12):2938–2950, 2014. DOI: 10.1109/JSSC.2014.2358570.

[44] N. Buadana, S. Jameson, and E. Socher. A multiport chip-scale dielectric resonator antenna for CMOS THz transmitters. *IEEE Transactions on Microwave Theory and Techniques*, 68(9):3621–3632, 2020. DOI: 10.1109/TMTT.2020.2993845.

[45] S. Suzuki, M. Asada, A. Teranishi, H. Sugiyama, and H. Yokoyama. Fundamental oscillation of resonant tunneling diodes above 1 THz at room temperature. *Applied Physics Letters*, 97(24):242102, 2010. DOI: 10.1063/1.3525834.

[46] B. S. Williams. Terahertz quantum-cascade lasers. *Nature Photonics*, 1(9):517–525, 2007. DOI: 10.1038/nphoton.2007.166.

[47] R. Koehler, A. Tredicucci, F. Beltram, H. E. Beere, E. H. Linfield, A. G. Davies, D. A. Ritchie, R. C. Iotti, and F. Rossi. THz Quantum Cascade Laser. In *APS March Meeting Abstracts*, pages M8–004, 2002.

[48] Y. Jin, JL Reno, and S. Kumar. Phase-locked terahertz plasmonic laser array with 2 W output power in a single spectral mode. *Optica*, 7(6):708–715, 2020. DOI: 10.1364/OPTICA.390852.

[49] L. H. Li, L. Chen, J. R. Freeman, M. Salih, P. Dean, A. G. Davies, and E. H. Linfield. Multi-Watt high-power THz frequency quantum cascade lasers. *Electronics Letters*, 53(12):799–800, 2017. DOI: 10.1049/el.2017.0662.

[50] K. Fujita, S. Hayashi, A. Ito, T. Dougakiuchi, M. Hitaka, and A. Nakanishi. Broadly tunable lens-coupled nonlinear quantum cascade lasers in the sub-THz to THz frequency range. *Photonics Research*, 10(3):703–710, 2022. DOI: 10.1364/PRJ.443819.

[51] Q. Lu, N. Bandyopadhyay, S. Slivken, Y. Bai, and M. Razeghi. Continuous operation of a monolithic semiconductor terahertz source at room temperature. *Applied Physics Letters*, 104(22), 2014. DOI: 10.1063/1.4881182.

[52] E. Bründermann, D. R. Chamberlin, and E. E. Haller. 7igh duty cycle and continuous terahertz emission from germanium. *Applied Physics Letters*, 76(21):2991–2993, 2000. DOI: 10.1063/1.126555.

[53] A. Bergner, U. Heugen, E. Bründermann, G. Schwaab, M. Havenith, D. R. Chamberlin, and E. E. Haller. New p-Ge THz laser spectrometer for the study of solutions: THz absorption spectroscopy of water. *Review of Scientific Instruments*, 76(6), 2005. DOI: 10.1063/1.1928427.

[54] H. W. Hübers, S. G. Pavlov, and V. N. Shastin. Terahertz lasers based on germanium and silicon. *Semiconductor Science and Technology*, 20(7):S211, 2005. DOI: 10.1088/0268-1242/20/7/011.

[55] S. Preu, G. H. Döhler, S. Malzer, L. J. Wang, and A. C. Gossard. Tunable, continuous-wave terahertz photomixer sources and applications. *Journal of Applied Physics*, 109 (6), 2011. DOI: 10.1063/1.3552291.

[56] K. Sengupta, T. Nagatsuma, and D. M. Mittleman. Terahertz integrated electronic and hybrid electronic–photonic systems. *Nature Electronics*, 1(12):622–635, 2018. DOI: 10.1038/s41928-018-0173-2.

[57] C. Spudat, P. Ourednik, G. Picco, D. Tuan Nguyen, and M. Feiginov. Limitations of output power and efficiency of simple resonant-tunneling-diode oscillators. *IEEE Transactions on Terahertz Science and Technology*, 13(1):82–92, 2022. DOI: 10.1109/TTHZ.2022.3228069.

[58] N. Oshima, K. Hashimoto, S. Suzuki, and M. Asada. Terahertz wireless data transmission with frequency and polarization division multiplexing using resonant-tunneling-diode oscillators. *IEEE Transactions on Terahertz Science and Technology*, 7:593–598, 2017. DOI: 10.1109/TTHZ.2017.2720470.

[59] J. Webber, T. Yamamoto, N. Nishigami, Y. Nishida, M. Fujita, and T. Nagatsuma. Multi-level wireless transmission using resonant tunneling diodes in 300-GHz band. *Electronics Letters*, 59(5):e12731, 2023. DOI: 10.1049/ell2.12731.

[60] T. Miyamoto, A. Yamaguchi, and T. Mukai. Terahertz imaging system with resonant tunneling diodes. *Japanese Journal of Applied Physics*, 55:032201, 2016. DOI: 10.7567/JJAP.55.032201.

[61] K. Okamoto, K. Tsuruda, S. Diebold, S. Hisatake, M. Fujita, and T. Nagatsuma. Terahertz sensor using photonic crystal cavity and resonant tunneling diodes. *Journal of Infrared, Millimeter, and Terahertz Waves*, 38:1085–1097, 2017. DOI: 10.1007/s10762-017-0391-0.

[62] A. Dobroiu, R. Wakasugi, Y. Shirakawa, S. Suzuki, and M. Asada. Absolute and precise terahertz-wave radar based on an amplitude-modulated resonant-tunneling-diode oscillator. *Photonics*, 5(4), 2018. DOI: 10.3390/photonics5040052.

[63] P. Ourednik and M. Feiginov. Chip-Size Double-Resonant-Tunneling-Diode Patch-Antenna Oscillators and their sub-THz Application. In *15th UK-Europe-China Work. Millim.-Waves and Terahertz Technol. (UCMMT)*, pages 1–3, 2022. DOI: 10.1109/UCMMT56896.2022.9994843.

[64] D. Bohm. Quantum Theory Prentice-Hall. *Englewood Cliffs, NJ*, 1951.

[65] L. V. Iogansen. Resonance tunneling of electrons in crystals. *Soviet Physics JETP*, 1965.

[66] R. Tsu and L. Esaki. Tunneling in a finite superlattice. *Applied Physics Letters*, 22 (11):562–564, 1973. DOI: 10.1063/1.1654509.

[67] LL Chang, L. Esaki, and R. Tsu. Resonant tunneling in semiconductor double barriers. *Applied Physics Letters*, 24(12):593–595, 1974. DOI: 10.1063/1.1655067.

[68] T. J. Shewchuk, P. C. Chapin, P. D. Coleman, W. Kopp, R. Fischer, and H. Morkoç. Resonant tunneling oscillations in a GaAs-Al x Ga1- x As heterostructure at room temperature. *Applied Physics Letters*, 46(5):508–510, 1985. DOI: 10.1063/1.95574.

[69] D. J. Griffiths and D. F. Schroeter. *Introduction to quantum mechanics*. Cambridge university press, 2018.

[70] S. Luryi. Frequency limit of double-barrier resonant-tunneling oscillators. *Applied Physics Letters*, 47(5):490–492, 1985. DOI: 10.1063/1.96102.

[71] C. I. Huang, M. J. Paulus, C. A. Bozada, S. C. Dudley, K. R. Evans, C. E. Stutz, R. L. Jones, and M. E. Cheney. AlGaAs/GaAs double barrier diodes with high peak-to-valley current ratio. *Applied Physics Letters*, 51(2):121–123, 1987. DOI: 10.1063/1.98588.

[72] H. Mizuta and T. Tanoue. High-speed and functional applications of resonant tunnelling diodes. *The Physics and Applications of Resonant Tunnelling Diodes*, page 133, 2006.

[73] M. Tsuchiya, H. Sakaki, and J. Yoshino. Room temperature observation of differential negative resistance in an AlAs/GaAs/AlAs resonant tunneling diode. *Japanese Journal of Applied Physics*, 24(6A):L466, 1985. DOI: 10.1143/JJAP.24.L466.

[74] A. Forster, J. Lange, D. Gerthsen, C. Dieker, and H. Luth. The effect of growth temperature on AlAs/GaAs resonant tunnelling diodes. *Journal of Physics D: Applied Physics*, 27(1):175, 1994. DOI: 10.1088/0022-3727/27/1/028.

[75] E. Wolak, E. Özbay, B. G. Park, S. K. Diamond, D. M. Bloom, and James S. Harris J. The design of GaAs/AlAs resonant tunneling diodes with peak current densities over 2× 105 A cm- 2. *Journal of Applied Physics*, 69(5):3345–3350, 1991. DOI: 10.1063/1.348563.

[76] T. Inata, S. Muto, Y. Nakata, T. Fujii, H. Ohnishi, and S. Hiyamizu. Excellent negative differential resistance of InAlAs/InGaAs resonant tunneling barrier structures grown by MBE. *Japanese Journal of Applied Physics*, 25(12A):L983, 1986. DOI: 10.1143/JJAP.25.L983.

[77] I. Mehdi and G. Haddad. Lattice matched and pseudomorphic In0. 53Ga0. 47As/In x Al1- x As resonant tunneling diodes with high current peak-to-valley ratio for millimeter-wave power generation. *Journal of Applied Physics*, 67(5):2643–2646, 1990. DOI: 10.1063/1.345472.

[78] T. Inata, S. Muto, Y. Nakata, S. Sasa, T. Fujii, and S. Hiyamizu. A pseudomorphic In0. 53Ga0. 47As/AlAs resonant tunneling barrier with a peak-to-valley current ratio of 14 at room temperature. *Japanese Journal of Applied Physics*, 26(8A):L1332, 1987. DOI: 10.1143/JJAP.26.L1332.

[79] J. H. Smet, T. P. E. Broekaert, and C. G. Fonstad. Peak-to-valley current ratios as high as 50: 1 at room temperature in pseudomorphic In0. 53Ga0. 47As/AlAs/InAs resonant tunneling diodes. *Journal of Applied Physics*, 71(5):2475–2477, 1992. DOI: 10.1063/1.351085.

[80] H. Kanaya, H. Shibayama, R. Sogabe, S. Suzuki, and M. Asada. Fundamental oscillation up to 1.31 THz in resonant tunneling diodes with thin well and barriers. *Applied Physics Express*, 5(12):124101, 2012. DOI: 10.1143/APEX.5.124101.

[81] L. F. Luo, R. Beresford, and W. I. Wang. Resonant tunneling in AlSb/InAs/AlSb double-barrier heterostructures. *Applied Physics Letters*, 53(23):2320–2322, 1988. DOI: 10.1063/1.100266.

[82] J. Singh. *Physics of Semiconductors and their Heterostructures*. McGraw-Hill College, 1993.

[83] H. Kroemer. The 6.1 A family (InAs, GaSb, AlSb) and its heterostructures: a selective review. *Physica E: Low-dimensional Systems and Nanostructures*, 20(3-4):196–203, 2004. DOI: 10.1016/j.physe.2003.08.003.

[84] J. R. Soderstrom, D. H. Chow, and T. C. McGill. InAs/AlSb double-barrier structure with large peak-to-valley current ratio: a candidate for high-frequency microwave devices. *IEEE Electron Device Letters*, 11(1):27–29, 1990. DOI: 10.1109/55.46920.

[85] L. Britnell, R. V. Gorbachev, A. K. Geim, L. A. Ponomarenko, A. Mishchenko, M. T. Greenaway, T. M. Fromhold, K. S. Novoselov, and L. Eaves. Resonant tunnelling and negative differential conductance in graphene transistors. *Nature Communications*, 4 (1):1794, 2013. DOI: 10.1038/ncomms2817.

[86] J. Gaskell, L. Eaves, K. S. Novoselov, A. Mishchenko, A. K. Geim, T. M. Fromhold, and M. T. Greenaway. Graphene-hexagonal boron nitride resonant tunneling diodes as high-frequency oscillators. *Applied Physics Letters*, 107(10):103105, 2015. DOI: 10.1063/1.4930230.

[87] N. Kacem, A. Bhouri, JL Lazzari, and N. Jaba. Quantum well width and barrier Thickness effects on the perpendicular transport in polar and non-polar oriented AlGaN/GaN Resonant Tunneling Diodes. In *2021 IEEE International Conference on Design & Test of Integrated Micro & Nano-Systems (DTS)*, pages 1–6. IEEE, 2021. DOI: 10.1109/DTS52014.2021.9498223.

[88] H. Mizuta and T. Tanoue. *The physics and applications of resonant tunnelling diodes*. Cambridge Studies in Semiconductor Physics and Microelectronic Engineering, 1995.

[89] T. C. L. G. Sollner, P. E. Tannenwald, D. D. Peck, and W. D. Goodhue. Quantum well oscillators. *Applied Physics Letters*, 45(12):1319–1321, 1984. DOI: 10.1063/1.95134.

[90] E. R. Brown, W. D. Goodhue, and T. C. L. G. Sollner. Fundamental oscillations up to 200 GHz in resonant tunneling diodes and new estimates of their maximum oscillation frequency from stationary-state tunneling theory. *Journal of Applied Physics*, 64(3): 1519–1529, 1988. DOI: 10.1063/1.341827.

[91] E. R. Brown, T. C. L. G. Sollner, C. D. Parker, W. D. Goodhue, and C. L. Chen. Oscillations up to 420 GHz in GaAs/AlAs resonant tunneling diodes. *Applied Physics Letters*, 55(17):1777–1779, 1989. DOI: 10.1063/1.102190.

[92] M. E. Hines. High-Frequency Negative-Resistance Circuit Principles for Esaki Diode Applications. *Bell System Technical Journal*, 39(3):477–513, 1960. DOI: 10.1002/j.1538-7305.1960.tb03933.x.

[93] D. Tuan Nguyen, P. Ourednik, and M. Feiginov. Island THz on-chip slot-antenna resonant-tunneling-diode oscillators. *Applied Physics Letters*, 123(4), 2023. DOI: 10.1063/5.0159147.

[94] K. Kasagi, S. Suzuki, and M. Asada. Array configuration using resonant-tunneling-diode terahertz oscillator integrated with patch antenna. In *2015 40th International Conference on Infrared, Millimeter, and Terahertz waves (IRMMW-THz)*, pages 1–2. IEEE, 2015.

[95] T. Maekawa, H. Kanaya, S. Suzuki, and M. Asada. Frequency increase in terahertz oscillation of resonant tunnelling diode up to 1.55 THz by reduced slot-antenna length. *Electronics Letters*, 50(17):1214–1216, 2014. DOI: 10.1049/el.2014.2362.

[96] T. Maekawa, H. Kanaya, S. Suzuki, and M. Asada. Oscillation up to 1.92 THz in resonant tunneling diode by reduced conduction loss. *Applied Physics Express*, 9(2): 024101, 2016. DOI: 10.7567/APEX.9.024101.

[97] H. Kanaya, T. Maekawa, S. Suzuki, and M. Asada. Structure dependence of oscillation characteristics of resonant-tunneling-diode terahertz oscillators associated with intrinsic and extrinsic delay times. *Japanese Journal of Applied Physics*, 54(9):094103, 2015. DOI: 10.7567/JJAP.54.094103.

[98] P. Ourednik, T. Hackl, C. Spudat, D. Tuan Nguyen, and M. Feiginov. Double-resonant-tunneling-diode patch-antenna oscillators. *Applied Physics Letters*, 119(26):263509, 2021. DOI: 10.1063/5.0068114.

[99] T. V. Mai, Y. Suzuki, X. Yu, S. Suzuki, and M. Asada. Structure-simplified resonant-tunneling-diode terahertz oscillator without metal-insulator-metal capacitors. *Journal of Infrared, Millimeter, and Terahertz Waves*, 41:1498–1507, 2020. DOI: 10.1007/s10762-020-00738-7.

[100] K. Urayama, S. Aoki, S. Suzuki, M. Asada, H. Sugiyama, and H. Yokoyama. Sub-terahertz resonant tunneling diode oscillators integrated with tapered slot antennas for horizontal radiation. *Applied Physics Express*, 2(4):044501, 2009. DOI: 10.1143/APEX.2.044501.

[101] M. Asada, K. Osada, and W. Saitoh. Theoretical analysis and fabrication of small area metal/insulator resonant tunneling diode integrated with patch antenna for terahertz photon assisted tunneling. *Solid-State Electronics*, 42(7-8):1543–1546, 1998. DOI: 10.1016/S0038-1101(98)00067-7.

[102] R. Sekiguchi, Y. Koyama, and T. Ouchi. Subterahertz oscillations from triple-barrier resonant tunneling diodes with integrated patch antennas. *Applied Physics Letters*, 96 (6):062115, 2010. DOI: 10.1063/1.3315868.

[103] M. Feiginov. Sub-terahertz and terahertz microstrip resonant-tunneling-diode oscillators. *Applied Physics Letters*, 107(12), 2015. DOI: 10.1063/1.4931727.

[104] E. R. Brown, T. C. L. G. Sollner, W. D. Goodhue, and C. D. Parker. Millimeter-band oscillations based on resonant tunneling in a double-barrier diode at room temperature. *Applied Physics Letters*, 50(2):83–85, 1987. DOI: 10.1063/1.97826.

[105] N. Orihashi, S. Suzuki, and M. Asada. One THz harmonic oscillation of resonant tunneling diodes. *Applied Physics Letters*, 87(23):233501, 2005. DOI: 10.1063/1.2139850.

[106] J. Lee, M. Kim, and K. Yang. A 1.52 THz RTD Triple-Push Oscillator With a uW Level Output Power. *IEEE Transactions on Terahertz Science and Technology*, 6: 336–340, 2016. DOI: 10.1109/TTHZ.2015.2509358.

[107] S. Iwamatsu, Y. Nishida, M. Fujita, and T. Nagatsuma. Terahertz coherent oscillator integrated with slot-ring antenna using two resonant tunneling diodes. *Applied Physics Express*, 14(3):034001, 2021. DOI: 10.35848/1882-0786/abdb8f.

[108] J. Lee, M. Kim, and J. Lee. 692 GHz high-efficiency compact-size InP-based fundamental RTD oscillator. *IEEE Transactions on Terahertz Science and Technology*, 11 (6):716–719, 2021. DOI: 10.1109/TTHZ.2021.3108431.

[109] X. Yu, Y. Suzuki, M. V. Ta, S. Suzuki, and M. Asada. Highly efficient resonant tunneling diode terahertz oscillator with a split ring resonator. *IEEE Electron Device Letters*, 42(7):982–985, 2021. DOI: 10.1109/LED.2021.3082577.

[110] M. Feiginov. Does the quasibound-state lifetime restrict the high-frequency operation of resonant-tunnelling diodes? *Nanotechnology*, 11:359, 2000. DOI: 10.1088/0957-4484/11/4/333.

[111] M. Feiginov. Effect of the coulomb interaction on the response time and impedance of the resonant-tunneling diodes. *Applied Physics Letters*, 76:2904, 2000. DOI: 10.1063/1.126512.

[112] M. Feiginov. Displacement currents and the real part of high-frequency conductance of the resonant-tunneling diode. *Applied Physics Letters*, 78:3301, 2001. DOI: 10.1063/1.1372357.

[113] P. Ourednik, G. Picco, D. Tuan Nguyen, C. Spudat, and M. Feiginov. Large-signal dynamics of resonant-tunneling diodes. *Journal of Applied Physics*, 133(1):014501, 2023. DOI: 10.1063/5.0134223.

[114] N. Orihashi, S. Hattori, S. Suzuki, and M. Asada. Experimental and theoretical characteristics of sub-terahertz and terahertz oscillations of resonant tunneling diodes integrated with slot antennas. *Japanese Journal of Applied Physics*, 44(11R):7809, 2005. DOI: 10.1143/JJAP.44.7809.

[115] M. Asada, S. Suzuki, and N. Kishimoto. Resonant tunneling diodes for sub-terahertz and terahertz oscillators. *Japanese Journal of Applied Physics*, 47(6R):4375, 2008. DOI: 10.1143/JJAP.47.4375.

[116] G.K. Reeves. Specific contact resistance using a circular transmission line model. *Solid-State Electronics*, 23(5):487–490, 1980. DOI: 10.1016/0038-1101(80)90086-6.

[117] G. K. Reeves and H. B. Harrison. Obtaining the specific contact resistance from transmission line model measurements. *IEEE Electron Device Letters*, 3(5):111–113, 1982. DOI: 10.1109/EDL.1982.25502.

[118] D. K. Schroder. *Semiconductor material and device characterization*. John Wiley & Sons, 2015.

[119] N. Kishimoto, S. Suzuki, A. Teranishi, and M. Asada. Frequency Increase of Resonant Tunneling Diode Oscillators in Sub-THz and THz Range Using Thick Spacer Layers. *Applied Physics Express*, 1(4):042003, 2008. DOI: 10.1143/APEX.1.042003.

[120] H. Kanaya, R. Sogabe, T. Maekawa, S. Suzuki, and M. Asada. Fundamental oscillation up to 1.42 THz in resonant tunneling diodes by optimized collector spacer thickness. *Journal of Infrared, Millimeter, and Terahertz Waves*, 35:425–431, 2014. DOI: 10.1007/s10762-014-0058-z.

[121] M. Feiginov, H. Kanaya, S. Suzuki, and M. Asada. Operation of resonant-tunneling diodes with strong back injection from the collector at frequencies up to 1.46 THz. *Applied Physics Letters*, 104:243509, 2014. DOI: 10.1063/1.4884602.

[122] S. Suzuki, N. Kishimoto, M. Asada, N. Sekine, and I. Hosako. Experimental and theoretical investigation of the dependence of oscillation characteristics on structure of integrated slot antennas in sub-terahertz and terahertz oscillating resonant tunneling diodes. *Japanese Journal of Applied Physics*, 47(1R):64, 2008. DOI: 10.1143/JJAP.47.64.

[123] H. Shibayama, M. Shiraishi, S. Suzuki, and M. Asada. High-power operation of terahertz oscillators with resonant tunneling diodes using offset-fed slot antennas and array configuration. *Journal of Infrared, Millimeter, and Terahertz Waves*, 33:475–478, 2012. DOI: 10.1109/JSTQE.2012.2215017.

[124] M. Feiginov, C. Sydlo, O. Cojocari, and P. Meissner. Operation of resonant-tunnelling oscillators beyond tunnel lifetime limit. *Europhysics Letters*, 94(4):48007, 2011. DOI: 10.1209/0295-5075/94/48007.

[125] M. Feiginov, C. Sydlo, O. Cojocari, and P. Meissner. High-frequency nonlinear characteristics of resonant-tunnelling diodes. *Applied Physics Letters*, 99(13):133501, 2011. DOI: 10.1063/1.3644491.

[126] M. Feiginov, C. Sydlo, O. Cojocari, and P. Meissner. Operation of resonant-tunnelling-diode oscillators beyond tunnel-lifetime limit at 564 GHz. *Europhysics Letters*, 97(5): 58006, 2012. DOI: 10.1209/0295-5075/97/58006.

[127] F. Han, H. Fujikata, H. Tanaka, S. Suzuki, and M. Asada. Terahertz Oscillator using Rectangular-Cavity Resonator and Large-Area RTD with Heat Dissipation Structure. In *47th International Conference on Infrared, Millimeter and Terahertz Waves (IRMMW-THz)*, pages 1–2. IEEE, 2022.

[128] M. Kim, Jooseok Lee, Jongwon Lee, and K. Yang. A 675 GHz Differential Oscillator Based on a Resonant Tunneling Diode. *IEEE Transactions on Terahertz Science and Technology*, 6(3):510–512, 2016. DOI: 10.1109/TTHZ.2016.2554399.

[129] M. Bezhko, S. Suzuki, and M. Asada. Analysis of output power characteristics for resonant-tunneling diode terahertz oscillator with cylindrical cavity resonator. *Japanese Journal of Applied Physics*, 60(12):121002, dec 2021. DOI: 10.35848/1347-4065/ac3721.

[130] Z. Jéhn. Cylindrical Cavity Optimization for Resonant-Tunneling Diode Oscillators. *IEEE Transactions on Microwave Theory and Techniques*, 70(5):2658–2667, 2022. DOI: 10.1109/TMTT.2022.3150146.

List of publications

Journal articles:

[J1] **D. Tuan Nguyen**, G. Picco, P. Ourednik, and M. Feiginov, "Impact of slot width on performance of symmetrical-slot-antenna resonant-tunneling-diode oscillators," *IEEE Transactions on Terahertz Science and Technology.* Submitted, under review.

[J2] **D. Tuan Nguyen**, P. Ourednik, and M. Feiginov, "Island thz on-chip slot-antenna resonant-tunneling-diode oscillators," *Applied Physics Letters*, vol. 123, no. 4, 2023. DOI: 10.1063/5.0159147.

[J3] P. Ourednik, T. Hackl, C. Spudat, **D. Tuan Nguyen**, and M. Feiginov, "Double-resonanttunneling-diode patch-antenna oscillators," *Applied Physics Letters*, vol. 119, no. 26, 263509, 2021. DOI: 10.1063/5.0068114.

[J4] P. Ourednik, G. Picco, **D. Tuan Nguyen**, C. Spudat, and M. Feiginov, "Large-signal dynamics of resonant-tunneling diodes," *Applied Physics Letters*, vol. 133, no. 1, p. 014 501, 2023. DOI: 10.1063/5.0134223.

[J5] C. Spudat, P. Ourednik, G. Picco, **D. Tuan Nguyen**, and M. Feiginov, "Limitations of output power and efficiency of simple resonant-tunneling-diode oscillators," *IEEE Transactions on Terahertz Science and Technology*, vol. 13, no. 1, pp. 82–92, 2023. DOI: 10.1109/TTHZ.2022.3228069.

Conference articles:

[C1] **D. Tuan Nguyen**, P. Ourednik, and M. Feiginov, "Conventional vs. island THz slot-antenna resonant-tunneling-diode oscillators," in *2023 48th International Conference on Infrared, Millimeter and Terahertz Waves (IRMMW-THz)*, 2023.

[C2] P. Ourednik, **D. Tuan Nguyen**, and M. Feiginov, "A simple view on large-signal resonant-tunneling-diode dynamics," in *2023 48th International Conference on Infrared, Millimeter and Terahertz Waves (IRMMW-THz)*, 2023.

[C3] P. Ourednik, T. Hackl, C. Spudat, **D. Tuan Nguyen**, and M. Feiginov, "Double-resonant-tunneling-diode chip-size patch-antenna oscillator," in *International School on Terahertz photonics and electronics, Pisa*, 2022.

[C4] M. Feiginov, P. Ourednik, and **D. Tuan Nguyen**, “Improved performance of THz resonant-tunneling-diode oscillators,” in *10th International Symposium on Terahertz-Related Devices and Technologies, Aizu-Wakamatsu*, 2023.

Curriculum Vitae

NGUYEN DINH TUAN

Date of birth: 16.09.1985
Nationality: Vietnam

OBJECTIVE

Candidate for the title: Doctor of Engineering Sciences, Dr. Ing., at the Department of Electrical Engineering and Information Technology, TU Wien

EDUCATION

Bachelor of Applied Mathematics and Physics 2006 - 2010
Moscow Institute of Physics and Technology, Department of Radio Engineering and Cybernetics
Programme: Radio Engineering and Cybernetics

Master of Applied Mathematics and Physics 2010 - 2012
Moscow Institute of Physics and Technology, Department of Radio Engineering and Cybernetics
Programme: Electronic Computers and Computer Engineering
Thesis: Increasing the speed of data transmission CAN package

Doctoral Study, in THz Electronics 2018 - present
TU Wien, Department of Electrical Engineering and Information Technology
Research Topic: THz and Sub-THz RTD Oscillators
Thesis: Optimization of Sub-THz and THz Resonant-Tunneling-Diode Oscillators with Symmetrical Slot Antennas

EXPERIENCE

Teaching Assistant 2013 - 2016
Department of Microelectronics and Microprocessing, Faculty of Radio-Electronics, Le Quy Don Technical University, Hanoi, Vietnam

Lecturer 2016 - present
Department of Microelectronics and Microprocessing, Faculty of Radio-Electronics, Le Quy Don Technical University, Hanoi, Vietnam